



HAL
open science

Adaptation of the paleoseismological approach to local tectonic regime: comparative study of the intraplate Basel-Reinach fault, Switzerland and the interplate North Anatolian fault, Turkey.

Matthieu Ferry

► To cite this version:

Matthieu Ferry. Adaptation of the paleoseismological approach to local tectonic regime: comparative study of the intraplate Basel-Reinach fault, Switzerland and the interplate North Anatolian fault, Turkey.. Geophysics [physics.geo-ph]. Universität Zürich, 2004. English. NNT: . tel-00007036

HAL Id: tel-00007036

<https://theses.hal.science/tel-00007036>

Submitted on 20 Oct 2004

HAL is a multi-disciplinary open access archive for the deposit and dissemination of scientific research documents, whether they are published or not. The documents may come from teaching and research institutions in France or abroad, or from public or private research centers.

L'archive ouverte pluridisciplinaire **HAL**, est destinée au dépôt et à la diffusion de documents scientifiques de niveau recherche, publiés ou non, émanant des établissements d'enseignement et de recherche français ou étrangers, des laboratoires publics ou privés.

Adaptation of the paleoseismological approach to local
tectonic regime: comparative study of the intraplate Basel-
Reinach fault, Switzerland and the interplate North
Anatolian fault, Turkey.

A dissertation submitted to the
SWISS FEDERAL INSTITUTE OF TECHNOLOGY ZURICH

For the Degree of
Doctor of Sciences

Presented by
FERRY, MATTHIEU ALEXIS
DEA IPGS – EOST – STRASBOURG
Born March 23rd, 1973
Citizen of France

Accepted on the recommendation of

Prof. Dr. D. Giardini, examiner
Prof. Dr. M. Meghraoui, co-examiner
Prof. Dr. A. Pfiffner, co-examiner
Prof. Dr. R. Armijo, co-examiner

Table of content

Abstract	5
Résumé	7
Introduction	11
<u>Chapter 1.</u>	13
Linking Past and Present, Depth and Surface: an introduction to the Paleoseismological approach	
1.1. Unveiling past earthquake parameters: the paleoseismological approach	
1.1.1. Seismic risk assessment	
1.1.2. The physics of earthquakes	
1.1.2.1. Rupture process	
1.1.2.2. Earthquake recurrence	
1.1.2.3. Characteristic earthquakes	
1.1.3. What paleoseismology brings	
1.2. A multidisciplinary approach: standard tools	
1.2.1. Regions at risk: historical and instrumental seismicity	
1.2.2. Fault identification and long-term history: geomorphology	
1.2.2.1. Satellite imagery	
1.2.2.2. Regional digital elevation model	
1.2.2.3. Aerial photography	
1.2.3. Geometry at depth and long-term vertical displacement: reflection seismics	
1.2.4. Shallow geometry and recent displacement: sub-surface geophysics	
1.2.4.1. High-resolution seismics	
1.2.4.2. Electrical tomography	
1.2.4.3. Ground-penetrating radar	
1.2.5. Recent cumulative displacement: micro-topography	
1.2.6. Recent history of sedimentation vs. faulting: trenching	
1.2.6.1. Making the most of a trench site: site selection	
1.2.6.2. Optimizing excavations: trench layout	
1.2.6.3. Acquisition of trench data: logging and sampling	
1.2.6.3.1. Logging	
1.2.6.3.2. Photo-mosaicing	
1.2.6.3.3. Dating	
1.2.6.3.3.1. Radiocarbon	
1.2.6.3.3.2. Thermoluminescence	
1.2.6.3.3.3. Cosmogenic nuclides	
1.2.6.3.3.4. Palynochronology	
1.2.6.4. Identification of a paleoseismic event: criteria	
1.2.6.5. Improving data quality: cross-correlating events	
1.2.6.6. Optimizing dates: the Bayesian statistical analysis	
<u>Chapter 2.</u>	49
Active Normal Faulting in the Rhine Graben and Paleoseismic Identification of the 1356, I₀=IX-X, Basel Earthquake (Central Europe)	
Summary	
Introduction	
2.1. The Basel earthquake	
2.2. Geological Setting and Seismotectonic Background	
2.3. Paleoseismic results and surface ruptures of the 1356	

earthquake

2.4. Discussion and conclusions

2.4.1. A major seismic source in the Basel area

2.4.2. Seismic history of the Basel area

2.4.3. Active tectonics in intraplate Europe and related seismic hazard implications

Chapter 3. Evidence for Holocene Paleoseismicity along the Basel-Reinach Active Normal Fault (Switzerland): A Seismic Source for the 1356 Earthquake in the Upper Rhine Graben **63**

Summary

3.1. Introduction

3.2. The 1356 Basel Earthquake

3.3. Neotectonic and Seismotectonic Framework

3.4. Fault Scarp Geomorphology

3.5. Geophysical Investigations

3.5.1. Methods

3.5.2. Results

3.6. Sample Datations and Age Determination

3.7. Paleoseismic Trench Analysis

3.7.1. Site 1

3.7.2. Site 2

3.7.2.1. Trenches 1 and 4

3.7.2.2. Trench 3

3.7.2.3. Trench 5

3.7.3. Evidence of Recent Faulting From the 1962 Trench

3.8. Summary

3.8.1. Paleoseismic Events Inferred From Trenching

3.8.2. Events Identified Within Other Geological Archives

3.9. Discussion

3.9.1. Faulting Geometry and Length Extension

3.9.2. Seismotectonic Characteristics and Deformation Rate

3.9.3. Implications for the Seismic Hazard

Chapter 4. Ground-penetrating radar investigations along the North Anatolian fault near Izmit (Turkey): Constraints on the right-lateral movement and slip history **99**

Abstract

4.1. Introduction

4.2. GPR Method And Site Selection

4.3. Profile Analyses

4.3.1. Köseköy Site

4.3.2. The A.D. 1591 Ottoman Canal Site

4.4. Discussion And Conclusions

Chapter 5. Paleoearthquake History of the western portion of the North Anatolian Fault in Western Turkey from paleoseismic data, and implications to the seismic hazard of Istanbul **111**

Abstract

5.1 Introduction

- 5.2. The Saros Site
 - 5.2.1. Site Stratigraphy
 - 5.2.2. Evidence for Earthquakes
 - 5.2.3. Determination of Lateral Slip
- 5.3. Izmit to Sapanca Segment
 - 5.3.1. The Ottoman Canal Site
 - 5.3.2. The Köseköy Site
 - 5.3.2.1. Site Stratigraphy
 - 5.3.2.2. Interpretation of Past Earthquakes
 - 5.3.3. Discussion of Results
 - 5.3.3.1. Hazard to Istanbul

<u>Conclusions and Outlook</u>	141
<u>References</u>	143
<u>World Wide Web Resources</u>	155
<u>Acknowledgements</u>	159
<u>Lebenslauf</u>	161

Abstract

The assessment of seismic risk in a given region relies on the proper estimate of related seismic hazard, i.e. the probability that an earthquake of said magnitude occurs within a said time window. Calculating that probability requires a precise knowledge of local seismotectonic parameters such as the frequency of damaging earthquakes, their magnitude and the annual deformation rate. These parameters may only be properly determined when observed over a representative time window. As return periods for strong earthquakes vary between a few decades and several millennia, instrumental and historical seismological datasets often prove to be insufficient. To improve the completeness of available seismicity catalogues, we applied the paleoseismological approach to two different regions: the Basel region (southern Upper Rhine Graben) which was struck by a destructive earthquake in 1356 and the Izmit region (east of the Marmara Sea), partly destroyed in August 1999 by a magnitude 7.4 tremor.

A full integrated study involving geomorphology, geophysics and trenching in the Basel region led to the identification of the seismogenic fault responsible for the last strong earthquake and to deciphering its seismic history for the Holocene. Thus, we demonstrate that the newly identified Basel-Reinach fault is the locus for a magnitude 6.4-6.7 earthquake every ~2600 years, on average. Furthermore, we give strong evidence for the probable extension of the fault through the city of Basel to the north and the folded Jura to the south. These results have a direct impact on the level of seismic risk to the region as it was consequently lowered by one degree on the basis of our original work.

We applied a similar, though adapted, approach to the North Anatolian fault around the Marmara Sea. An extensive trenching effort combined with ground-penetrating radar profiles carried out on the Ganos fault to the west and the Izmit-Sapanca segment to the east evidence several recent events and yield measurements of pertaining co-seismic offsets. They clearly show characteristic behavior on both sides of the Marmara Sea, however with varying offsets: 4 to 5 m for the Ganos fault and 2 to 2.5 m for the Izmit-Sapanca segment. This brings new constrains to better characterize faulting behavior in the region and consequent seismic risk to the city of Istanbul.

Résumé

La prise en compte du risque sismique dans une région donnée passe par l'évaluation de l'aléas, c'est-à-dire la probabilité qu'un séisme de magnitude définie se produise dans un intervalle de temps défini. Le calcul de cette probabilité repose sur certains paramètres sismo-tectoniques locaux tels que la fréquence des tremblements de terre destructeurs, leur magnitude ainsi que le taux de déformation annuel. Ces paramètres ne seront convenablement déterminés qu'en disposant d'une fenêtre d'observation représentative des phénomènes en jeu. Face à des périodes de retour variant de quelques décennies à plusieurs millénaires, les données sismologiques instrumentales et historiques se révèlent souvent insuffisantes. Afin de compléter les catalogues de sismicité disponibles, nous avons appliqués les méthodes de la paléosismologie à deux régions très différentes : la région de Bâle (sud du Fossé Rhénan) frappée par un séisme destructeur en 1356 et la région d'Izmit (est de la Mer de Marmara) en grande partie détruite en Août 1999 par un séisme de magnitude 7.4.

Une étude intégrée complète de la région de Bâle a permis d'identifier la faille responsable du dernier grand séisme puis de retracer son histoire sismique holocène. Nous avons ainsi démontré qu'elle est le lieu d'un évènement de magnitude 6.4-6.7 tous les 2600 ans, en moyenne. De plus, nous donnons des indications fortes sur son prolongement au travers de la ville de Bâle, au nord, et du Jura Plissé, au sud. Ces résultats ont une incidence directe sur le niveau de risque sismique régnant dans la région. En effet, celui-ci a diminué d'un degré depuis la prise en compte de ces éléments jusqu'ici inédits.

Nous avons appliqué une approche similaire, quoique adaptée, à la faille Nord Anatolienne autour de la Mer de Marmara. Une campagne de tranchées menée sur la faille de Ganos à l'ouest et sur le segment Izmit-Sapanca à l'est ainsi que des profils de radar géologique ont mis en évidence plusieurs évènements récents et permis de déterminer l'amplitude des mouvements co-sismiques produits lors de ces séismes. Ceux-ci montrent clairement un comportement caractéristique des deux côtés de la Mer de Marmara, avec toutefois des déplacements co-sismiques différents : 4 à 5 m pour Ganos et 2 à 2.5 m pour Izmit-Sapanca.

The beginning of knowledge is the discovery of something we do not understand.
Frank Herbert

Introduction

The present thesis was carried out in the frame of several research projects, the main one being the PALEOSEIS project. PALEOSEIS was initiated as part of the wider PEGASOS project which aims at updating risk assessment for nuclear facilities in Switzerland. As instrumental and historical seismicity data for strong and damaging events are incomplete with respect to the earthquake cycle, the paleoseismological approach was considered a valuable alternative to assess the frequency and intensity of M6+ earthquakes in Switzerland.

Adapting that approach to available geological archives, a large part of the project was devoted to the study of soft-sediment deformation in lake deposits (Becker et al., 2002; Monecke, 2004) and earthquake-triggered subaquatic slumps (Schnellmann, 2004). That same approach was applied to the Basel region (Becker et al., 2002) which endured a M6.5 earthquake in 1356. As a matter of fact, the Basel region displays geomorphological features most likely unmodified by glaciers during the last ice age. Consequently, we additionally applied the now classical paleoseismological approach to the Basel region as it is used to study major active faults throughout the world. We adapted the approach and especially made great use of exploration geophysics in a region where i) slip rate is only ~ 0.2 mm/yr and deformation is not prominent, ii) erosion is strong and minor landforms are poorly preserved and iii) land is heavily urbanized with few places available for trench studies. One should say that many feasibility criteria turned out to be somehow borderline cases and we could not achieve strong a priori confidence regarding the study's outcome. This led us to gather a large amount of data and cross-check results with several different methods to rule out inconsistencies and build up an ensemble of converging pieces of evidence. Eventually, we ended up with what is likely one of the most in-depth integrated active fault studies to date, especially with respect to the length of the Basel-Reinach fault. Most usually, paleoseismic studies focus on recent surface rupture to retrieve parameters for the last 2 to 4 earthquakes or on deformed old geomorphic features to estimate long-term slip-rate. Here, we start the study from the very beginning on the basis of historical damage produced by the 1356 earthquake (Mayer-Rosa and Cadot, 1979) and search the region for adequate geomorphic features. We identify a scarp which geophysics show to be linked to a deeply rooted fault system. Detailed geophysical and geomorphological investigations help identify recent fault strands affecting shallow sediments. Several sites are selected and investigated by means of excavations following a standard approach commonly applied to major active faults such as the San Andreas fault system or the North Anatolian fault but only seldom to faults with low slip rates (Meghraoui et al., 2000).

In parallel, we participate to several efforts following the destructive 1999 Izmit and Düzce earthquakes along the North Anatolian fault Turkey. There, we study obviously recent surface rupture by means of classical excavations and rather vanguard ground-penetrating radar (GPR) surveys. We test its usability and potential for paleoseismic purposes with the intent to develop its use in the near future. Actually, GPR shows to be flexible and efficient at imaging concealed shallow fault strands where morphology is not preserved or expressed. Furthermore, we can detect offset buried channels that document slip history for the last 3 events and perform virtual trenching, thus complementing and partially replacing expensive and time-consuming excavations. As the study is exploratory, we favor trenching to obtain basic strong data and only perform GPR surveys where and when possible. Encouraging results lead us to consider giving growing importance to lightweight high-resolution geophysics for our future active fault studies along fast faults in the eastern Mediterranean. Besides, we would recommend following a standard procedure including microtopographic survey, geophysical survey (with processing and interpretation steps) then trenching on the basis of cross-checked data.

In conclusion, we demonstrate that geophysical methods are still underused for paleoseismic purposes and may provide valuable extra information. The right method should be selected on the basis of several fault parameters such as slip rate, slip mechanism and slip per event. Furthermore, our study shows that very recent surface rupture may easily be concealed and only detected by means of geophysical exploration.

Chapter 1

Linking Past and Present, Depth and Surface: an Introduction to the Paleoseismological Approach

How does an earthquake shape the environment? Linking rupture processes which occur at depths of several tens of kilometers to changes in the landscape is no easy task. It has long been an obstacle for paleoseismological studies, mostly because intermediate phenomena were not fully understood, and explained. In the present chapter, we present an overview of physical processes associated to an earthquake or to a fault's activity and which shall be taken into account for seismic hazard and seismic risk calculations. Then, we discuss how the paleoseismological approach may bring unique data as well as new insights to contribute to better understanding of seismic behavior and mitigation seismic risk. This will be thoroughly illustrated by two paleoseismic studies undergone in i) an intraplate region of low seismicity with a single known historical earthquake (see Chapters 2 and 3 about the 1356 Basel, Switzerland, earthquake) and ii) an interplate region of high seismicity with short recurrence intervals and a long detailed historical record (see Chapters 4 and 5 about the North Anatolian fault, Turkey). On the basis of both these studies, we will demonstrate how Paleoseismology may be originally and successfully applied using techniques adapted to specific geological conditions and we will suggest recommendations for future work.

1.1. Unveiling past earthquake parameters: the paleoseismological approach

Nowadays, public authorities and private companies in developed countries (and to a lesser extent in developing countries) show a growing concern for seismic risk and pertaining mitigation. Indeed, as cities expand and value-added wealth is produced, damage and induced reconstruction costs increase exponentially. In parallel, many crucial facilities are as well potential sources of strong health issues if damaged by an earthquake (nuclear power plants, oil refineries and transportation networks, storages for toxic chemical compounds, etc) and are attracting more and more public concern. Furthermore, as our knowledge of tectonic processes improves, regions previously thought to be quiet may turn to be at risk. Consequently, new branches of Seismology are developing to bring answers to these questions. Among these approaches, Paleoseismology aims at linking past earthquakes to present-day observations to better characterize location, occurrence frequencies and magnitudes of damaging events in a region, hence documenting seismic hazard to improve risk mitigation. Taking into account necessary criteria used to compute seismic hazard, Paleoseismology is the approach dealing with the determination of past earthquake parameters on the basis of information recorded and preserved by geological processes.

1.1.1. Seismic risk assessment

For a given region of the world, ranging from a country to a city –or even a single building–, seismic risk is the combination of seismic vulnerability and seismic hazard. Vulnerability reflects structural properties of a given building or class of buildings, thus indicating their susceptibility to endure more or less severe damage or even total collapse during an earthquake of given magnitude.

Vulnerability may be emphasized by local history, site effects, construction habits or construction codes. The Basel region has a multimillennium-long history as a central passage point on the Rhine river. Many buildings of the old city center, built on sediments from the Rhine, are several centuries-old and their design does not take into account seismic risk issues. At the other end of Europe, private houses in Turkey are often built by their owner over several years, extra stories being added as money becomes available. However, foundations are never upgraded, thus increasing the overall fragility of the building.

Seismic hazard focuses on earthquakes themselves as natural phenomena. There, the aim is to determine several standard parameters (mainly frequency and magnitude) used to characterize damaging events in a given region. The combination of vulnerability and hazard produces a value (or set of values) called seismic risk which describes the potential “cost” induced by the settlement of a given anthropic activity in a given region (here with respect to earthquakes). The same general approach may be applied to various sources of hazard, either natural (e.g., floods, hurricanes, rock falls) or artificial (e.g., leakage from a chemical or nuclear facility).

1.1.2. The physics of earthquakes

1.1.2.1. Rupture process

In 1910, Reid proposed a model to describe strike-slip deformation associated to an earthquake based on interseismic and coseismic phases. At a sufficient depth, the geological medium is ductile enough to be continuously and aseismically deformed. More to the surface, deformation is brittle, discreet and concentrated along faults. As far-field elastic deformation goes on continuously, it induces a sigmoidal bend perpendicular to the fault, which is locked by roughness and asperities. When stress concentration (or pore pressure) on the fault exceeds its strength, it breaks and near-field coseismic deformation catches up catastrophically with far-field interseismic deformation. With each earthquake, that deformation cycle starts again. It should be noted that the amount and velocity of deformation are supposed to be constant from event to event, thus suggesting that the cycle is perfectly periodic and magnitude and time of occurrence are predictable.

1.1.2.2. Earthquake recurrence

Reid's model has been derived since then by Shimaki and Nakata (1980) into two possibilities where either time or slip is predictable (Fig. 1.1). In a time-predictable model, the stress threshold at which failure occurs is known and constant. Given the slip of the previous earthquake and the rate of strain accumulation, the time of the next earthquake may be calculated, not its slip (or magnitude). Conversely, in a slip-predictable model, the stress threshold at which failure stops is known and constant. Given the time of the previous earthquake and the rate of strain accumulation, the slip of the next earthquake may be calculated, not its time.

1.1.2.3. Characteristic earthquake

Schwartz and Coppersmith (1984) proposed that some faults or fault segments break repeatedly with similar slip amounts and slip distributions at comparable return intervals (Fig. 1.1). Such a fault would be typified by characteristic earthquakes. As a result, detailed data related to a single event would bring significant understanding of faulting behavior and future events, thus achieving a tremendous step towards earthquake prediction and risk mitigation.

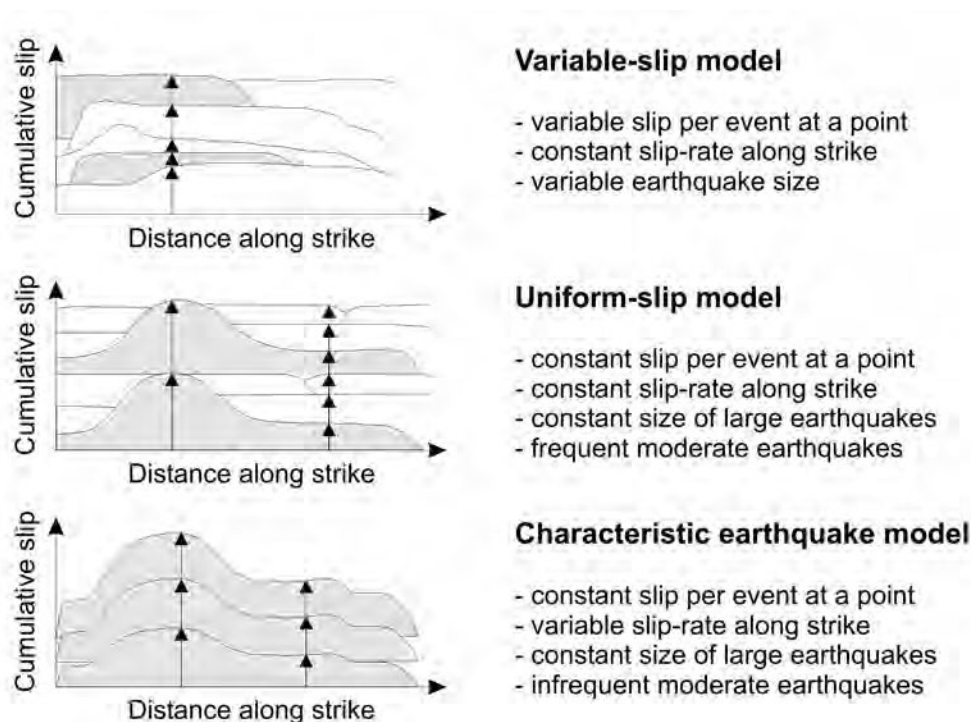


Figure 1.1. Models for variable slip (top), uniform slip (center) and characteristic earthquakes (bottom). Modified after Schwartz and Coppersmith (1984).

To test these different models and eventually improve our knowledge of active tectonic processes, it appears necessary to have a detailed dataset at one's disposal,

including values of slip amounts, recurrence intervals, rupture lengths, etc... Obviously, the best model would integrate the largest dataset available for a given fault or fault system such as what is being carried out for the San Andreas fault in California, USA (extensive literature from Sieh, 1978 to Dawson et al., 2003).

1.1.3. What paleoseismology brings

Paleoseismology addresses a specific timescale that bridges neotectonics and instrumental seismology, namely from late Pleistocene to present day. A detailed paleoseismic study may help describe slip distribution along a fault or fault segment for individual earthquakes with $M=6$ and over dating back to several thousand years. Characterizing past earthquakes parameters (fault location, magnitude, and recurrence interval) shall help build a strong enough dataset to test models and determine seismic hazard.

1.2. A multidisciplinary approach: standard tools

According to a famous comment by George Bernard Shaw, “scientists are people who know a great deal about very little”. That very approach appears not to be applicable to paleoseismology as it relies on diverse domains of Earth Sciences and beyond to achieve a single goal. It is striking to realize that many paleoseismologists are actually structural geologists, geomorphologists, sedimentologists, limnogeologists, rock mechanics, exploration geophysicists or seismologists with a specific concern for active tectonics and seismic hazard. Indeed, paleoseismology relies on different subject matters to assess parameters of past earthquakes:

- Humanities (including Archeology and History) to locate the maximum damage area produced by an historical earthquake as described in historical documents (Mayer-Rosa and Cadiot, 1979) or recorded by man-made structures at archeological sites (Klinger et al., 2000),
- Geomorphology to evaluate long-term deformation and tectonic activity,
- Shallow geophysics to locate buried surface rupture and settle trench sites,
- Sedimentology, soil science and soft-sediments mechanics to understand the geological record,
- Tectonics to trace faulting events backwards from trench observations,
- Geochemistry to understand and interpret age determinations,
- Seismology to link surface observations to earthquakes and to compute seismic hazard calculations.

Though it is not necessary to master each of those matters, some fairly high level of knowledge must be acquired to enable a proper communication and guarantee a standard quality for interpretations and results. Indeed, paleoseismologists are in need for these external pieces of information and cannot suppose that their colleagues show proper paleoseismological sensitivity. Here, we will go through some of these methods –preferably those used in the frame of the present thesis as well as some of the most widespread- to explain their principles and how they are used within the frame of paleoseismic investigations. As they are numerous and rather different, we will not enter the detail of each of them. Several fundamental books do explore them into detail, which the reader should consult profitably. McCalpin (1996) edited a comprehensive textbook which covers all geological aspects of paleoseismology from fundamental physics to field techniques. Stratton Noller et al. (2000) wrote an extremely detailed monograph on the various techniques of Quaternary Geochronology. Burbank and Anderson (2001) focused on relationships between tectonics and geomorphology for which they provide numerous recent case studies. However, it shall be noted that none of these authors develops the use and importance of sub-surface geophysics. Actually, they are seldom used in regions of high seismic activity although they may be very helpful (see Chap. 4) and paleoseismic studies are still only few in regions of low seismicity where they may provide valuable information and complement scarce datasets (see Chap. 2 and 3).

1.2.1. Regions at risk: historical and instrumental seismicity

Basic data needed for seismic hazard calculations must reflect the frequency and the strength of potential earthquakes in a region. Typically, frequency is given by the return period, i.e. the mean time interval between two similar events (it should be noted that for seismic risk calculation purposes earthquakes may not necessarily be produced by the same source, i.e. fault). To be properly assessed, the return period must be shorter than the observation time window for two successive earthquakes to be recorded. Historical data may be used as an alternative when the length of the instrumental record is not adequate. Indeed, descriptions of destruction endured by buildings over an area help map damage intensity for a given event (see Fig. 2.2 in Chap. 2 and Fig. 5.? in Chap. 5). As damage is strongly related to the intensity of seismic shaking, the maximum damage area (mesoseismal zone) usually coincides with the location of the seismic source. Though the shape of the mesoseismal zone does not necessarily reflect the geometry of the fault, it most generally comprises a large portion of it. Such an intensity map is a precious document to initiate field investigations.

In Switzerland, for instance, routine instrumental recording dates back to 1975, this limits applicability to extremely short recurrence intervals. However, historical and

archeological datasets are rich and point to the largest known historical earthquake north of the Alps as having struck the city of Basel on 18th October 1356. There is no unambiguous historical evidence that another similar event (in terms of magnitude and induced damage) occurred since then or before. With a single data point, the only possible value for the return period is 650 years (i.e. today - 1356). However, this is a minimum value that leads to an unknown overestimate of seismic hazard for the region as the true recurrence interval is most likely longer. Paleoseismological investigations in the Basel region (see Chap. 2 and 3) revealed that a total of five earthquakes occurred on that same fault during the Holocene, with a mean return period of 2600 years. That single result significantly changes the level of seismic hazard to the Basel region as it is now a level 3a seismic zone instead of 3b with respect to Swiss building codes SIA 260 (2003 edition, supersedes 1989 edition SIA 160).

Similarly, the Middle East has an extensive and detailed historical record of past earthquakes for the last two millennia (Poirier and Taher, 1980) with return periods of a few centuries. Hence, major faults have been thoroughly characterized such as the North Anatolian fault (Ambraseys and Finkel, 1995) and the Dead Sea fault (Khair et al., 2000; Meghraoui et al., 2003). Khair et al. (2000) proposed a segmentation model for the Dead Sea fault on the basis of historical seismicity only, with pertaining consequences on potential rupture lengths, stress accumulation and triggering of nearby faults.

1.2.2. Fault identification and long-term deformation: geomorphology

Once an area of high probability has been determined for the location of a fault (on the basis of historical and/or instrumental data), one may have a closer look at the landscape to identify features typical of an active structure. For a fault to produce large earthquakes with surface rupture, some level of maturity must be reached. Indeed, as magnitude is directly correlated to the dimensions of the rupture area, only a fault of pre-existing sufficient area may be the locus of a damaging earthquake. Typically, following Wells and Coppersmith (1994), with a typical seismogenic thickness of 15 km, an $M_w=6.5$ shock (i.e., the 1356 Basel earthquake) requires a rupture length of 15 km with 0.7 m coseismic slip. Similarly, it requires 120 km of rupture and 2.5 m of slip to build up an $M_w=7.4$ event (i.e., the 1999 Izmit earthquake). Thus, producing surface rupture supposes that a long-term process took place before to build up favorable and sufficient rupture area, involving noticeable cumulative surface deformation with –most frequently– visible geomorphological features such as fault scarps, perturbed drainage patterns (see section 1.2.5.), young deposits in an anomalous position, uplifted terraces (Berryman et al., 1989), etc... Such a long-term deformation signature may help characterize long-term slip rate (used in hazard calculations, see Chap. 3), provided that features may be dated and their amount of deformation may be measured.

Furthermore, they usually point to their associated active fault, which may be crucial in a region of low seismicity where no strong instrumental earthquake has ever been recorded.

Remote sensing techniques (as detailed in the following section) provide simultaneously large-scale and high-resolution images which help locate interesting features in a region of several km² (aerial photographs) to several hundreds of km² (satellite images). They offer enough zooming capacity to start a detailed study of a potential fault scarp prior to undertaking potentially expensive and time-consuming field surveys.

1.2.2.1. Satellite imagery

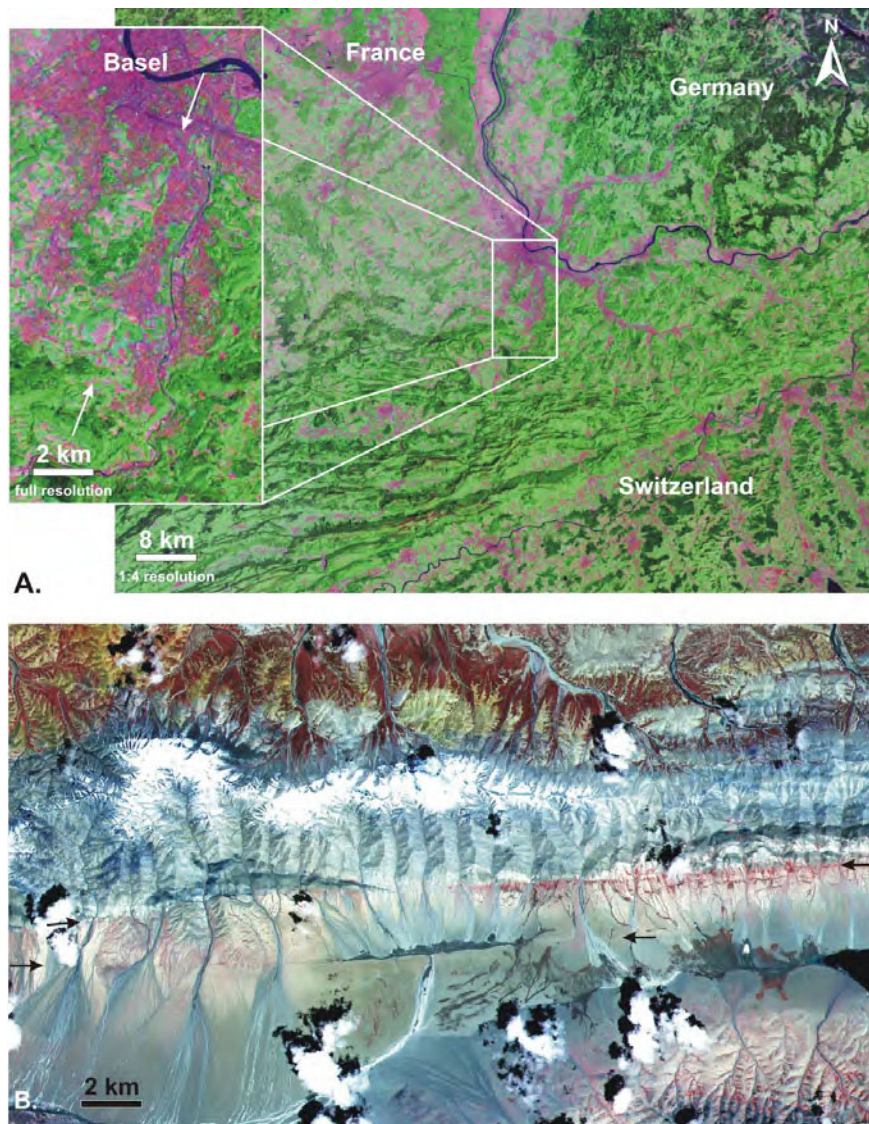


Figure 1.2. A) Landsat image (MrSID format, distributed by NASA) for the Basel, Switzerland region. False colors indicate vegetation (shades of green), wet areas (pink to purple) and free water (dark blue). A sharp contrast between a vegetation-covered area and a floodplain (see inset) suggests the possible occurrence of a fault (between white arrows). B) ASTER false color image of the Kunlun fault, Tibet, following the 2001 Kokoxili earthquake. Arrows indicate pertaining surface rupture (see text for details), which is underlined by dark stream deposits blocked by the fault scarp.

Since the recent rapid development of space technologies, observation of the Earth has been a major priority for satellite design. Most of our planet may be scrutinized using a wide spectrum of electromagnetic (EM) frequencies including infrared and radar and be mapped for various purposes as a function of the on-board sensor type (see Gupta, 2003 for an in-depth review of remote sensing geology). It is generally assumed that the Earth's surface reflects ~10% of solar radiations. Our planet itself emits some radiation due to its thermal state. The combined EM radiation spectrum may be collected by passive sensors which equip the different specialized satellites. However, before hitting a sensor, EM waves travel through the atmosphere and undergo absorption (by H₂O vapor, CO₂ and O₃ mainly) and scattering (nonselective by clouds and fog, selective by molecules smaller than the wavelength).

For instance, the ASTER (Advanced Spaceborne Thermal Emission and Reflection) sensor, which was launched aboard the Terra satellite (EOS-AM-1) by NASA in 1999, incorporates three subsystems dedicated to recording three different parts of the infrared spectrum. It offers 30 m-resolution-images with enhanced vertical exaggeration for stereoscopic and photogrammetric applications. Furthermore, as shown by Rowan and Mars (2003, see Fig. 1.3), mineral groups and rocks reflect unique absorption bands which vary with frequency and serve as identification criteria to map lithological units and, possibly, faults. Other natural and artificial objects may be identified with remote sensing and contribute to a better location of faults, such as variations in water content and subsequent vegetation distribution (tree or shrubby lines may grow along lines of water circulation on the fault).

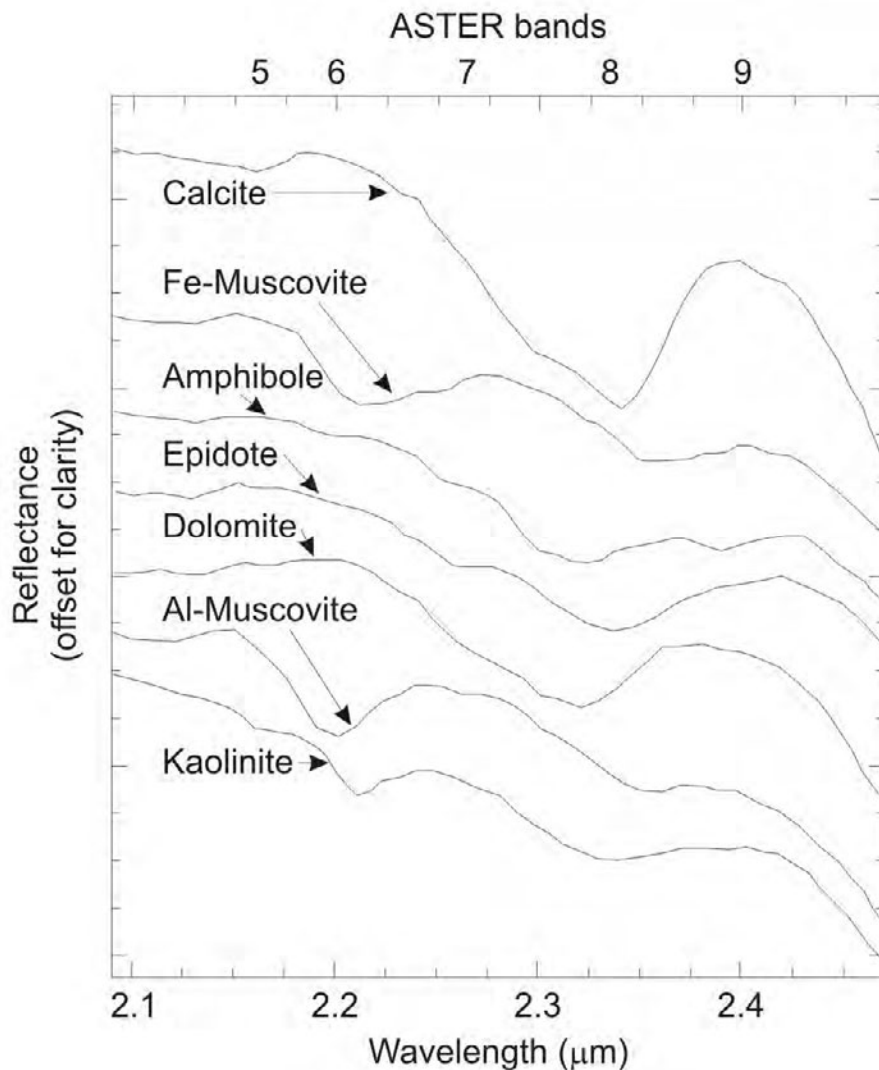


Figure 1.3. Response spectrum of various minerals as recorded by the ASTER sensor. Absorption bands differ for each mineral species (i.e. 2.29-2.33 for calcite and 2.19-2.2 for Al-muscovite). From Rowan and Mars, 2003.

Similarly, Klinger et al. (2003) recently took advantage of meter-resolution Ikonos images to map sections of the 250-km-long surface rupture produced by the 14th November 2001, Mw=7.9 Kokoxili earthquake along the Kunlun fault, Tibet. Exceptional zooming capacities unveiled meter-scale features (mostly ridges and river streams) affected by displacements which could be accurately measured on the sole basis of remote sensing data. Taking into consideration the very poor accessibility of the region and pertaining high fieldwork costs, those satellite images provide fast, crucial and unique information.

1.2.2.2. Regional digital elevation models

A digital elevation model is a numerical representation of a landscape surface given in (X, Y, Z) format where X is northings, Y is eastings (both in degrees, kilometers or meters) and Z is the elevation (traditionally in meters above sea level). These datasets may be obtained by

direct measurement in the field (high-resolution microtopography with a total station –see section 1.2.5.-, differential GPS or LIDAR), digitization of existing topographic maps, photogrammetry (use of stereoscopic pair of aerial/satellite images to extract elevation information) or Synthetic Aperture Radar (SAR) interferometry (radar stereoscopy between two satellite passes).

Global datasets such as GTOPO30, DTED0 and GLOBE (see Section World Wide Web resources) have ~1 km resolution which is sufficient for continental or national studies but not adequate for regional ones. National mapping agencies usually provide 25-m-resolution datasets well adapted to geomorphological studies. However, these datasets are often digitized maps for which the density of original (i.e. verified) data points is not known and often low. It may thus be reasonable to turn to updated satellite data such as these provided by ASTER and SRTM (Shuttle Radar Topographic Mission) missions. They consist in 30-m-spaced data points with strong internal consistency, though ASTER elevations are relative for a single shot/file (they are internally calibrated with respect to one-off atmospheric conditions) and may vary significantly between two consecutive satellite passes (users should prefer sequenced files recorded the same day with similar –preferentially dry and cloudless- atmospheric conditions or may experience significant offsets of elevations, typically of the order of 30m to 50m).

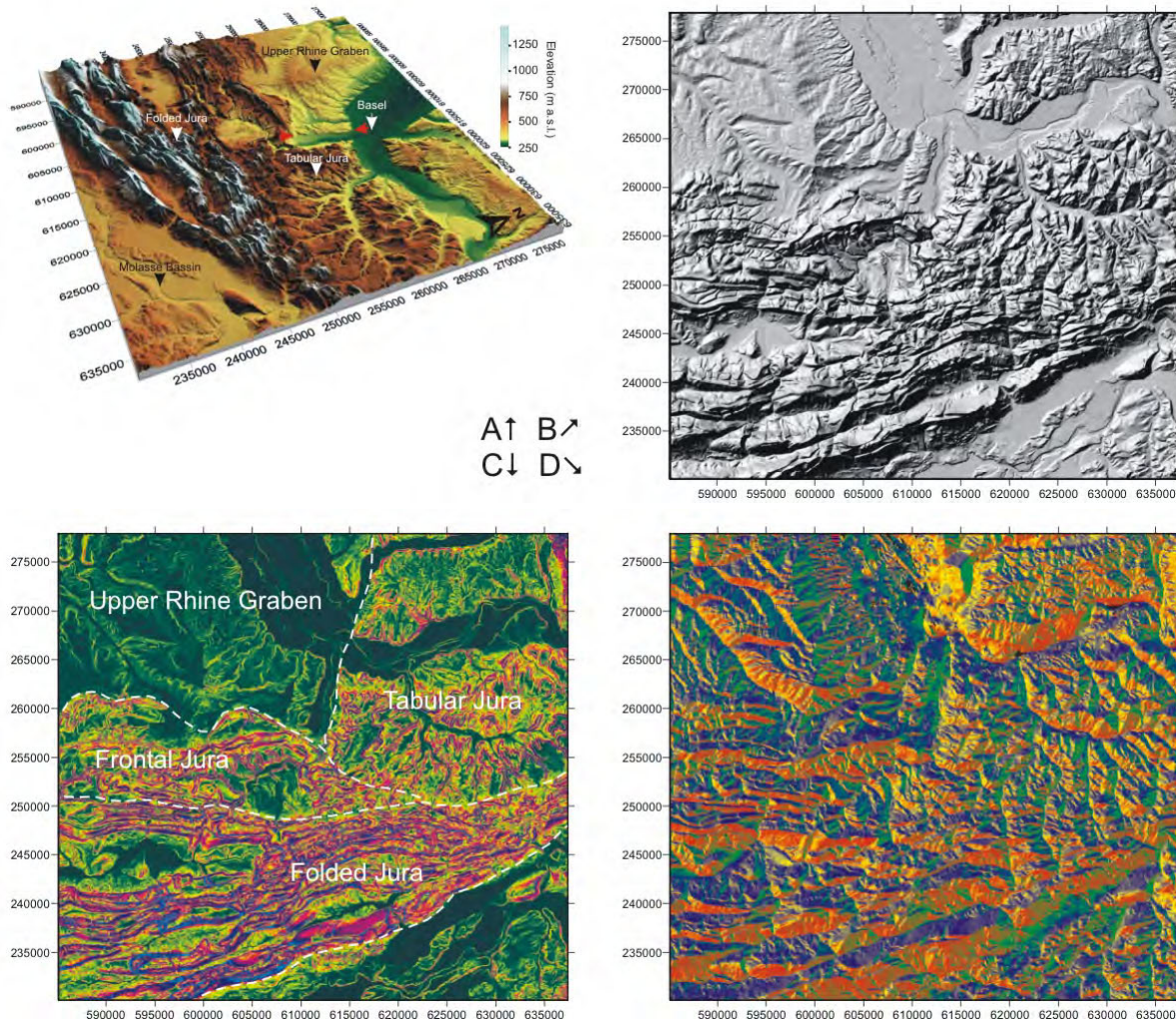


Figure 1.4. Basic representations and processing of digital elevation data with the example of the Basel area (dataset from the Federal Office of Topography, agreement DV1441). Coordinates are meters in the Swiss CH 1903 reference system (UTM projection). A) 3D perspective view with color coding for elevation. Red arrows indicate the Basel-Reinach fault scarp. B). Shaded relief illuminated under a NW-oriented 45°-inclined sun. C) Slope map showing a steep slope domain (pink to purple) corresponding to the Folded Jura and a flat domain (shades of green) corresponding to the southern Upper Rhine graben. Note the clear linear slope line outlining the Basel-Reinach fault scarp. D). Aspect map showing dominant north-facing (in blue) and south-facing (in red) slopes.

Digital elevation data may be simply gridded to display a landscape surface and give a better overview a region. Topographic data may as well be extracted to build profiles across interesting geomorphological structures to understand relationships between tectonics and sedimentation that may induce scarp asymmetry or regional tilting (see Fig. 3.6a in Chap. 3). Elevation data are most valuable when used simultaneously with geological data as they may reveal that a given unit lays at an anomalous position from one side of the fault to the other (see Fig. 3.6b in Chap. 3). Furthermore, standard processing may include terrain modeling such as slope, aspect (slope direction) or profile curvature (2nd derivative) calculations as

shown in Figure 1.4, as they may reveal hidden structures or provinces characterized by different parameters. Indeed, Fig. 1.4c displays a slope map of the Basel region which may be divided into four areas with different signatures. The Folded Jura displays aligned alternating bands of low (green) and steep (purple) slopes, thus marking its intensely folded structure. The Tabular Jura shows areas of constant slope which shape is similar to the drainage pattern, typical of tabular regions. The Upper Rhine graben is dominantly dark green, thus reflecting its flat nature due to active ongoing deposition of river sediments. Finally, the Frontal Jura exhibits a mixed signature, typical of a transition zone.

1.2.2.3. Aerial photography

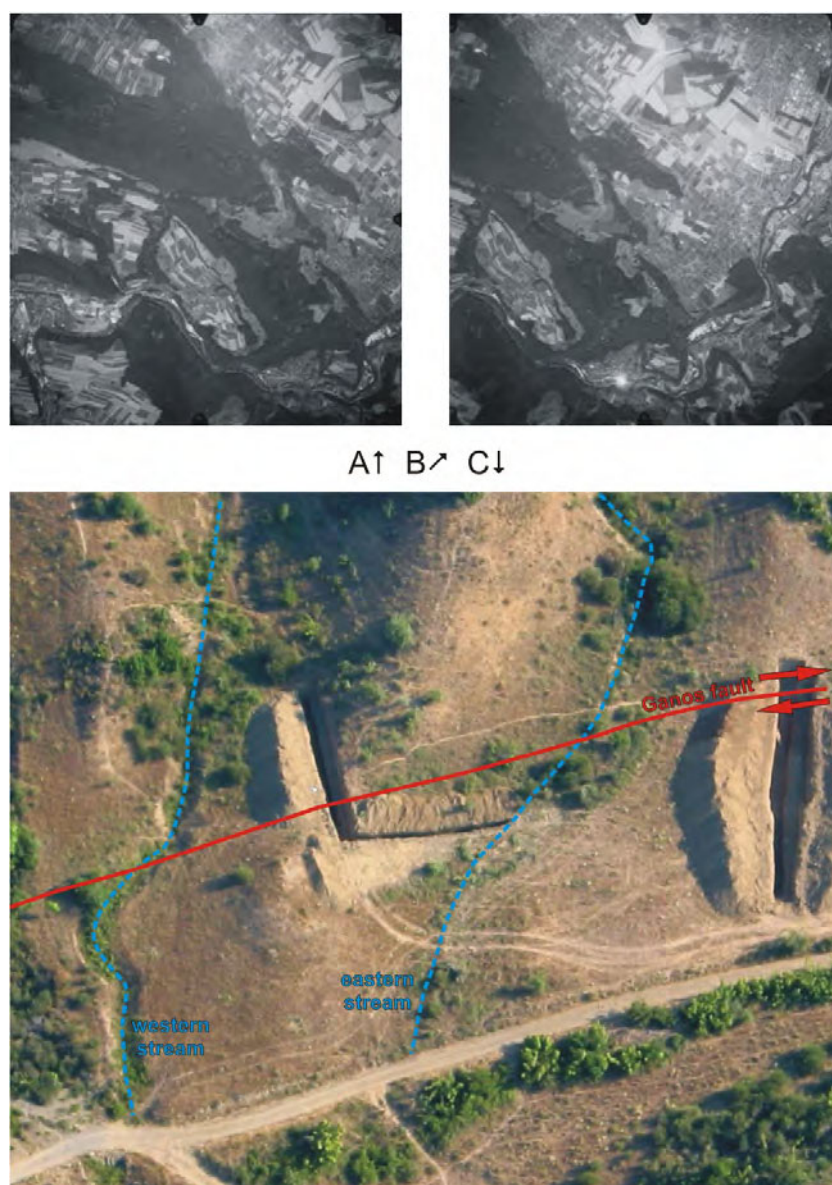


Figure 1.5. A) and B) pair of stereoscopic images of the Basel-Reinach fault scarp. High-resolution stereoscopic view reveals a faint N20 scarp which is hardly visible in the topography without vertical exaggeration. C) Aerial photograph of the Ganos fault at Güzelköy trench site, western Turkey. Blue streams (flowing from top of the picture) are consistently right-laterally diverted, thus suggesting they

may be displaced by a fault. Trench investigations revealed the presence of a fault (red line) with recent displacements. Scale is given by the main road, which is ~4 m wide. Picture was taken by Stefano Pucci (INGV Roma) aboard a paramotor.

Aerial photography has long been a basic tool for geomorphologists and paleoseismologists. These high-resolution pictures of the landscape can display features that cannot be seen in the field and may offer stereoscopic view which renders relief and textures with striking realism. Indeed, a pair of photographs taken with a slight gap mimics the natural human stereoscopic view. Features may then be described and separated on the basis of their texture (lithology and age), color (vegetation, i.e. lithology and hydrology), geometry (displacements or anomalous location) and relationships (chronology of deposition and erosion episodes). This makes aerial photography a premium tool for mapping geomorphological features such as incised streams, alluvial fans and river terraces prior to undertaking fieldwork. Nowadays, with the advent of meter-resolution satellite images (e.g., Ikonos and Spot 5), it may not be worth ordering an expensive special airplane flight anymore. Furthermore, satellite images come as a complete data set comprising various frequencies sensible to lithological and hydrological variations (see section 1.2.2.1.). However, in regions where an earthquake occurred recently, comparing readily available old aerial photographs with new ones –or with satellite images- may help determine places which underwent strong horizontal displacements and prepare fieldwork more efficiently. Following the dominant philosophy in paleoseismology, it is once again more efficient to combine information and take advantage of all available datasets. It should be noted that aerial pictures may also document field investigations. Indeed, some colleagues are developing tools to take real-time aerial pictures of trench sites during fieldwork periods. Stefano Pucci (INGV Rome, Italy) is preparing a PhD thesis on the use of a paramotor to take such pictures (see Fig. 1.5c). Similarly, Prof. R. Arrowsmith (Arizona State University) is developing a photographic system based on a digital camera attached to a 2-m-wingspan kite and triggered through a remote control (see World Wide Web Resources).

These various methods and sources of information may eventually lead to the identification of potentially active structures which would display evidence for recent deformation. In case no instrumental earthquake confirms this result or evidence is not strong enough, it may then be necessary to provide evidence for a structural continuation from surface features to a potentially seismogenic fault at depth. This may be achieved by means of geophysical imaging techniques such as seismics, electric tomography or ground-penetrating radar (GPR) as described in the following sections.

1.2.3. Geometry at depth and long-term vertical displacement: deep reflection seismics

In regions where no recent surface rupture has been observed and only historical earthquakes are known, a geomorphological signature is needed but not always enough to establish the presence of a fault (see Chapters 2 and 3). Reflection seismics with sufficient resolution, focusing on the first hundreds of meters below the surface may help strengthen the active fault hypothesis. Indeed, a seismic section perpendicular to the fault trend shall evidence faulted and displaced units which, on the basis of their age and amount of deformation, should document long-term vertical slip rate and, possibly, give an estimate of the beginning of activity on the fault. Indeed, abutting relationships may show that a group of units are similarly deformed, thus suggesting that deformation started, at soonest, after deposition of the last unit. Furthermore, it may help better characterize the fault over long-term and show vertical deformation on apparently strike-slip faults. The geometry itself shows the deformation style and may document more about the complexity of the fault system which may spread as a flower structure or be very concentrated. For example, it is most often uneasy to check whether a normal fault is listric at depth or not from surface observations. This is crucial point as it is directly linked to rupture width (or depth) and, consequently, to potential rupture area and pertaining maximum event magnitude.

1.2.4. Shallow geometry and recent displacement: sub-surface geophysics

Once a potential feature for a seismogenic source has been identified, paleoseismological investigations should focus on locating the most recent surface ruptures in order to plan excavations. High-resolution geophysics may help image the sub-surface and show recent displacements affecting shallow units that may be unearthed by trench investigations (usually, 2m to 5m-depth).

1.2.4.1. High-resolution reflection seismics

High-resolution seismics rely on acoustic properties of geological material, namely sound wave velocity and density, most frequently combined into acoustic impedance as a product of both. Sound waves of a given frequency (or frequency range) are emitted towards the sub-surface (ground or water) by means of a source (hammer, shotgun, weight dropper, dynamite or vibrating truck on-shore and dynamite or water or air-cannon off-shore). As waves travel through geological materials, they may encounter impedance contrasts and be either transmitted, reflected or refracted (or, most often, some of each) following Snell's law. Secondary waves may eventually be reflected back to the surface to be recorded by an array of simple seismometers (geophones). Alternative survey geometries and processing

techniques may lead to proper imaging of the sub-surface to help show the geometry of a fault zone (see Fig. 3.? in Chapter 3). Depending on the frequency used (and related seismic source), one may achieve various resolutions and pertaining penetration depth. Hence, a recent study unveiled original features as a wedge of sub-vertical low-density material surrounding the San Andreas fault (Hole et al., 2001). As a direct application to paleoseismology, Stephenson et al. (1993) evidenced recent surface faulting on the Wasatch fault, Utah, now buried below younger deposits. However, due to the limited practicable resolution, high-resolution seismics are usually valuable to locate a fault zone in its width but seldom to image clear recent ruptures, unless very high resolution can be achieved (e.g. with a transducer for river and lake investigations, see Schnellmann et al., 2003). Consequently, we have to turn to higher resolution techniques to evidence recent displacements prior to opening excavations.

1.2.4.2. Electrical tomography

As seen in the previous paragraph, seismics are generally not suitable to make the last link with the surface. However, resistivity soundings and their 2D version known as electrical tomography may image the underground continuously from 50 m depth to the surface with resolution up to 1 m; depending on survey parameters (see Chap. 3). Electrical tomography has fairly simple theoretical principles as it images resistivity (inverse of conductivity) of geological material by injecting a current of given intensity and measuring the resulting tension. As resistivity is the ratio of tension over intensity, resistivity may be calculated simply. The subtlety of the method comes with multielectrode equipment which may achieve hundred measurements per hour with little participation of the operator. Furthermore, with 24, 48 or more electrodes simultaneously available, the system may use the same electrode as an injection point then as a measurement point. This is highly convenient as it enables to test several survey geometries during a single measurement round through programmable scripts. Of course, measured resistivities are integrated over a slice of geological material and shall be considered as apparent values. Block modeling helps reconstruct a pseudo-section which quality (or representativity) may be estimated by a root mean square (RMS) difference between measured values and synthetic values produced on the basis of the pseudo-section. Typically, a proper RMS should be lower than 5%. Furthermore, the most widespread processing software called RES2DINV and developed by the Geotomo Company is not open source. Actually, its authors do not give details about their handling of known unstable boundary conditions which should be addressed (Maineult, 2003). Consequently, it may be recommended to focus interpretations on the central zone of a resistivity pseudo-section, discarding features located close to the limits, especially when they display unusual geometries.

Electrical tomography has been extensively used for hydrogeological and contaminant tracking purposes (Barker, 1990; Reynolds and Taylor, 1995). It is now starting to be deployed over active faults to provide information about their structure close to the surface (see Fig. 1.6 and Suzuki et al., 2000). Following its use on the Bree fault by Camelbeeck and Meghraoui (1998), we proposed to use it on the Basel-Reinach fault as well (see Chap. 3) as a decision tool to choose potential trench sites along the fault.

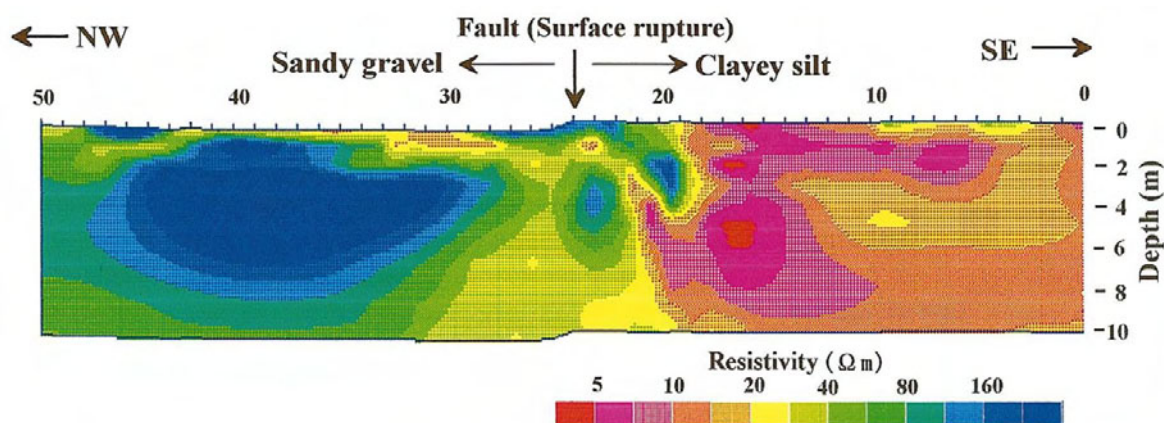


Figure 1.6. Electrical tomography pseudo-section across the Nojima fault zone, Japan. Section was modeled from 784 measurements performed with 50 electrodes (located at points 1 m to 50 m). Exactly below a 1-m-high scarp, produced by the 1995 Kobe earthquake, a strong resistivity contrast separates clayey silts from sandy gravels. That abrupt lithological change is attributed to cumulative slip on the Nojima fault. From Suzuki et al., 2000.

When interpreting resistivity contrasts, it is often uneasy to discriminate between a change in lithology and variations in hydrological conditions, though they might be correlated. Indeed, a porous geological unit may display a significantly different resistivity when dry or water-saturated (due to the mobilization of conductive salts). Hence, we established several recognition criteria to interpret the presence of a steep normal fault, as this was the preferred mechanism inferred from geomorphological observations in the Basel region:

- a distinctly vertically displaced resistivity unit,
- a sharp sub-vertical contrast separating two different units (lithological contact),
- a sub-vertical “intrusion” of low-resistivity material associated with water circulation and possible secondary clay minerals deposition along a fault plane (Fujimoto et al., 2000).

Thus, electrical resistivity soundings and tomography help make the link between shallow structures and their surface expression. Hence, a scarp morphology within a low seismicity region may be correlated to a well-expressed structure at depth (see Chap. 3).

Although, this does not link that very candidate to recent –or even historical- earthquakes as resolution is not adequate. Such a goal may be achieved –apart from trenching- by means of highly detailed geophysical surveys that ground-penetrating radar permits under favorable lithological conditions.

1.2.4.3. Ground-penetrating radar

Unlike electrical resistivity which deals with the conduction of electrical currents, ground-penetrating radar (GPR) is based on the propagation of electromagnetic waves. Indeed, GPR is basically similar to seismics using radio waves instead of sound waves with –most frequently- a single pair of source/receptor. As first envisioned by Davis and Annan (1989), radio waves with frequencies ranging from 10 MHz to 1 GHz are adequate to image resistive material (resistivity should be higher than 100 Ω .m at 100 MHz) with resolutions up to 10 cm, the classical penetration depth/resolution trade-off being a crucial survey parameter. Indeed, such high frequencies are strongly absorbed by geological material, especially by conductive ones which often form a more or less thick screen at the surface (wet clay and soil) in temperate regions. Hence, considering field conditions and the nature of the target to image, one should always choose the best compromise between resolution (see Fig. 1.7a) and penetration depth. That choice shall be the result of a well-understood process as GPR equipment might be bulky and unused antennae should be left at the laboratory. On the other hand, inadequate frequency may lead to a total failure of the survey.

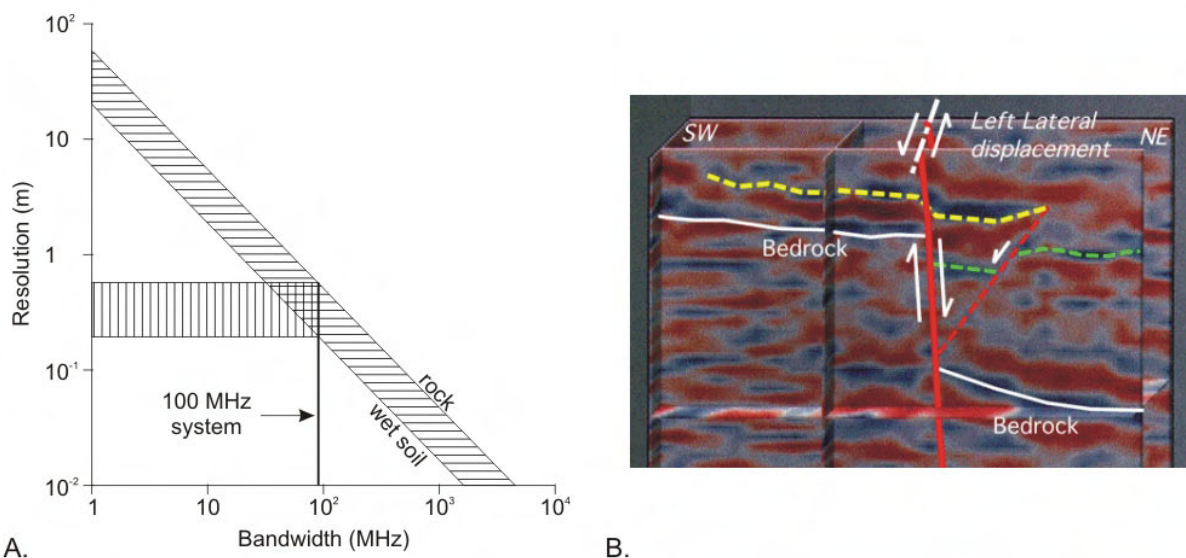


Figure 1.7. A) The relation between resolution and bandwidth and the usability of a 100 MHz system for rock and wet soil lithologies. From Davis and Annan, 1989. B) Example of a GPR section across the Neodani fault, Japan, which locally produced 3m of slip in 1891. From Hauser et al., 2001.

As GPR may image units as thin as several tens of centimeters, it has been thoroughly tested within known tectonic environments to locate old faults in hard rocks (Meschede et al. 1997) and recent vertical displacements in Quaternary units (Smith and Jol, 1995). Busby and Merritt (1999) lead an extensive survey of deformation styles within Quaternary glacial sediments and document numerous small-scale normal and thrust faults. Furthermore, GPR may be used to locate and identify secondary evidence for past earthquakes such as liquefaction features (Liu and Li, 2001) which –when available- are much valuable to estimate the intensity of ground shaking over a vast region, like the New Madrid seismic zone (Obermeier et al., 2001).

Apart from identifying fault zones, paleoseismological applications of the GPR method now include coseismic slip determination. Indeed, we successfully used GPR to detect and trace buried stream channels cut and horizontally displaced by the North Anatolian fault during the 1999 Izmit earthquake as well as during two previous events (see Chap. 4 and 5). As an additional result, we showed that it is feasible to use inexpensive time-saving geophysical methods such as GPR to complement -and even partly replace- classical excavations in regions where stratigraphy (layers thickness shall be larger than the vertical resolution) and slip parameters (slip per event shall be larger than the horizontal resolution) are adequate.

1.2.5. Recent cumulative displacements: micro-topography

Once a potentially active fault or scarp has been identified and located, fieldwork shall start with a microtopographic survey. Microtopography is the measurement of geomorphological features with a meter-order resolution (or better) and a centimeter-order accuracy (or better). This can be achieved through the use of a total station (or theodolite), a common tool for geometers. A total station (see Fig. 1.8) is a high-precision optical instrument used as a monocular. The station is installed at a fixed base where horizontality is set to zero and a given direction (preferably north) is set as origin. Then, an operator covers the study area with a reflector installed on top of plumb cane, which length is known. When a measurement shall be performed, the station operator targets the reflector and the station measures the horizontal and vertical angles with respect to the horizontal and origin direction (north) as well as the direct distance by means of a laser pulse. These three parameters are converted to (X, Y, Z) with respect to the station on the basis of simple geometrical relationships.

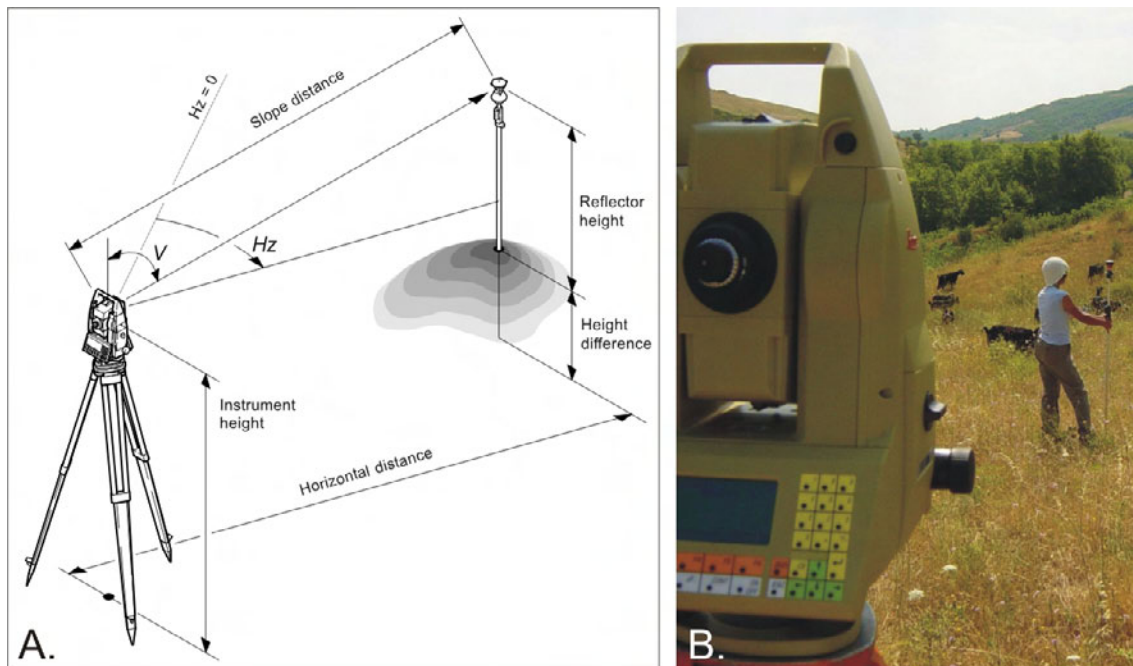


Figure 1.8. A) Principles of microtopography. Hz: horizontal angle with respect to origin. V: vertical angle with respect to horizontal. From Leica TPS1100 notice. B) Microtopographic survey using the Leica T1800 equipment. The total station (khaki green device in the front) is mounted on a stable tripod and is operated to follow the 3D reflector (red orange crystal-like accessory in the back) mounted on top of a plumb cane. The cane is carried around the survey area with adequate horizontal spacing.

The Leica T1800 we used in the frame of the present work was additionally equipped with a tracking system which would automatically search for the reflector and follow it between measurements. However, that special accessory relies on laser signals and is highly sensitive to ambient light and intense sunlight disables it. This allowed to measure up to 1000 points per day at the Güzelköy site, along the North Anatolian fault (unpublished data, see Fig. 1.8b, 1.9 and 1.10). Such a detailed topographic map is a valuable tool for locating and archiving all kinds of observations such as fault traces in trenches, trenches themselves, geomorphic features, samples, etc... Furthermore, they provide a record of recent past events and may help identify events too old to be properly preserved in trenches. Across normal faults, topographic profiles may display similar evidence as remnants of former scarps produced by vertical coseismic slip and partly eroded. The complexity of the scarp may help reconstruct several events with topography only (Meghraoui et al., 2000). However, dating such surfaces is generally difficult and, in most cases, performed through low-accuracy methods like cosmogenic nuclides concentration. Thus, microtopography shall be complemented by excavations.

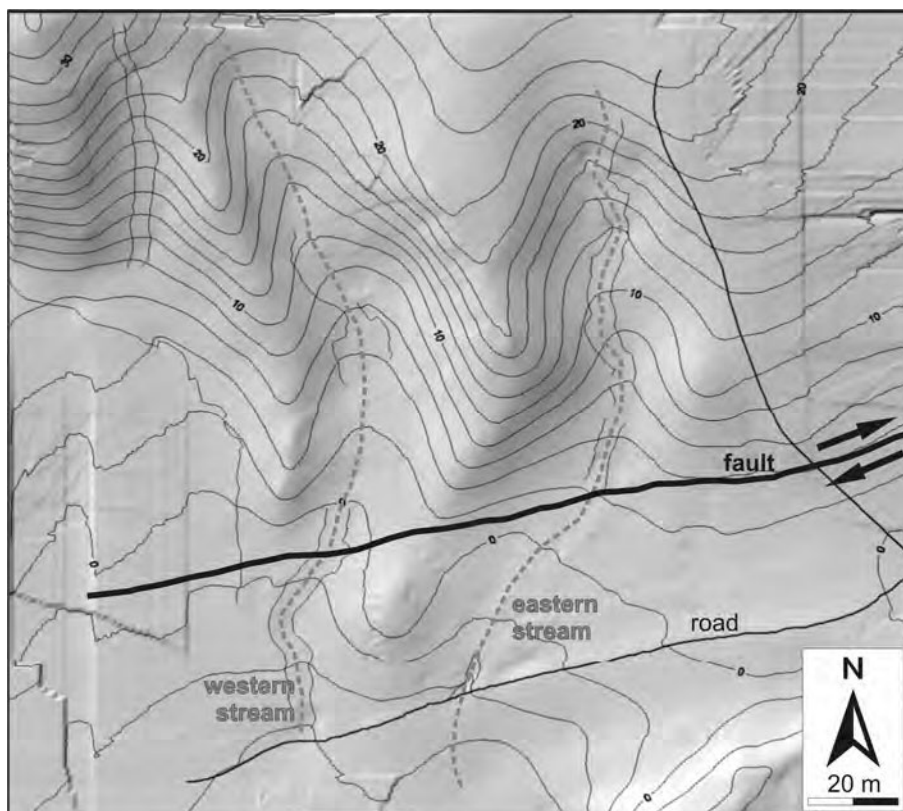


Figure 1.9. Microtopographic map the Güzelköy site, Ganos fault, western Turkey. Note the two deeply incised streams right-laterally diverted by the fault. The western stream experienced ~10 m of slip, i.e. 2-3 times the amount of slip produced by the last historical event in 1912. The eastern stream displays more than 20 m of lateral displacement, suggesting that at least 5 events were recorded at that site.

1.2.6. Recent history of sedimentation vs. surface faulting: trenching

Keeping in mind that the final goal of a paleoseismological study is to identify individual seismic events and determine slip per event and return period, one should eventually address the high-resolution geological record composed by most recent deposits deformed by the last earthquakes to have occurred on the fault. This may be performed by excavating large holes across the fault and parallel to it to describe relationships between geological units and faults. Here, we will expose the most commonly-used trenching techniques, most of them being standard for most paleoseismologists.

1.2.6.1. Making the most of a trench site: site selection

Planning a trenching campaign is heavy duty work. To optimize a trench, one should make sure that odds are good enough that the trench will display surface rupture and host suitable sediments to guarantee a proper record of events, in terms of stratigraphy (lithological

interfaces should be unambiguous) and datable material (probably the most luck-dependant parameter). As trenches may be hundreds of meters long, 2 m to 10 m wide and 2 m to 6 m deep, several hundreds of working hours may be necessary to complete the fieldwork. Thus, it is generally profitable to seek help from a group of 5 to 10 people (as we did in Turkey). If this is not possible, trenches should remain open for a longer period (as we did in Switzerland).

While planning an excavation campaign, one must take into account legal conditions. As we experienced, obtaining authorizations is a fairly quick and simple task in Turkey. Along the North Anatolian fault, inhabitants are sensitive to earthquake issues, especially since the destructive Izmit and Düzce earthquakes of 1999 which suddenly raised the question of seismic risk to Istanbul with great acuteness. People are usually very friendly and keen to participate to the effort by giving full access to their property, on a sole oral basis. The community authorities shall then be informed before work starts and often prove to be helpful in providing digging equipment and personnel. Additionally, Turkey is only little urbanized outside large cities and most land is used for agricultural purpose. Another parameter is the length of the fault. The Izmit earthquake produced some 115 km of surface rupture (Barka et al., 2002), thus offering numerous potential trench sites.

On the contrary, opening trenches in Switzerland is a long-term laborious process. The limited visible 8-km-length of the Basel-Reinach fault scarp combined with a high level of urbanization strongly limits the number of accessible sites. Additionally, the following procedure must be followed:

- Contact the county geologist. He has to be informed about any excavation deeper than 2 m and be provided with all pertaining observations and documents. He may make contacts with local authorities easier.
- Contact owner(s) for authorization. Properties are expensive in the studied region and often shared between several brothers and sisters who shall all be contacted. Answer(s) must be written.
- Contact the community for authorization. Usually, communities are positive as long as owner(s) agree(s) and may provide some field support. Allow a minimum of four weeks before starting work as the community publishes a legal description of planned work to let any community citizen the opportunity to protest.
- Contact the Forest Office. Unless the property is completely free of trees, they shall be asked for an authorization.
- Contact a construction company to rent a backhoe. These companies are usually busy in Switzerland and may ask for a delay before starting any new work.

To many respects -including location, accessibility, time schedule, sedimentary adequacy and legal issues- it is generally crucial to choose a trench site most carefully as the whole study may enter a dead-end or, at least, be postponed in case of failure. Furthermore, it is common knowledge that all parameters cannot be addressed prior to trenching and that, in the end, “Mother Nature is the only one to decide”. Thus, it is crucial that potential assessable risks of failure be identified and tapered.

1.2.6.2. Optimizing excavations: trench layout

Excavations shall be planned following parameters to document (chronology, slip per event...), site morphology, rupture geometry and style of faulting. On the one hand, normal and reverse faults, which exhibit mainly dip-slip movement, are usually best studied with a set of deep trenches perpendicular to the direction of the fault. On the other hand, strike-slip faults should be studied with fault-parallel shallow trenches to determine slip and perpendicular trenches to determine events chronology. However, as initial layout depends on surface information, it is often needed to open complementary trenches when first observations suggest the situation is less clear than first thought, which is generally the case.

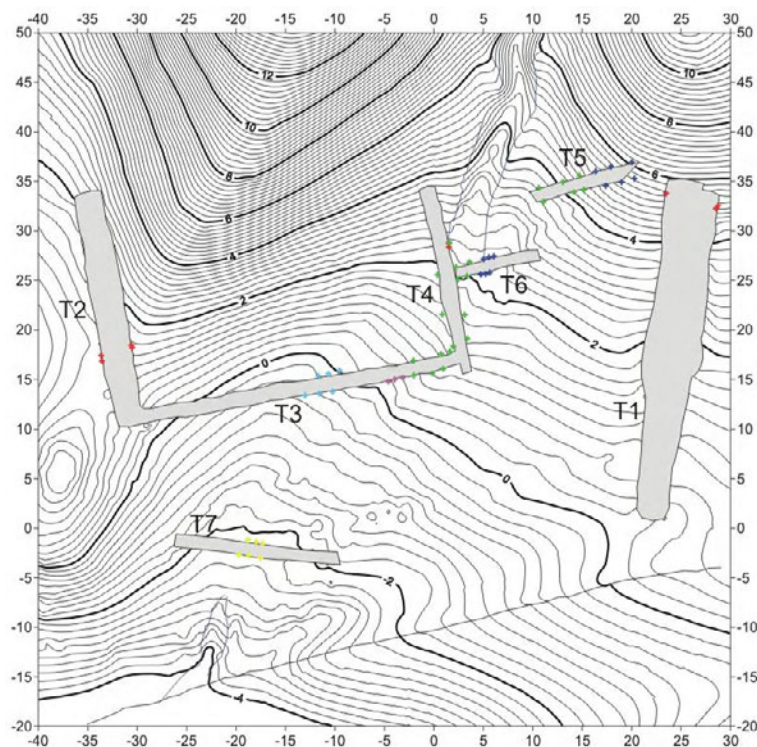


Figure 1.10. Topographic map of the Güzelköy, Turkey trench site. Grey shapes are trenches; colored dots are trench observations (red for fault traces, other colors for different generations of stream channels). Height curve spacing is 0.2 m. Local relative coordinates are given in meters.

In every case, trenches shall be designed in agreement with several base rules. Indeed, some standard guideline shall be followed to rule out incompatibilities with other trench studies and guarantee its quality with respect to research standards:

- trenches should be linear and connecting trenches should be perpendicular in order to avoid projection biases.
- walls should be vertical, continuous and planar (this is easily achieved in silts and sands, practically impossible in cobbles and boulders) for similar reasons and to avoid biases when setting up the grid and logging (see next section). The so-called “Japanese style” prefers walls at 45° for safety reasons. However, as this requires more time and work and induces a strong projection error, it is only rarely used. Alternatively, unstable walls can be reinforced with hydraulic shores (this is compulsory for excavations deeper than 2 m in Switzerland).
- the soil cover shall be cleanly cut and not ripped off as it will serve as a reference for logging and its subtle topography may indicate buried faults. It should be preserved and put back in place after backfilling trenches, especially when working on agricultural land.
- dirt piles shall be stored at least 2 m away from the trench for safety reasons (overloading) and to leave a proper pathway for workers. Furthermore, one shall consider opening further excavations and make that deposits location would not interfere.
- a gentle slope shall be laid out at an end (or both ends) of the trench to provide easy access and exit, especially in case of emergency. Indeed, it may happen that a trench is flooded within a few minutes by a strong shower (as it occurred at the Köseköy, Turkey, trench site in July 2000).

Additionally, obvious safety measures should be followed. When working in deep trenches (>2.5 m), we highly recommend to wear a hard hat as a common 10-cm-wide pebble falling from a height of 1 m is sufficient to cause noticeable annoyance. Furthermore, repeated use of scraping and cleaning tools may be damaging for hands and gloves shall be considered a basic protection. It is also recommended to avoid large groups inside trenches and, above all, to avoid large groups on the edge of a trench as they unexpectedly overload unstable material.

1.2.6.3. Acquisition of trench data: logging and sampling

Classical observation techniques of Geology include description of natural outcrops and sampling of rocks and sediments. It may then seem unusual to fabricate artificial outcrops like trenches. Actually, as fault zones are usually narrow and affect young –i.e.,

unconsolidated- sediments, natural outcrops are very scarce (e.g., incising stream beds) and most frequently poorly adapted. Hence, it is a best choice to open temporary optimized observation windows in the ground with some control over the sedimentary record. Following data collection is then rather classical as it comprises logging on graph paper, photomosaicing and sampling.

1.2.6.3.1 Logging

Logging is the process of reporting information from outcrop to paper with the greatest accuracy. Obviously, this is a decisive point of our approach as trench logs are the core evidence to be presented to the scientific community. They document events chronology and magnitude and shall be as little ambiguous as possible. However, in places where stratigraphy is complex and unclear, it may happen that interpretations slightly differ. A trench log is always a synthesis of background knowledge, experience, observations and interpretations. In that sense, it is not a raw data set like photographs or samples may be.

Before all, trench walls shall be cleaned from any traces left by the mechanical shovel (scars, clay packs, corrugations) and checked to locate important features (faults -main, secondary, synthetic and antithetic-, event horizons, etc...). Then, a string log shall be installed on one or both walls. That grid may be 50 cm x 50 cm or 1 m x 50 cm, and supported by nails which size and diameter is adapted to the sedimentological content. Setting the grid requires a real horizontal line provided by a water level (basically, a transparent hose filled with water) along with smaller line levels for selective checks. Vertical direction may be provided by a standard plumb line.

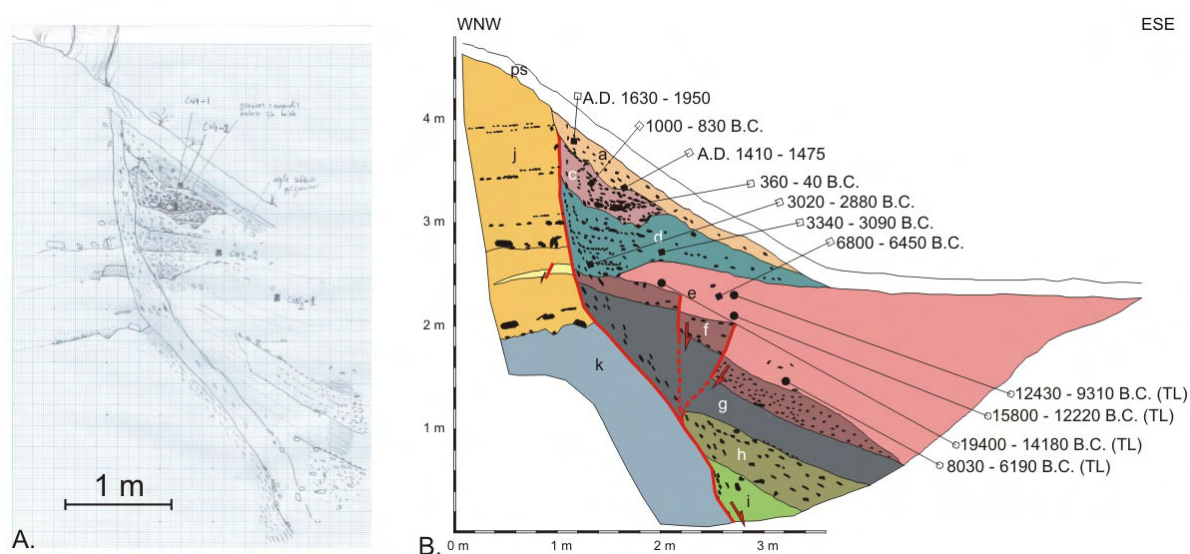


Figure 1.11. A) Raw paper log of the fault zone displayed in Trench 4, Basel-Reinach fault, Switzerland. B) General trench log of Trench 4, Basel-Reinach fault, Switzerland drawn on the basis of the raw log, the photomosaic and further field observations.

Trench logs shall be adapted to what should be shown, to the geometry and dimensions of the trench and to the level of detail provided by the stratigraphy. Usually, a 1:20 scale is recommended in most situations with larger scales for general logs (a 100-m-long trench fits a A3 sheet at a 1:250 scale, or 1:100 if the log is cut into three segments) and smaller scales for zooms over fault zones where stratigraphy (or events) may be too thin to be properly drawn (at a scale of 1:20, a 0.5 mm pencil strike represents 1 cm). Logs should be drawn on graph paper with a dry paper pencil. The logger should take proper references like grid nails to start with and report surface topography and trench bottom. Usually, two people are needed to log a trench. The drawer stays outside of the trench, makes observations, locates important features and reports them on paper while the measurer -inside of the trench- gives accurate feature coordinates within the grid reference frame along with details about texture and sedimentological content. Both work together to spare time and minimize the impact of personal interpretations.

1.2.6.3.2 *Photomosaicing*

Trench logs are very valuable pieces of data but remain somehow interpreted in ambiguous places and do not display entirely raw observations. However, photographs may provide objective information to discuss and to preserve for later verification and office work. With the advent of digital photography, it has been made incredibly easier to shoot several hundreds pictures a day and merge them into a mosaic of a 1 m to 2-m-wide and 20 m to 50-m-long trench to have a general view of processes at play.

The main caveat with taking pictures for a mosaic is optical distortion. Trench walls are supposedly planar whereas camera lenses are convex. This induces some distortion that may be critically high at the edges of the picture at wide angles. However, in narrow trenches, taking pictures at a wide angle helps minimize the number of shots needed to cover a wall and, thus, the amount of time devoted to that task. Here again, the right trade off should be chosen between time and quality. As pictures are most often some of the only genuinely raw data retrieved from trenches, we would strongly suggest that quality should be a priority for the present matter.

Taking into account final display size and print scales, individual photographs do not need high resolutions. Typically, with a 50 mm focal length, pictures taken at 1 m distance cover about 65 cm by 45 cm of usable surface (i.e., surface exhibiting low distortion). Setting the digital picture size to 640 by 480 pixels (lowest resolution available on most cameras) results in a resolution of 1 mm/pixel, far more than needed. Furthermore, such a picture file weights ~60 kb once saved in jpeg format, representing ~20 MB for a 300-picture mosaic like the one shown in Figure 1.12. Once assembled into some illustration software (e.g. Adobe Illustrator,

Corel Draw, Macromedia Freehand), the file weight increases by ~20%. For large mosaics, the final document may be over 100 Mb, which requires lots of computer resources and slows down considerably most standard computers. Higher resolutions are thus useless or for zooming purposes on specific areas of the trench only (e.g., fault zones and event horizons).

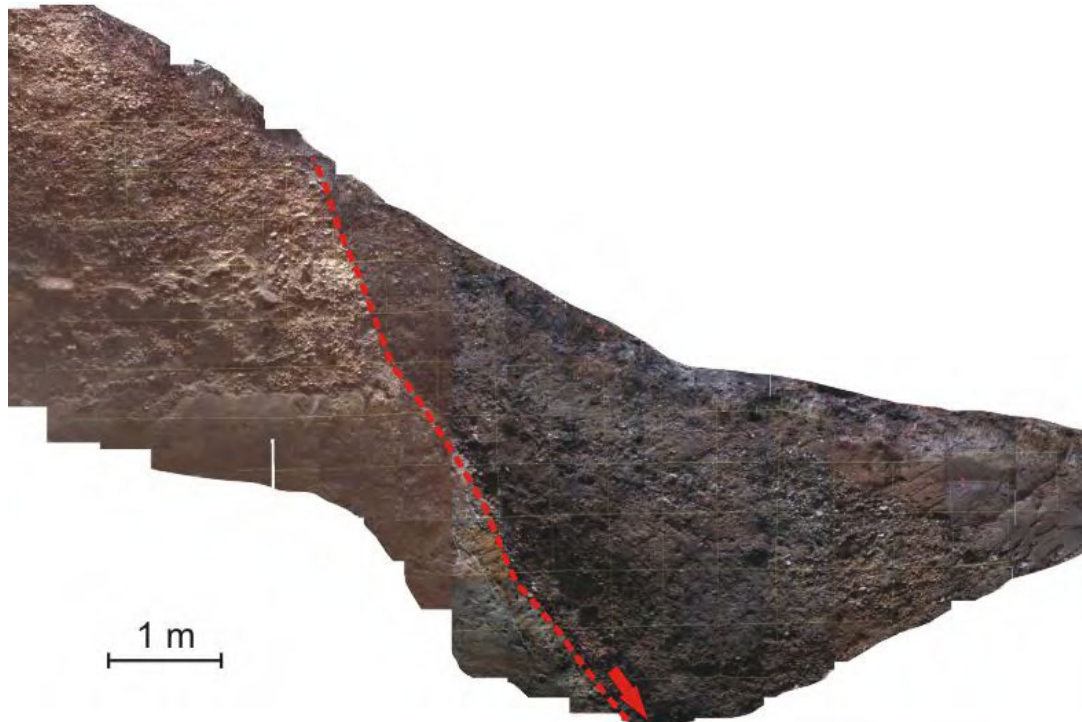


Figure 1.12. Photomosaic of Trench 4 excavated across the Basel-Reinach fault, Switzerland. The fault is clearly visible as a lithological contrast between light yellowish late Pleistocene gravel units on the footwall block and dark brownish Holocene clay and silt on the hanging wall. The mosaic was created from 300 digital pictures (640x480 pixels) shot in a 1-m-wide trench.

Besides being a precious archive for trench investigations, photomosaics are more and more used for field work. Indeed, during a field campaign within the RELIEF project along the Ganos fault, Turkey (unpublished data), we cleaned and gridded trench walls immediately after completing excavations and shot photomosaics systematically. Two to three people would focus on taking pictures while two more people would assemble mosaics and print them on A3 sheets. One single person -instead of two- could then draw trench logs over printed photomosaics, gaining much time as most features were already displayed, allowing more time to work on critical features related to seismic events identification.

1.2.6.3.3 *Dating*

As seismic hazard assessment strongly relies on recurrence intervals (or return periods), dating events is a central issue for paleoseismological studies. In regions of high seismicity, where several events occurred during historical times, dating may be partly achieved by means of historical documents and archeological findings. For instance, in Turkey, an Ottoman Canal built in A.D. 1591 crosses the North Anatolian fault and is faulted and displaced in several places (see Chap. 4 and Chap. 5). That canal provides a rare time mark to bracket the slip history on that part of the fault. Most frequently, dating is based on in-situ material exposed in trenches or on geomorphic features. Obviously, dates can only be inferred for datable materials. Accuracy and time-range of datations depend on the method used which, itself, depends on the available material. Organic compounds like bones, teeth, snail shells, charcoal chunks and soil may be dated through radiocarbon analysis whereas fine silts may be dated by thermoluminescence. Beside these absolute dating methods, one has sometimes to rely on relative methods like palynochronology, where pollen is available and properly preserved.

1.2.6.3.3.1 Radiocarbon

Living organisms of all kinds and size (from microbes to plants and animals) assimilate carbon throughout their lifetime. Atmospheric carbon is composed with three isotopes: ^{12}C (98.89%), ^{13}C (1.11%) and ^{14}C ($10^{-10}\%$). They are absorbed following their concentration in the air, which varies through time. ^{14}C is the product of interactions between ^{14}N and cosmic rays in the stratosphere (75%) and upper troposphere (25%). ^{14}C is rapidly oxidized to ^{14}CO , then to $^{14}\text{CO}_2$ before entering the global carbon exchange cycle. It may then be easily absorbed by plants as a base brick for photosynthesis and, thus, enter the food chain to accumulate in upper species. ^{12}C and ^{13}C are stable isotopes whereas ^{14}C is radioactive and decays back into ^{14}N with a half-life of 5730 years, as described by the radioactive decay equation:

$$N = N_0 \times e^{\left(\frac{0.693 \times t}{T_{1/2}} \right)}$$

where: N_0 is the initial number of atoms,
 N is the number of remaining atoms at time t ,
 t is time,
 $T_{1/2}$ is the half-life.

As the concentration of remaining radioactive isotope decreases by half after one half-life, N_0 may be out of instrumental detection threshold fast or hidden by modern carbon. This currently limits the applicability of the method to the last 55'000 years. For long, ^{14}C

concentration measurements were performed by counting decay hits with a Geiger device. This could take a long time and lead to poor accuracy as it understands that decay rates should be constant. Nowadays, Accelerated Mass-Spectrometers (AMS) enable fast and accurate measurements of the whole carbon content for a sample (see Fig. 1.13). ^{14}C measurements are faster, more accurate and may be quality-checked with ^{13}C content. Furthermore, while several hundred grams were required for conventional method, only 1mg of pure carbon should yield a proper result with AMS.

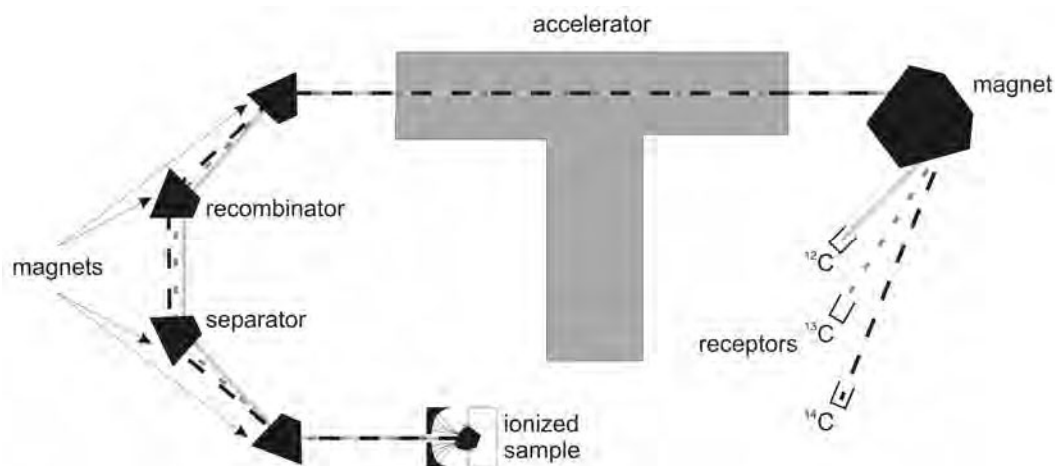


Figure 1.13. Schematic diagram of an AMS device. The sample is ionized and particles are driven towards a group of magnets. Isotopic fluxes are separated and cleaned as elements heavier than ^{14}C (typically oxygen and iron) are ejected from the trajectory by their higher inertia. Fluxes are then recombined to be equally accelerated. A stronger magnet separates isotopes and directs them to individual receptors for counting.

Once isotopic concentrations are measured and corrected, the radiocarbon age of the sample may be calculated. It reflects the decay history starting with a given concentration of ^{14}C in the atmosphere. This is actually not completely true. Indeed, isotopic ratios vary through time as a result of variations in atmospheric temperature, pressure and ^{14}C production rate in the upper atmosphere (following variations in the intensity of cosmic radiations). Hence, it is most important to correct for that phenomenon before comparing to dates as usually handled. That correction is called calibration. It is performed through a coral and tree-ring database which links calendar years (as a couple of a warm and a cold season) to a specific ^{14}C content (see Stuiver et al, 1998 and Fig. 1.14). Contrarily to ages BP (Before Present), dates BC/AD may be compared to historical documents, archeological findings and other absolute datation methods.

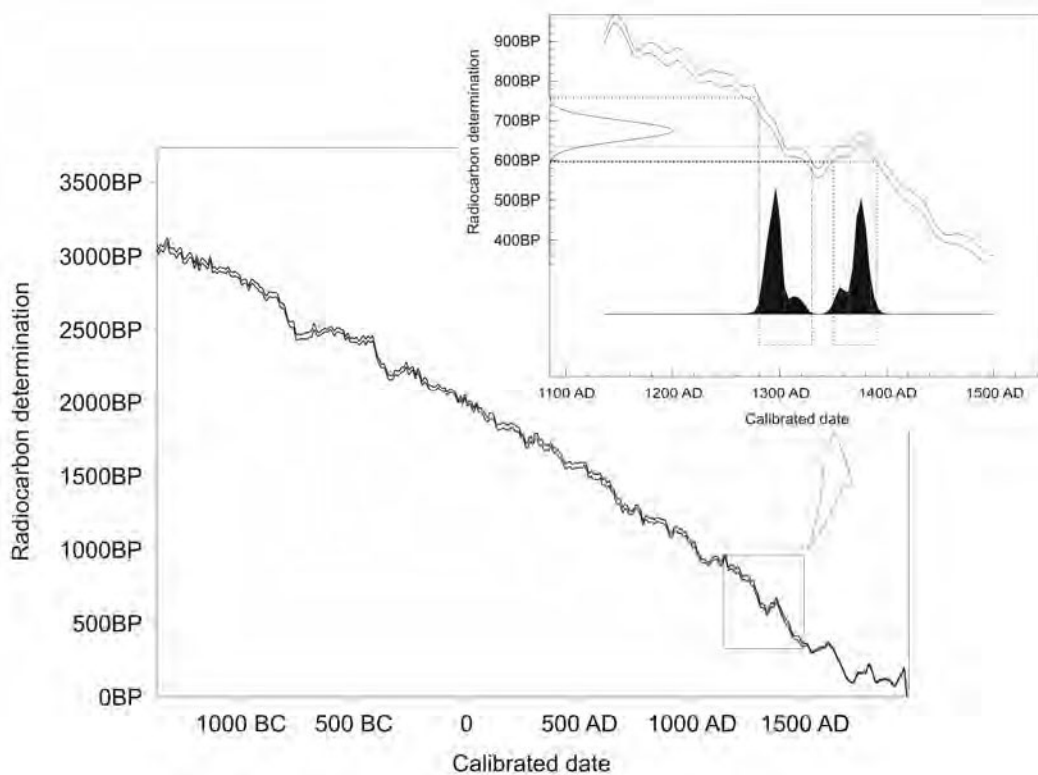


Figure 1.14. Calibration curve between 1400 BC and today (After Stuiver et al., 1998) and example of a calibration result (inset). We calibrated the age 675 ± 25 BP and present results for 1σ in grey (68.2% probability that true age is comprised between AD 1280 and AD 1305 or between AD 1365 and AD 1385) and 2σ in black (95.4% probability that true age is comprised between AD 1280 and AD 1330 or between AD 1350 and AD 1390). Because of a local minimum in the calibration curve, two peaks show up after calibration, thus leading to a wide time bracket.

Before all, as for any dating method, one should always have in mind the representativity of a given sample. Indeed, choosing the right material to sample and date may turn out to be no easy task. Charcoal bits are usually considered as high quality samples as they represent a short time window (a 1-cm-thick piece corresponds to 3 to 10 years) and yield a large quantity of carbon, with pertaining high accuracy. However, original wood may be decades or even centuries older than the time it was burnt into charcoal. Similarly, bulk soil is seen as second choice material as it contains only low amounts of carbon. Their major asset is their in situ formation that binds them to their geological unit. Let us say that many radiocarbon specialists elect peat as the best material for paleoseismic investigations. Peat is formed in situ by the accumulation of organic matter and displays high carbon content. The inevitable caveat being that peat requires specific conditions to form and is only rarely present.

For various reasons, organic compounds may have been leached off from a stratigraphic unit (acid groundwater) or –most commonly- may have never deposited at a site (i.e., in arid regions). One should turn to other datation methods to make the best out of available materials. Thermoluminescence (TL) addresses that issue for very fine-grained silts and buried soils, stalagmitic calcite and heated flint and stone. Natural radioactive elements like ^{238}U and ^{232}Th decay in the environment and release electrons which migrate to the surrounding material. Minerals based on silica (most commonly quartz and feldspars) host defects within their crystalline structure (lattices) where electrons may accumulate. The longer they are exposed, the more electrons are trapped. Controlled heating causes vibrations in the lattice and may then excite these electrons to emit light. The intensity of the signal is proportional to the time of exposure to natural radiations. The interesting point is that exposure to light reduces the TL signal down to a well-defined residual level, i.e. resetting the clock to zero. It is basic principle for the method that most lattices are exposed to light before the grain is deposited and buried. This limits the applicability of the method to silica-base very fine-grained material accumulated at a low rate of deposition (e.g., eolian silts).

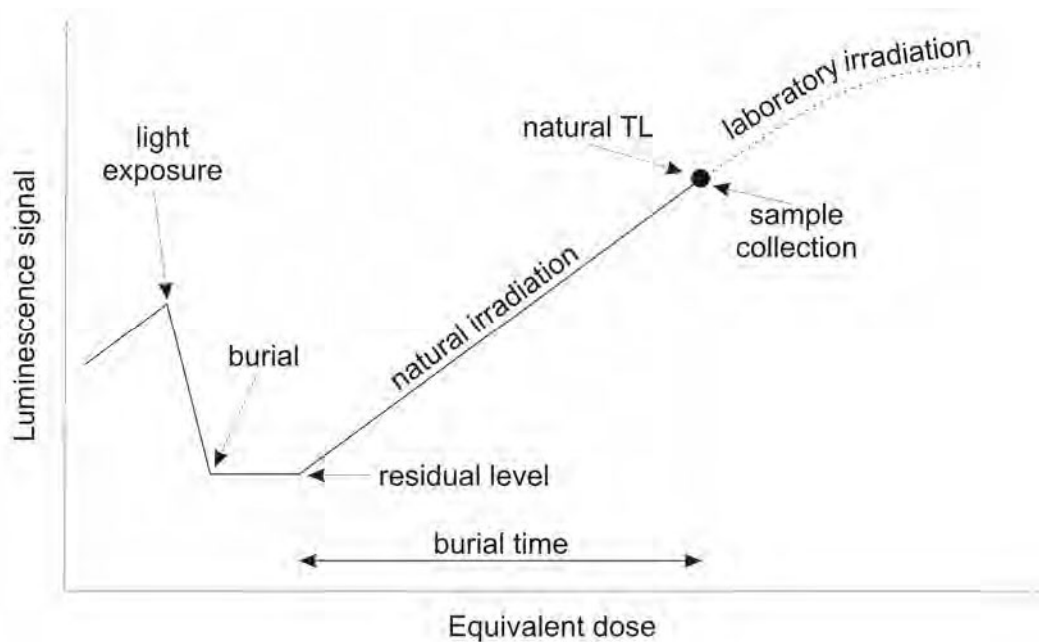


Figure 1.15. The TL geological cycle. After exposure to solar light, the TL “clock” is reset to zero (residual level). Following exposure to environmental irradiation, the equivalent dose increases linearly with time. Modified from Wintle and Huntley, 1982.

Although TL principles seem rather simple, the method itself contains numerous sources of errors. Beside laboratory measurement corrections and difficulties to interpret results, in-situ conditions must be addressed and fully understood before using TL at a given site. Indeed, i) the supposed depositional environment must ensure solar resetting of the TL

signal, ii) the solar resetting event must be understandingly linked to the geological event to date, iii) sediment samples must be protected from light during collection, iv) soil B horizons should not be sampled and v) dose rate heterogeneities should be minimized.

Provided that field and laboratory criteria are properly fulfilled, TL ages may be converted to calendar dates by subtracting the current year, as no calibration is needed. Some authors claimed to have dated loess units as old as 800'000 years (Berger et al., 1992). However, it is generally accepted that TL gives consistent and reliable results for materials not older than 120'000 years, which is more than enough for paleoseismological purpose.

1.2.6.3.3.3 Cosmogenic nuclides

The Earth's surface is under constant irradiation by cosmogenic rays. They interact with matter to form new cosmogenic nuclides by nuclear reactions. Thus, ^{40}Ca , ^{39}K and ^{35}Cl may be transformed to ^{36}Cl in calcite while O and Si may be transformed to ^{10}Be and ^{26}Al , respectively, in quartz (Lal, 1991). As cosmic rays do not penetrate deeper than a few meters, only rocks exposed at the surface are prone to experience cosmogenic nuclides production. The accumulation reflects the exposure time of the geomorphic surface since its deposition (alluvial terrace) or denudation (fault scarp). Dating alluvial terraces helps determine long-term slip rates on fast active faults (Van der Woerd et al., 1998) while sampling a vertical profile on an active normal fault may help identify denudation events associated to coseismic slip (see Fig. 1.16 and Benedetti et al., 2002).

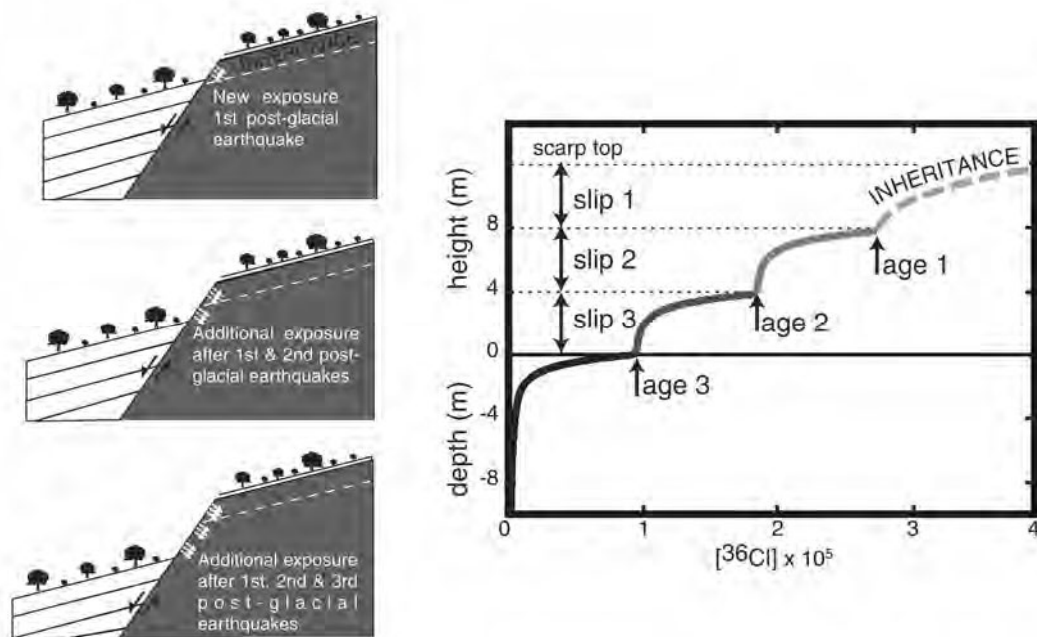


Figure 1.16. Principles of cosmogenic nuclides analysis for paleoseismic investigations on the Sparta fault, Greece. Each coseismic slip event denudes an additional exposure surface to cosmic rays

bombardment (left). ^{36}Cl concentrations (right) reflect sudden increases associated to sub-vertical movements on the fault. From Benedetti et al., 2002.

1.2.6.3.3.4 Palynochronology

Previously exposed datation methods are absolute, in the sense that they provide dates. However, datable materials are not always available and relative dating may be considered a valuable alternative. Among them (paleomagnetism, magnetic susceptibility...), we chose to describe palynochronology as it appears to be well-adapted to paleoseismic events determinations. At a given site, botanical diversity depends mostly on climatic conditions. As climate changes from polar to temperate or arid, vegetation adapts: species decrease or disappear and species emerge. Considering these vegetation changes are homogeneous over a region, tracking variations in pollen concentrations may help correlate sedimentary units across several lakes, peat bogs or sag ponds, for instance. Available absolute dates may then be merged to calibrate pollen curves and estimate ages for identified events (Becker et al., 2002). Still, some caveats occur as the pollinic record must be long enough to ensure a proper correlation with existing data (typically, over 1 m thickness) and pollen grains must be well preserved to reflect their origin species during identification.

The same kind of approach applies to magnetic susceptibility which reflects small changes in the Earth's magnetic field at the time of deposition. A proper record of magnetic susceptibility variations needs very fine-grained sediments depositing in a calm environment, i.e. in a lake, and may not be used for trench investigations.

1.2.6.4. Identification of a paleoseismic event: criteria

There are numerous branches of Earth Sciences involved in paleoseismological investigations. Each of them focuses on specific aspects of the geological record to retrieve events information and needs to compare observations to standard criteria to be able to link events to earthquake occurrences. These criteria are –obviously- different for lakes (seismites), caves (damage to speleothems), rock falls (trapped soil) and active faults. We will concentrate here on criteria that should be addressed when investigating fault excavations (trenches). The unique advantage to excavate trenches across surface rupture is the primary nature of the data. While off-fault observations often remain questionable about their triggering mechanism (storms can strongly disturb recent lake sediments, slowly flowing ice or mudpacks can easily break speleothems, rock falls usually happen during huge rainfall), excavations give a direct access to the seismogenic fault.

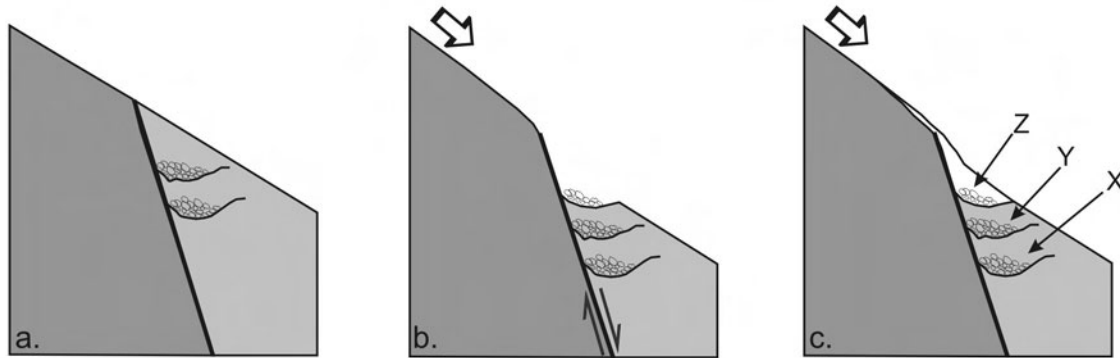


Figure 1.17. Recording of vertical movement on a normal fault. a) fault is pre-existing and close to the surface. b) an earthquake occurs and vertical displacement creates disequilibrium in the slope profile. c) over several weeks to years, the scarp is eroded and sediments are deposited on top of the hanging block.

There are several standard criteria that permit the identification of a seismic event in the frame of trench investigations. At that stage, let us consider that trenches have been opened across an active seismogenic fault and that local deformation is primarily due to faulting. Earthquakes may induce various symptoms to be observed and interpreted: faulting and displacement of geological unit(s), ductile warping of fine-grained layers, opening and filling of cracks and fissures and/or liquefaction of sand units. Whatever the feature, the common ground is to demonstrate that one or several of them formed at a given moment. This rely on abutting relationships which help identify the unit last deposited before the event and the unit first deposited afterwards, also called “event horizon”. Dating both units gives a time bracket pointing to the occurrence of the event.

1.2.6.5. Optimizing dates: the Bayesian statistical analysis

Calibration of radiocarbon ages to calendar dates does not yield results under scalar form but as probability distributions that correspond to 1σ (68.2 %) or 2σ (95.4 %) confidence intervals. Litton and Buck (1995) showed that a classical probabilistic approach called Bayesian statistical analysis could be applied to radiocarbon calibration in order to restrict probability distributions, with some limitations (Steier and Rom, 2000). The approach consists in building a relative a priori chronological sequence that integrates radiocarbon and thermoluminescence ages (on the basis of stratigraphic relationships between corresponding layers) as well as faulting events (following abutting relationships). The Bayesian analysis focuses on overlapping probability distributions to separate different samples and merge similar ones. Resulting dates for faulting events have a lower precision and but a narrower time range. Moreover, it is possible to compute the internal consistency of individual samples and events within the sequence model. For the Basel-Reinach fault study (see Chap. 2 and

3), the Bayesian statistical approach permitted a better correlation of events across different trenches and different sites and strengthened the events chronology during the Holocene. Additionally, it showed that our radiocarbon dataset was highly consistent, without any probable inversion, and that interpreted events chronology was reliable.

1.2.6.6. Improving data quality: multiarchive study

Excavating a trench and observing deformation may not be sufficient to characterize paleoseismicity in a region. For an event to become a paleoearthquake, consistent observations should be performed in several trenches at a single site and at different sites along a same fault or fault segment. Indeed, it must be shown that the rupture propagated to the surface over a measurable length of the fault to properly estimate a paleomagnitude. Local variations in rupture mode and sedimentary processes may lead to some differences in the earthquake history recorded at distant sites. Indeed, though rupture distribution along a fault or fault segment usually varies continuously, some local large variations are frequently observed (Barka et al., 2002). It may as well happen that deposition conditions may change from one event to another and local sedimentary record may turn out to be incomplete. Generally speaking, the lack of evidence does not mean that no event occurred. However, the overall pattern should match to strengthen the interpretation of corresponding events.

It may as well be interesting to compare and correlate different independent geological archives where events could be identified in lakes, caves and/ rock falls (see Chap. 3 and Becker et al., sub.). In regions where such archives are available, an integrated study may help describe prehistorical earthquakes in term of intensity and damage area. Indeed, fine-grained lake sediments are highly sensitive to seismic shaking and seismites (e.g., mixed layers) may point to shaking events. Furthermore, lake sediments are usually well-layered, deposit at a fairly constant rate and display a rather high organic content. Hence, they may yield much better age constraints once a correlation has been firmly established. It should be noted that some rare strong earthquakes do not produce noticeable surface rupture. Active fault methods, and especially trenching, are then useless and may be replaced by alternative methods such as investigations of soft-sediments deformations in lakes (Schnellmann et al., 2003).

Chapter 2

Active Normal Faulting in the Rhine Graben and Paleoseismic Identification of the 1356, 10=IX-X, Basel Earthquake (Central Europe)

*Meghraoui, M., Delouis, B., Ferry, M., Giardini, D., Huggenberger, P., Spottke,
I.
and Granet, M.*

(Science, 2001, Volume 293, pp. 2070-2073)

Summary

An active normal fault has been identified in the epicentral area of the 18 October 1356 Basel earthquake, the largest historical seismic event in central Europe. The east dipping normal fault forms a 8-km-long escarpment, NNE-SSW trending with a 30-50 m topographic relief in the Birs Valley. Paleoseismic investigations using geomorphologic analysis, geophysical prospecting and trenching were conducted across two main fault branches that reach the surface. Faulting episodes in trenches indicate that at least three seismic events occurred on the fault in the last 8500 years; the youngest event is dated shortly before 1410 – 1475 AD and corresponds well with the 1356 Basel earthquake (Io=IX-X MKS). These successive ruptures on the active fault indicate the potential for strong ground movements immediately south of the city of Basel and provide new elements for the seismic hazard evaluation along the Rhine graben in central Europe.

Introduction

Earthquakes of the last ten years (Northridge 1994, Kobe 1995, Izmit-Duzce 1999 and Bhuj-India 2001) remind us how fragile the urban environment is to the earthquake hazard. Two main issues in particular emerge: (1) In order to understand the damage produced by past earthquakes and to forecast future earthquake scenarios, a detailed understanding of potentially active faults and related seismic source behaviour is required, which all too often is missing for large historical earthquakes; (2) Areas with low-to-intermediate seismicity level and related hazards are very vulnerable to large earthquakes, as the basic knowledge on active faults required to understand the earthquake process is lacking, expectations for earthquake hazard are low and building protection is also low.

These issues are exemplified by the earthquake that on October 18, 1356, damaged large parts of the upper Rhine graben and destroyed the city of Basel (Figures 1a and b). The largest known earthquake of continental Europe, with an epicentral intensity MSK=IX-X and an estimated 6.0 - 6.5 magnitude, the 1356 Basel event benefits of a relatively rich historical accounts (1). A detailed spatial description of damage to the medieval castles and churches reports 60-80 castles destroyed within a ten km radius from Basel and damage to towers and churches to a distance of 200 km (Figure 2). Today, Basel is a key communication node at the center of an important multinational (France, Germany, Switzerland), high-technology and industrial zone, with several critical facilities in the area (nuclear power plants, chemical industry). Building damage in Switzerland due to the repetition of the 1356 event today would amount to 50 M US\$ (2).

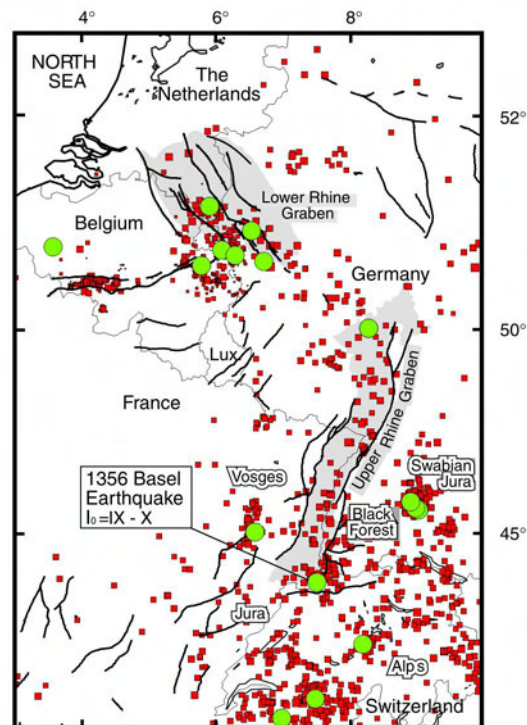


Figure 1. Seismotectonic framework of the central European region around Basel (Camelbeeck & Meghraoui, 1998). Grabens are limited by Quaternary faults. Squares depict the instrumental seismicity from 1910 to 1990 ($1 < M < 5.5$). Circles correspond to the historical seismicity since 1350 ($M > 5.0$).

To produce accurate scenarios for the repetition of the 1356 earthquake in the heart of modern Europe, it is essential to identify the fault that produced the seismic event and to reconstruct its seismogenic history. The identification of seismogenic faults in intraplate tectonic domains undergoing slow deformation is very often problematic. The deformation rate is low ($\ll 1$ mm/yr.) and does not allow for a clear surface expression of active faults as in interplate active zones. Even if in some intraplate active zones active faults may be visible, the development of urban areas, or the thick vegetation cover and the ongoing erosional process may conceal the main features of active deformation. However, detailed paleoseismic studies combining field geomorphological investigations, high resolution digitized elevation maps, subsurface geophysics and trenching, allow for a more reliable fault analysis. Our investigations rely on two fundamental observations: (1) the occurrence of earthquakes is part of a geological process associated with a seismogenic fault, and (2) individual or cumulative coseismic movements can be registered in the morphology and late Quaternary deposits. For instance, recent paleoseismic investigations in the lower Rhine graben have shown that active normal faults are related with a scarp morphology and that 3 successive coseismic displacements have occurred in the last 45 000 years (3, 4).

In this paper, we present evidence of an active normal fault in the epicentral area of the 1356 Basel earthquake. Using a paleoseismological analysis we reconstruct the timing of historic and pre-historic earthquakes in the Basel area and date a coseismic displacement that can be correlated with the 1356 fault break. We then discuss the inferences for seismic hazard in the Central European area.

The 1356 Basel earthquake

The 1356 Basel earthquake benefits of a relatively rich historical accounts with a detailed spatial description of damage to medieval castles and churches (Figure 2); no other European historical earthquake has been so frequently mentioned in contemporary historical reports.

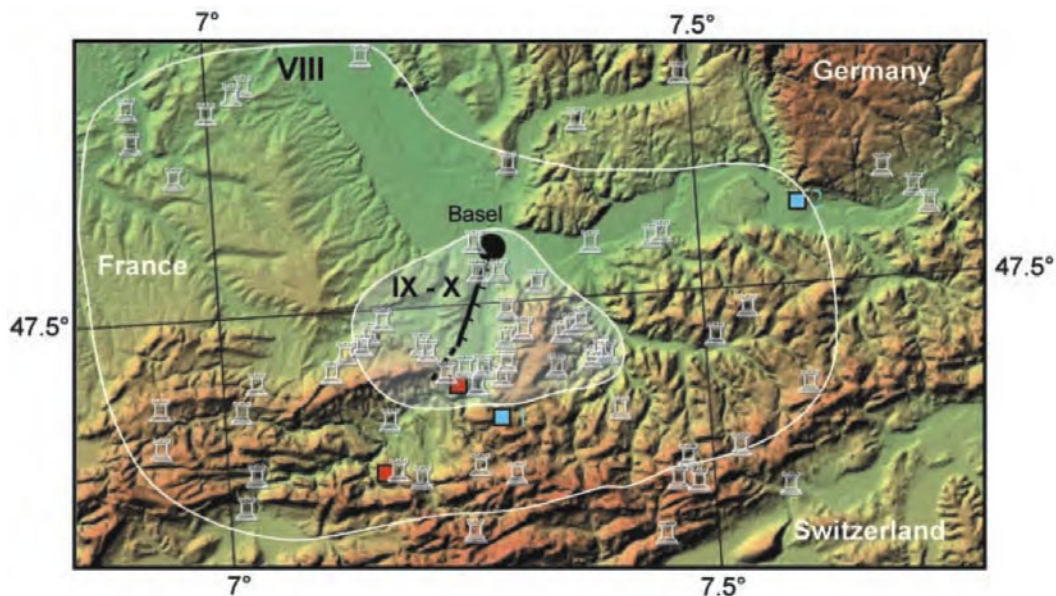


Figure 2. Isoseismals VIII and IX to X of the 1356 Basel earthquake and the location of damaged medieval castles (2, 3). The active fault (solid black line) is in the Birs Valley, south of Basel. Note also the location of caves (red squares) and Berg and Seewen lakes (blue squares) in the area (12). The magnitude of the Basel earthquake and spatial distribution of the damage suggest a shallow focal depth and a fault length of 10 to 15 km; events of this size are generally expected to induce coseismic surface deformation.

The city itself was severely damaged and about 40 castles collapsed in the epicentral area (5). Cadiot and others (6) report the precise account of Konrad von Waltenkof (1360) who describes the continuous aftershock activity during one year after the large event of 18 October 1356. Several contemporary reports (Jean de Roquetaillade, 1360; K. von Waltenkof, 1360; F. Closener, 1362; P. Despotots, 14th-15th century) describe several seismic events on the 18 October with a first strong shock in the evening (“at the diner time”,

7 – 8 pm) and a second stronger shock at 10 pm (“at the bed time”). The latter was considered by all chroniclers as the main shock. From the detailed account of mainly 12 contemporaneous chroniclers (from 1356 to 1421), Mayer-Rosa and Cadiot (1) assigned an MSK intensity IX to X for the main shock and determined an epicentral location in the Birs Valley at about 10 km south of Basel. Indeed, the epicentral zone includes the town of Basel, but the authors observe that damage was more extensive to the south, in the lower Birs Valley and the Jura Mountains of the Blauen, than to the north in the Black Forest (Figure 2). The 1356 Basel earthquake has been assigned magnitudes ranging between 6.3 and 6.5, based on the investigations of the reported historical damage (6). No surface faulting, nor the presence of a causative fault were explicitly mentioned in historical documents. However, a 1362 manuscript related to the biography of the Pope Innocenzo VI reports ground ruptures associated with the 1356 earthquake (6). The Basel earthquake size and related damage distribution (Figure 2) indicate a shallow focal depth and a fault length of 10-15 km; events of this size are generally expected to induce coseismic surface deformation with ground ruptures. The occurrence of multiple shocks during the Basel earthquake may reflect the complex fault pattern between the Jura and the lower Birs Valley.

Geological Setting and Seismotectonic Background

The upper Rhine graben separates the Vosges to the west from the Black Forest to the east and its southern limit corresponds to the Jura Mountains (Figure 1). The complex geological structure of the Basel region is due to the interaction between two main tectonic domains : 1) the Rhine graben and the related Cenozoic rift system, as a part of the intraplate deformation in Europe since the late Eocene; the NNE-SSW trending Quaternary normal faults of the upper Rhine graben underwent changing stress regimes where ENE-WSW main extension prevails, and 2) the Jura fold and thrust belt formed mainly during the late Miocene and Pliocene tectonic episodes, but shows also evidence of Quaternary deformation (7, 8). The recent tectonic regime is associated with transcurrent faults (9) and the role of late Quaternary tectonic episodes is poorly known. The Quaternary faults in the upper Rhine graben show a prominent morphology and a frontal recent scarp, comparable to those observed in the lower Rhine graben (4).

The recent background seismicity of the upper Rhine graben is relatively modest in comparison with that of other continental rifting or interplate tectonic settings. Regional studies with local seismic network show a more pronounced seismicity to the east and south of the graben and a depth of the seismogenic layer of about 15 km within the graben, reaching 20 km depth beneath the Black Forest and Swiss Jura (10, 11). This difference in the thickness of the seismogenic layer may indicate a discontinuity at the top of the lower crust or the brittle-ductile transition zone (12) and could be interpreted as a potential focus of

the large earthquakes nucleation in the area (13). Focal mechanisms calculated for several tens of $ML \leq 5$ earthquakes in the region of the southern upper Rhine graben and northern Alpine foreland show the predominance of strike slip and normal faulting with NE-SW to ENE-WSW direction of extension (14, 15).

The Basel region is characterized by different geological structures and related tectonic background with compressional (Alpine foreland) and extensional structures (Rhine graben) that results in complicated landscape morphology. Therefore the nature of the 1356 earthquake has remained for a long time an open question, since the geological outcrops alone could not provide the necessary observations that characterize the earthquake fault. The east-west trending folds and thrusts of the Jura extend to the North by means of shallow décollement structures (8), and in their morphotectonic study, Meyer et al. (7) discuss the existence of possible seismogenic structures in the area and infer that the Basel earthquake may have reactivated a basement thrust fault beneath the shallow-depth aseismic detachment that underlies the Jura Mountains. Other authors attribute the faulting mechanism associated with the Basel seismic event to reverse faulting, on the basis of the long term deformation that shows tilted and uplifted Quaternary terraces at the edge between the Jura Mountains and the graben (7), or to active normal faulting also imaged by deep reflection seismic line recorded across the graben (1, 12).

Paleoseismic results and surface ruptures of the 1356 earthquake

On the basis of the historical damage indications and of a geomorphological reconnaissance of the area, we focused our paleoseismological investigations on the NNE-SSW trending Basel-Reinach scarp which forms a 8-km-long, linear, sharp morphological feature with 30-50-m-high of topographic relief along the Birs Valley (Figure 3).

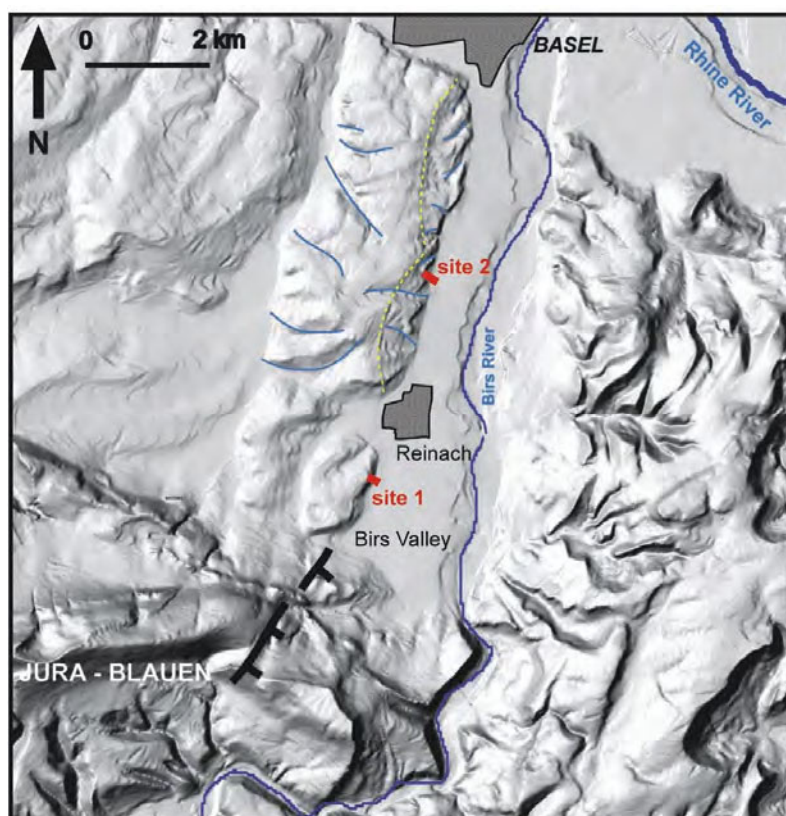


Figure 3. Geomorphology of the Birs Valley and the Basel-Reinach fault scarp from a high resolution topography (MNT25, Office Fédéral de Topographie, DV 1441) and paleoseismic sites 1 and 2. Rivers are shown by blue lines. Note the uplifted Birs River terraces (yellow lines) on the footwall along the northern strand of the fault and the southern fault continuation (black dashed line) across the Jura.

Oligocene sandstones with intercalated clay layers dipping 10° west constitute the pre-Quaternary substratum outcropping along the scarp. The substratum is overlain by a succession of alluvial terraces, and according to the geological map (16) the uppermost terrace is older than the Bruhnes-Matuyama geomagnetic reversal (0.7 Ma). At depth, seismic profiles across the fault scarp show about 100 m vertical offset at 600 m depth which may correspond to the lower Oligocene (Figure 4), (16). At the surface, the linear morphology of the scarp also indicates the active character of the fault and its relationship with the alluvial erosional processes. Younger terraces attributed to the Pleistocene, that likely belong to the old meanders of the Birs river, are exposed in particular along the northern section of the scarp (Figure 3). The examination of aerial photos shows late Pleistocene and Holocene deposits that constitute alluvial terraces and young alluvial fans visible along the scarp toe. Although the fault was not directly visible, we inferred its presence due to the exposed old meanders and step-like morphology along the scarp that suggest its successive uplift during the late Quaternary. Furthermore, the drainage pattern visible along the scarp with short and

deep stream incisions along tributary creeks to the east and long meandering streams to the west illustrates the morphological asymmetry likely due to the successive surface deformation (Figure 3).

Paleoseismological investigations were conducted using geomorphology, electrical resistivity profiles and trenching. The suspected fault-controlled scarp is visible immediately south of the city of Basel, but it is partly hidden by the suburban settlements, agricultural fields and small forests. Although the fault does not appear along the scarp, its approximate location can be defined in between the steep slope of the scarp and the flat fields of the Birs Valley. In order to locate the fault precisely and select appropriate sites for trenching we carried out geophysical prospecting (electrical resistivity, radar, high-definition reflection seismic profiles) across the scarp and the adjacent young alluvial fan.

The fault is visible in several electrical profiles in the form of a sharp resistivity contrast which indicates a minimum of 6 m of vertical separation corresponding to the cumulative offsets produced by the successive displacement events (Figure 4). Several other geophysical profiles (Electrical resistivity, radar imaging and high-reflection seismics) that were performed across the scarp point out the presence of a normal fault system and related successive tectonic episodes.

Trenching operations across the scarp were conducted starting in September 1999. We selected two trench sites at the intersection between the fault and young alluvial fan deposits (Figure 3). Trenches at site 1 were exploratory and were not longer than 10 m due to trees. Trenches at site 2 were subsequently dug to cross a large part of the scarp; trenches T1 and T3 are about 70-m-long, and two subsidiary trenches T2 and T4 with about 10 to 20 m in length were opened to provide lateral constrain on observations of faulted late Quaternary units. We present here only the main results and trench T4 of site 2 (Figures 3, 4 and 5).

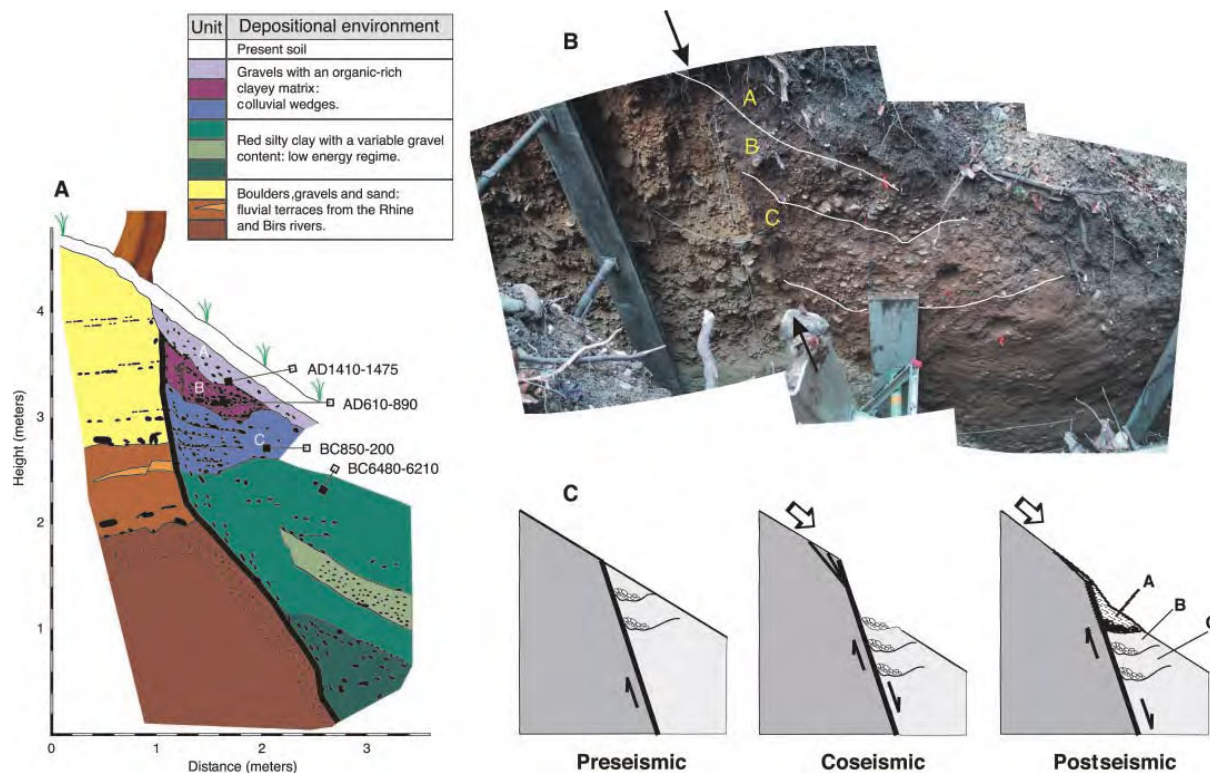


Figure 4. A) Trench T4 north wall illustrating the surface faulting with the three most recent displacements and colluvial wedge deposit A that postdate the 1356 earthquake. B) Photomosaic of colluvial wedges A, B, and C. C) Reconstruction of paleoseismic events: The fault scarp degradation and related colluvial wedge deposit A record the most recent earthquake.

Evidence of normal faulting and surface deformation was found in all trenches, confirming the geophysical observations. At site 2, the main fault which appears as two main branches accompanied by minor antithetic faulting and deformed (warped) units, affects a young alluvial fan adjacent to an incised creek (Figures 4 and 5). The occurrence of a number of late Quaternary faulting episodes is attested by: (1) the 10-cm-thick shear zone with warped footwall units and faulted silty layers on the hanging wall, (2) the alternance of sandy-silty deposits with coarse gravels on the hanging block and successive organic-rich colluvial wedge deposits associated with a superficial fault scarp, (3) a thick superficial sedimentary unit made by fine silty-clay layers forming a small graben-like structure and (4) the successive back-tilting of superficial colluvial coarse gravels and alluvial fine silty units near a main fault branch. Faulted colluvial wedge deposits shows cumulative vertical displacements, with secondary ruptures and progressively tilted gravels and sandy-silt units that illustrate a succession of faulting events.

Trench T4 intercepted a fault which displaces the youngest colluvial wedges (Figure 5A). This fault branch is located at the base of the steep slope of the scarp and allows the preservation of cumulative vertical movements by means of successive fault scarp degradation and related unconformities (Figure 5B). The uppermost unit A below the present soil corresponds to a 0.5-m-thick colluvial wedge deposit made of mixed gravels and silty-clay layers that postdate the most recent fault displacement (see the reconstruction of Figure 5C). C14 dating of a bulk soil sample collected at the base of unit A give 460 ± 25 years B.P. which yield a calibrated 2σ age AD 1410 – 1475 (calibration program OXCAL v3.5, 17, 18). Unit B also consists of 0.5-m-thick colluvial wedge deposits with admixed coarse gravels and silty-clay at the base of which C14 dating of a bulk soil sample gives 1310 ± 70 years B.P. (2σ age AD 610–890). Unit C is 0.8-m-thick colluvial deposits comparable to units A and B but with nearly flat lying stratified units of coarse and fine gravels, abruptly cut by the fault. The C14 dating of a bulk soil sample yields 2430 ± 120 years B.P. (2σ age BC 850–200). A succession of massive colluvial silt layers with scattered gravels are below unit C and the C14 dating of a bulk soil sample yields an age of 7510 ± 80 years B.P. (2σ age BC 6480–6210). The succession of faulted colluvial wedges B and C overlain by unit A evidence three coseismic events with at least 1.8 m cumulative vertical displacements (that correspond to the thickness of the three colluvial wedges A, B and C of Figure 5B) during the last 8500 years (Table 1). The most recent faulting event is bracketed between AD 610 and 1475. As it probably occurred shortly before the deposition of unit A (soon before AD 1410-1475) it may corresponds to the AD 1356 Basel earthquake.

Discussion and conclusions

A major seismic source in the Basel area

The active Basel-Reinach normal fault displays along the western scarp of the Birs Valley successive displacements during the late Pleistocene and Holocene. The pattern of surface deformation with the normal fault system observed in geophysical profiles and trenches is extensive and can be compared to surface ruptures observed during large earthquakes such as Corynth (Mw 6.7, Greece; 19) or Borah-Peak (Ms=7.3, Basin and Ranges; 20).

The 8-km-long fault scarp that limits to the west the Birs Valley can be considered as a minimum length. Indeed, the fault may extend to the north across the city but also to the south, where the east-west trending Jura folds (2.5 km SSW of Reinach) are faulted and highly fractured at their intersection with the fault scarp extension. The total vertical displacement $U_t = 50\text{-}100$ m across the fault scarp, indicated by the uniform 30 to 50m high scarp morphology, the 30 m thick late Quaternary deposits and by the cumulative separation at 600 m depth (Figure 4) (16) suggests a longer fault length. On the basis of the Kanamori

and Anderson dislocation theory (21) the 0.5 to 0.8 m of coseismic vertical displacements visible in trench T4 imply a rupture length of 15 to 20 km. If we consider 0.5 m as an average coseismic displacement along the Basel-Reinach fault, the empirical relations derived from Wells and Coppersmith (22) yield a surface rupture length between 10 and 20 km long and a 6.4 to 6.5 magnitude. A longer fault (≥ 15 km) would also be more consistent with the 15 km depth of the seismogenic layer (11) and the average 0.5 m of vertical displacement per event obtained from the trenches. These fault dimensions would yield an estimated seismic moment $M_0 = 3-5 \cdot 10^{25}$ dyne cm ($M_w = 6.4$) for the 1356 Basel earthquake, in good agreement with the historical estimates.

Seismic history of the Basel area

In addition to the 1356 earthquake, the trench datations identify two additional event time windows (Table 1) bracketed between BC 6480–850 and BC850–AD890, indicating the occurrence of a 1356-type event every 1500-2500 years.

These results are in good agreement with the analysis of growth anomalies of speleothems and block collapses in 2 caves located immediately south of the Birs Valley (Figure 3), which indicate the occurrence of 3 disturbances dated at BC3630–3370, BC160–AD80, and AD1165–1400 (23). If these disturbances can be attributed to past earthquakes they correlate quite well with events observed in trench T4. In addition, extensive investigation of lake sediment deposits in the Berg and Seewen Lakes near Basel have indicate the occurrence of 3-5 seismic events during the last 11000 years BC (the last 2000 years cannot be investigated with these techniques), and identified the possible event time windows 180-1160 BC, 2900-3850 BC, 4870-5660 BC, 8260-0940 BC and 10720-11200 BC (24).

A consistent pattern emerges from these different investigations and points to a recurrence time of 1356-type earthquakes in the Basel area of about 2500 years. In addition, the consistent datings of trench T4 indicate that the Basel-Reinach fault is the primary seismogenic active fault in the upper Rhine graben during the Holocene.

Active tectonics in intraplate Europe and related seismic hazard implications

The occurrence of three large earthquakes in the last 5000-7500 years with a total amount of 1.8 m of vertical displacement on the Basel-Reinach fault leads to 0.24 mm/yr of uplift rate. The uplift rate obtained from the paleoseismic investigations is comparable to the 0.18 mm/yr derived from the vertical offset of the uppermost alluvial terrace visible on the footwall block, covering the Oligocene units and appearing in boreholes at 30 m depth in the Birs Valley (16). Geodetic measurements across the upper Rhine graben also show a maximum extension rate of 1-2 mm/yr for the past 20 years (25). Taking into account the

historical and instrumental seismicity catalogue, Ahorner (26) calculates 0.32 mm/yr seismic slip rate. Hence, the 0.18 to 0.24 mm/yr uplift rate along the Basel-Reinach fault likely accommodates a major part of the seismic deformation of the graben.

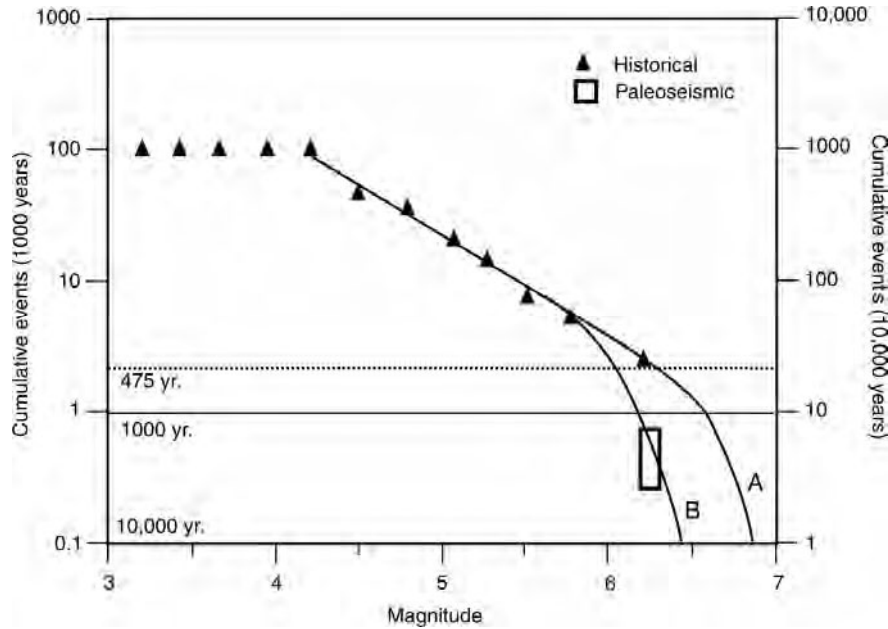


Figure 5. Cumulative logarithmic frequency-magnitude distribution of the seismicity of the last 1000 years in the greater Basel region, from the Marcoseismic Earthquake Catalogue of Switzerland. The activity rates constrained by historical and paleoseismological records are similar at low magnitudes but very different at higher magnitudes. The difference is also modest for the 475-year return period commonly assumed in hazard mapping but becomes dominant for longer return periods and low occurrence probabilities.

To see how significant the earthquake datings from the Rheinach fault are for the assessment of local seismic hazard, we constructed the frequency-magnitude distribution of the seismicity during the last 1000 years in the greater Basel region (Figure 5). The logarithmic distribution exhibits the expected linear decay in the magnitude range $M = 4.5$ - 6.3 , with two seismic events with a magnitude exceeding 6, 1021 and 1356. However, the existence of the 1021 seismic event has been seriously questioned from a recent examination of historical documents (27). In the hypothesis of stationary seismicity commonly assumed in seismic hazard assessment, the 1000 yr activity rate can be extrapolated for a 10,000 yr period by scaling the curve by one logarithmic unit, obtaining 20 1356-type earthquakes over a 10,000 yr period (curve A). The paleoseismological results allow to restrict the range of possible scenarios for the Basel area (28); combining trenching results along the Basel-Rheinach fault with those of lake deposit investigations, we obtain 5-8 1356-

type earthquakes for the last 10.000 yr (depending on selection criteria) and we obtain a more conservative distribution for the occurrence rate for earthquake in the Basel region (Curve B, Figure 5).

The activity rate curves constrained by the historical and paleoseismological records (A, B) are similar at low magnitudes, but very different at higher magnitudes; the difference is also modest for the 475 yr return period commonly assumed in hazard mapping, but becomes dominant for longer return periods and low occurrence probabilities. The prospect for future large earthquakes along the Basel-Reinach fault needs further development of the paleoseismological investigations that will help in : 1) a better estimate of the total fault length and related maximum expected magnitude, and 2) assessing a complete list of paleoearthquakes, their related individual displacements and recurrence interval during the late Pleistocene and Holocene.

The damage pattern produced by an earthquake depends on the complex interaction between the seismic source, the local geological conditions and the building vulnerability. The future re-evaluation of the seismic risk in the upper Rhine graben will be based on a more robust estimate of the recurrence period of large earthquakes and on a more precise definition of the faulting and shaking scenario in the Rhine sedimentary valley.

Acknowledgments

We thank M. Cara, D. Mayer-Rosa, P. Ziegler, J. Vogt, K. Bonjer, A. Crone, R. Arrowsmith, B. Meyer, E. Jacques, T. Winter, G. Sagripanti and D. Faeh for the fruitful discussions during the field and trenches investigations. We thank P. Grootes (Kiel University) for the detailed reports and comments on C14 dating. The 2-year research and investigations were funded by the INSU-PNRN (project 99PNRN 20 AS), the BRGM (contract Geofr3D 99/17), the European Commission SAFE project (DG XII - EVG1-2000-22005), and the Swiss PALEOSEIS program (SNF and HSK).

Chapter 3

Evidence for Holocene Paleoseismicity along the Basel-Reinach Active Normal Fault (Switzerland): A Seismic Source for the 1356 Earthquake in the Upper Rhine Graben

*Ferry, M., Meghraoui, M., Delouis, B. and Giardini, D.
(in press, *Geophysical Journal International*)*

3.1. Summary

We conducted a paleoseismic study with geomorphologic mapping, geophysical prospecting and trenching along an 8-km-long NNE-SSW trending fault scarp south of Basel. The city as well as 40 castles within a 20-km radius were destroyed or heavily damaged by the earthquake of 18th October 1356 (Io = IX-X), the largest historical seismic event in central Europe. Active river incisions as well as late Quaternary alluvial terraces are uplifted along the linear Basel-Reinach fault scarp. The active normal fault is comprised of at least two main branches reaching the surface as evident by resistivity profiles, reflection seismic data, and direct observations in six trenches. In trenches, the normal fault rupture affects three colluvial wedge deposits up to the base of the modern soil. Radiocarbon as well as thermoluminescence age determinations from other trenches helped to reconstruct the Holocene event chronology. We identified three seismic events with an average coseismic movement of 0.5 - 0.8 m and a total vertical displacement of 1.8m in the last 7800 years and five events in the last 13200 years. The most recent event occurred in the interval 610 - 1475 A.D. (2σ) and likely corresponds to the 1356 earthquake. Furthermore, the morphology suggests both a southern and northern fault extensions that may reach 20 km across the Jura Mountains and across the Rhine Valley. Taking this fault length and a 10 km-thick seismogenic layer suggests a Mw 6.5 or greater event as a possible scenario for the seismic hazard assessment of the Basel region.

Keywords: paleoseismicity, active tectonics, Upper Rhine graben, Basel.

3.2. Introduction

The tectonic signature of coseismic surface faulting in an active fault zone is developed and preserved as a function of rate of deformation and surface geologic processes. Successive coseismic surface rupture displacements along a fault can be studied using paleoseismic investigations to determine a rate of the active deformation and a recurrence interval for large earthquakes. The paleoseismic record of large or moderate earthquakes in regions with a present-day low level of seismicity has been documented to show fault slip rates much lower than 1 mm/yr and likely on the order of 0.1 mm/yr (Crone et al., 1997; Camelbeeck and Meghraoui, 1998).

However, the identification and characterization of a seismogenic fault in these regions are a major problem due to two main factors: (1) the rate of active deformation being quite low, surface faulting and related cumulative scarp are hardly visible unless a detailed study in active tectonics is undertaken, (2) the surface deformation is very often hidden by

either a thick vegetation cover (e.g., forests), by agricultural fields or by an urban area as it is the case along the Basel-Reinach (BR) fault. Therefore, paleoseismic investigations across low slip rate active faults require the use of a multidisciplinary approach including geomorphology, geophysical prospecting and trenching. This approach was successfully tested along the Feldbiss fault (at Bree) in the Lower Rhine graben and the paleoseismic results revealed the occurrence of three events with $M_w > 6.2$ in the last 30 000 years (Meghraoui et al., 2000; Vanneste et al., 2001).

Intraplate Europe is classified among the stable continental regions because of the low rate of deformation (Fig.1) (Johnston, 1996; Camelbeeck and Meghraoui, 1998). However, the historical seismicity is noteworthy and moderate to large damaging earthquakes have occurred in the past (Camelbeeck et al., 2000). In this context, the occurrence of the 18th October 1356 shallow earthquake in Basel is among the largest historical seismic event with maximum $M_w = 6.5$ in Western Europe (Mayer-Rosa and Cadiot, 1979). This large seismic event posed the problem of the identification of the seismic source in the area of Basel (Meyer et al., 1994). In a previous study of the active deformation of the southern Upper Rhine graben we have identified the BR active fault and shown its probable relationship with the 1356 earthquake (Meghraoui et al., 2001). The first results obtained from trench studies have shown the occurrence of three large seismic events with $M_w > 6$ in the last 7800 years and a total vertical displacement of 1.8 m.

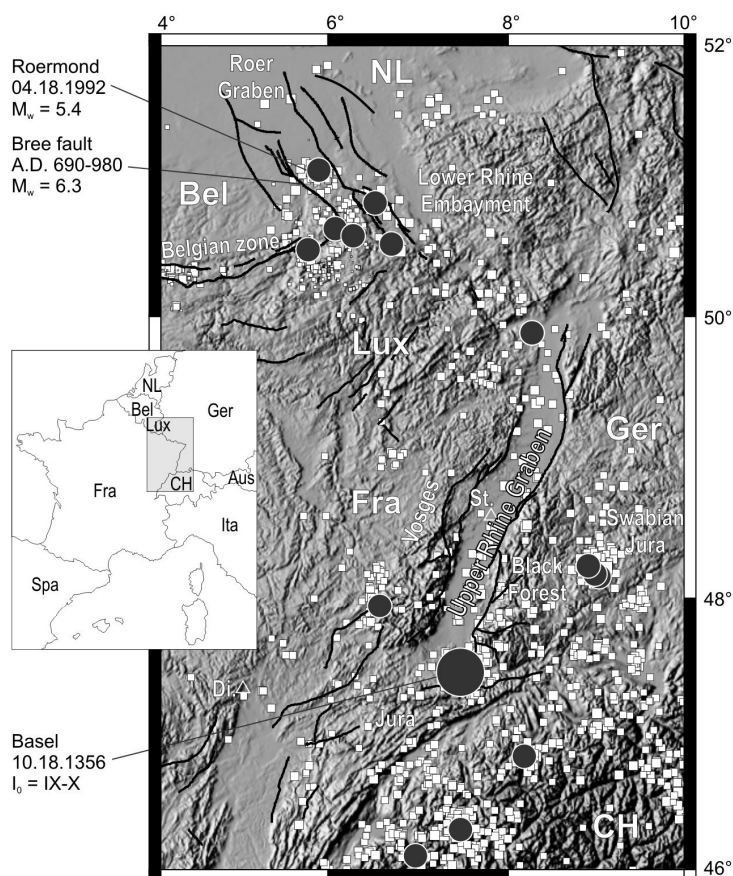


Figure 3.1. Seismicity and tectonics of NW Europe. Seismicity (historical in grey circles and instrumental in white squares) and Quaternary faults (black lines) of the Rhine graben underline the recent tectonic activity of intraplate Europe. Our study area is located in the vicinity of the 18 October 1356 Basel earthquake, one of the strongest seismic events in Europe ($I_0 = IX-X$; Mayer-Rosa and Cadiot, 1979). White triangles point to Dijon (D) and Strasbourg (St) cities located more than 100 km away and which recorded strong damage to bell towers.

In this paper we provide a summary of the 1356 earthquake followed by a detailed description of the BR fault using the relationship between the fault scarp geomorphology (surface deformation and drainage pattern) and related distribution of late Quaternary deposits (colluvial, fluvial and alluvial terraces). Historical accounts of the 1356 seismic event are presented together with the seismotectonic and neotectonic frameworks. The surface faulting and related paleoseismology is documented using (1) electrical resistivity profiles combined with high resolution seismic lines and (2) 8 trenches dug across the fault at two different sites. An analysis of the long term deformation using accelerated mass-spectrometer (AMS) radiocarbon and thermoluminescence (TL) dating shows the succession of past seismic events illustrated with reconstructions and kinematical models of the surface faulting. Amounts of coseismic displacements, maximum size of the fault and recurrence interval of large earthquakes are discussed for an evaluation of the seismic hazard in the southern upper Rhine graben.

3.3. The 1356 Basel Earthquake

On the 18th October 1356, the city of Basel was struck by a first seismic shock “by dinner time” then by a stronger shock “by bed time” (Vogt, 1979). According to several historical sources, strong aftershocks occurred monthly for more than a year. Contemporaneous damage descriptions following the earthquake were thoroughly reviewed by Montandon (1943), Vogt (1979), Mayer-Rosa and Cadiot (1979), Lambert (1997) and Fäh et al. (2003). The city itself endured very severe damage with almost all of its churches and towers destroyed as well as part of the city moat and not more than a hundred houses resisted collapsing (Vogt, 1979). Earthquake victims may have reached 2000 lives from the 6000 inhabitants. This estimate can be, however, exaggerated as the region endured a “black decade” that included a millennial flood in 1343, the Black Plague in 1348-49 and the Basel earthquake in 1356. Historical sources report that 40 castles were destroyed or heavily damaged within a 20-km radius of the city and damage to bell towers was recorded as far as 110 km in Strasbourg and Dijon. Mayer-Rosa and Cadiot (1979) assigned an intensity of IX-X

on the MSK scale and an estimated magnitude of 6.0 - 6.5. Taking into account all historical observations and in the frame of the recently re-evaluated historical catalogue of the Swiss Seismological Service (Fäh et al., 2003), we propose a new intensity map (Fig. 2). Soon after the earthquake, Pope Innocent VI sent a delegate who accurately described damage to the city and its surroundings. He reported that “...the earth opened in several places and white boiling sulphurous water flowed out abundantly.” (Vogt, 1979) indicating the possible occurrence of surface ruptures and/or liquefaction features. In addition to the 1356 event, the region has seen 9 other events with estimated magnitudes larger than 5 during the last millennium (Fäh et al., 2003).

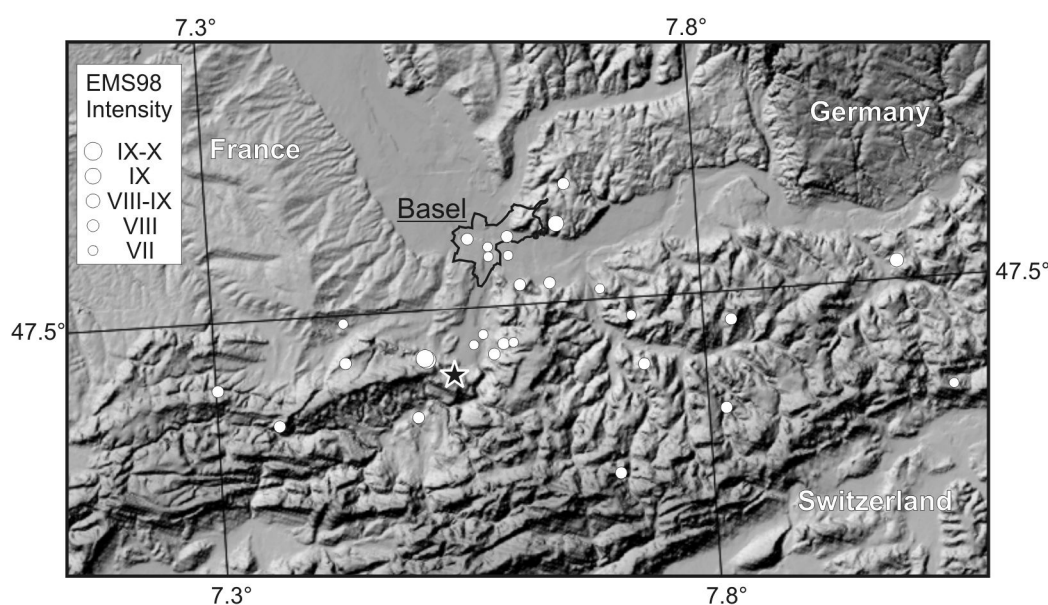


Figure 3.2. Intensity map for the 18th October 1356 Basel earthquake with data from the Swiss Seismological Service re-evaluated historical seismicity catalogue (Fäh et al., 2003). White dots indicate damage distribution. The inferred epicenter (black star) is located at the southern end of the Birs Valley, 8 kilometers south of Basel.

3.4. Neotectonic and Seismotectonic Framework

The Upper Rhine graben is part of a continental rift affecting intraplate Europe during late Cenozoic time. According to seismic profiles and borehole data, it is filled with more than 3.300 m of Tertiary and Quaternary sediments (Doebli and Olbrecht, 1974). The southern region of the Upper Rhine graben (Fig. 3) is limited to the east by the Tabular Jura and to the south by the folded Jura. Early extensional movements took place during the late Eocene and the late Oligocene, and according to Laubscher (2001), the Tabular Jura is related to the

extensional movements of the graben. In fact, along with a well-developed bounding fault system, the large-scale N-S trending Rhine Valley flexure formed and a normal fault system propagated eastwards over more than 20 km, as far as Zeiningen (Fig. 3). This region is interpreted as the faulted upper Muschelkalk limestone forming individualized blocks tilted to the East and that slipped westwards on an underlying evaporite layer. The faulting episode presumably stopped during the late Oligocene and became a major west-dipping normal fault zone affecting the eastern rim of the tabular Jura. No mention exists in the literature on the Neogene and Quaternary tectonic episodes of this region.

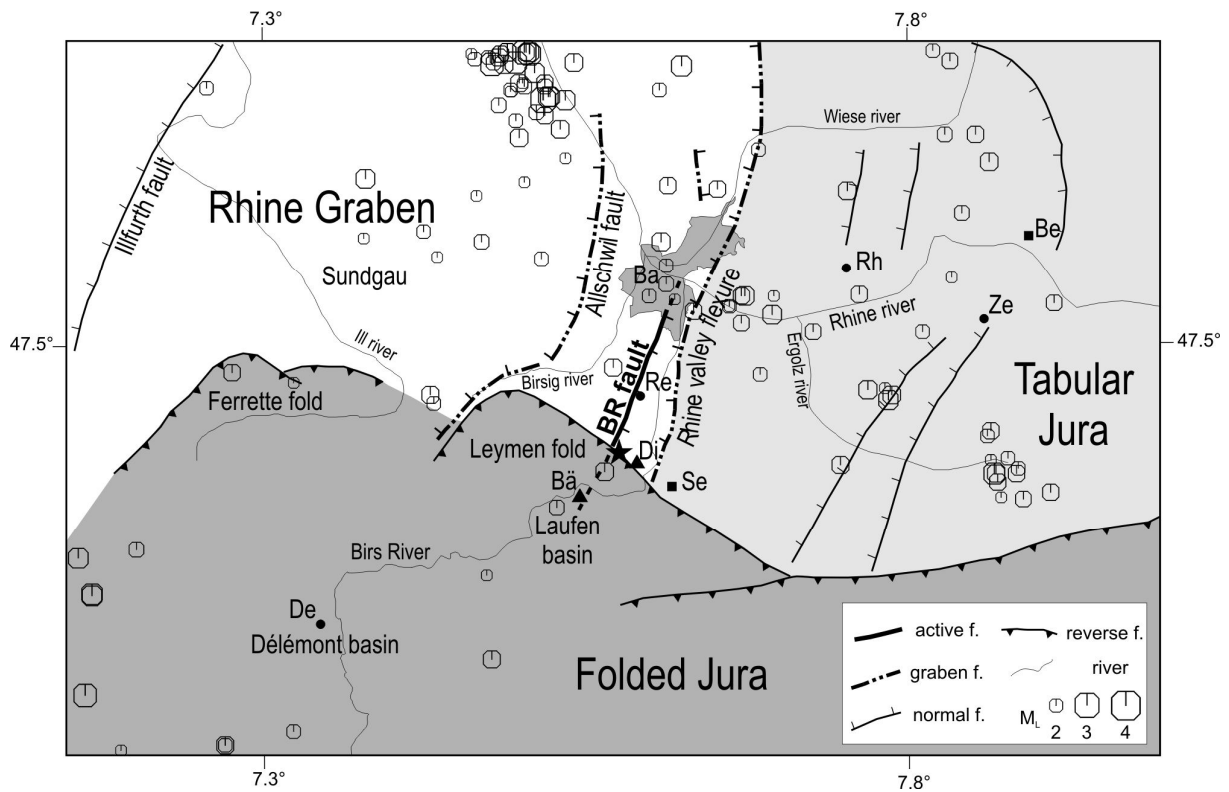


Figure 3.3. Seismotectonic framework of the southern upper Rhine graben. BR: Basel-Reinach fault, Ba: Basel, De: Délémont, Re: Reinach, Rh: Rheinfelden, Ze: Zeiningen. Seismicity recorded over 1975-2000, $2 < M_L < 4$. Black star refers to the location of the 1356 epicenter as estimated by the Swiss Seismological Service (Fäh et al., 2003). Triangles refer to caves investigated by Lemeille et al. (1999), Di: Dieboldslöchli, Bä: Bättlerloch. Squares refer to lakes investigated by Becker et al. (2002), Se: Seewen, Be: Bergsee.

To the South, the Folded Jura forms an E-W arcuate folding system and constitutes the foreland tectonic structures of the western Alps. It is generally associated with the Alpine compression and is often interpreted as the most active structure in the region. Recent stress measurements (Becker, 2000) and geodetic measurements (conventional and GPS, Nocquet

et al., 2001) document Quaternary as well as present-day N-S to NW-SE compression and E-W to NE-SW extension of the main active deformation between the Jura and the Rhine graben. From geomorphic data and seismic profiles Nivière and Winter (2000) provide evidence for Quaternary faulting from a shallow (2 – 3 km depth) compressional décollement extending north in the Sundgau, but due to its geometry and depth it is not considered a seismogenic structure. Authors infer that the northern rim of the Folded Jura exhibits several chevrons which would accommodate for most of the Quaternary compression. Although no evidence is shown for late Pleistocene and Holocene faulting, an inferred WSW-ENE basement fault has been considered as the most probable source for the Basel earthquake (Meyer et al., 1994).

The present day stress tensor as inverted from focal mechanisms by Plenefisch and Bonjer (1997) corresponds to a predominantly strike-slip regime with σ_1 striking N162 and σ_3 striking N69, both of them being horizontal to subhorizontal. However, the presence of two secondary minima suggests that σ_1 may be oriented vertically or at 45°. Furthermore, as magnitudes between 2 and 4 only were available, implications in terms of crustal deformation should be cautious and extension may be considered likewise.

3.5. Fault Scarp Geomorphology

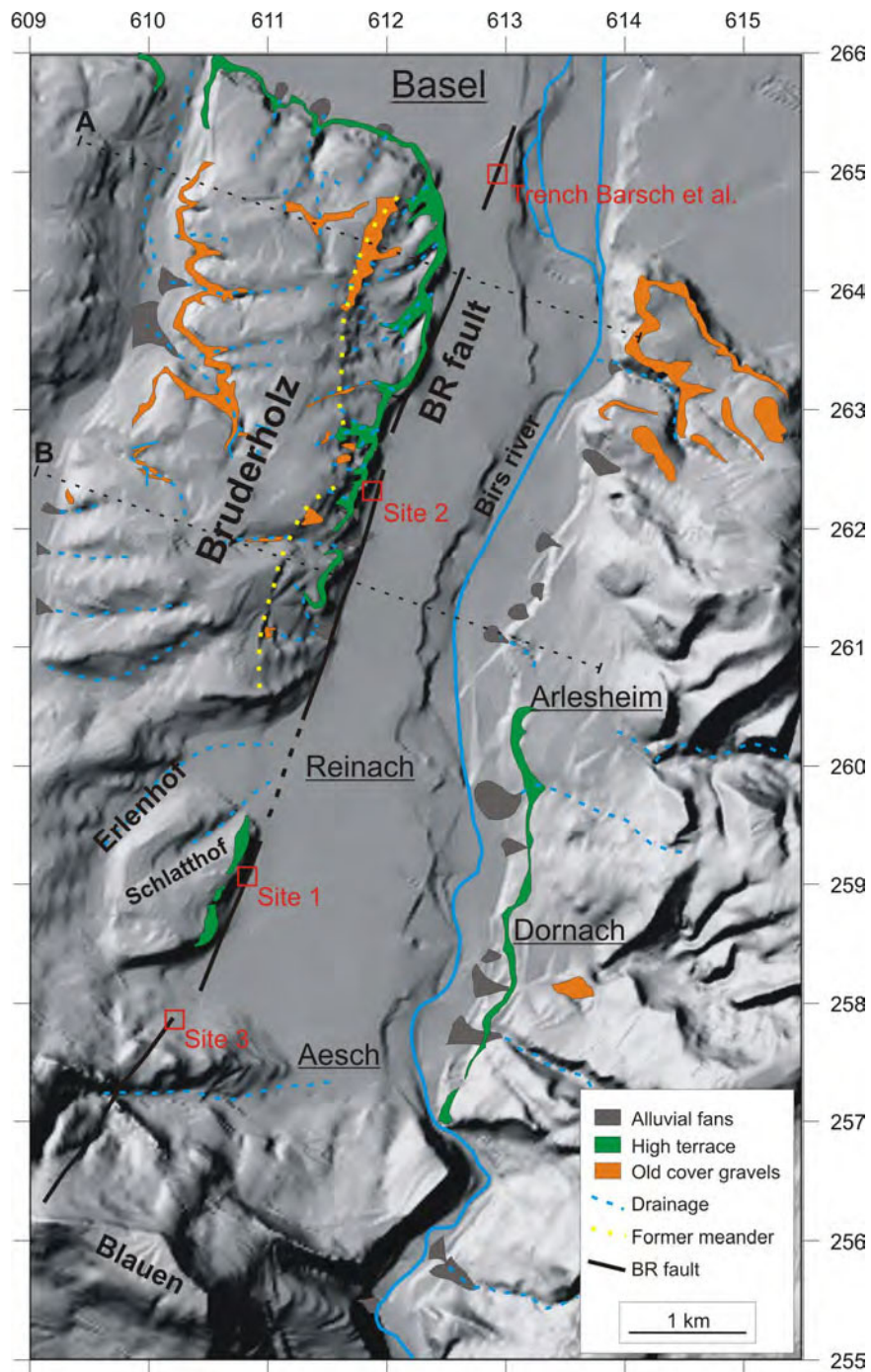


Figure 3.4. Geomorphology of the Basel-Reinach fault scarp. Shaded relief of the Birsi valley from digital elevation data (DHM25 dataset by Landestopographie, DV1441) shows the location of the Basel-Reinach fault (thick black line). Quaternary alluvial terraces (old cover gravels as orange patches and high terrace as green patches) and abandoned meanders (yellow dashed arcuate lines) of the Birsi River are uplifted with respect to the present-day flood valley. Short straight lines on the eastern side of the valley are due to kriging artifacts and old river channels. Black dashed lines labeled A and B refer to the extracted topographic profiles shown in Fig. 5. Coordinates are in kilometers in the Swiss CH1903 reference system.

The Rhine graben exhibits a N10-N20 direction and is in the south bordered by the Vosges massif to the west and the Black Forest massif to the east. South of the city of Basel, the recently identified BR fault forms the bounding structure of the Birs Valley to the east with the Bruderholz heights to the west and exhibits evidence for a late Pleistocene and Holocene tectonic activity (Meghraoui et al., 2001). Its orientation (N15) is consistent with the general direction of the graben (Fig.1). West of the Birs Valley, the Birsig river flows eastward to the western flank of the Bruderholz block then is sharply diverted to the North (Fig. 3.3). As a response to a marked topographic asymmetry drainage patterns on the eastern flank of the Bruderholz block display long meandering streams with short straight streams on its western flank (Fig. 4 and 5-a). The northern section of the BR scarp shows a series of streams that have incised ~25 m through Quaternary river terraces and have steep (>40°) slopes. This geomorphology suggests intense erosion processes which may be related to recent uplift or subsidence movements along the scarp. At the same location, two former meanders of the Birs River (see yellow dashed arcuate lines on Fig. 3.4) are now perched at 30-40 m relative to the present-day flood valley. More to the south, and west of Reinach, the Erlenhof Valley could be a similar younger feature. All along the BR fault scarp, Quaternary alluvial terraces attributed to the Rhine and Birs Rivers crop out as elongated strips at various elevations above the Birs level. An examination of Quaternary terraces on both sides of the Birs Valley shows that the top surface of the Q3s terrace (high terrace on Fig. 3.4) which is attributed to the ~240 ka Riss age (Bitterli-Brunner and Fischer, 1988) crops out at a higher elevation on the western flank of the valley (Fig. 3.4 and 3.5-b). Outcrops of Q3s follow a gentle gradient of ~0.5° to the NNE on both edges of the Birs Valley. However, their altitude is consistently higher by ~35 m on the western side than on the eastern side. This indicates a minimum uplift of 30-40 m along the Bruderholz scarp with respect to the rim of the Tabular Jura after the deposition episode of unit Q3s. Assuming a maximum age of 240 000 years for Q3s and not taking erosion into account, we obtain 0.12 – 0.16 mm/yr as a minimum long-term vertical displacement rate.

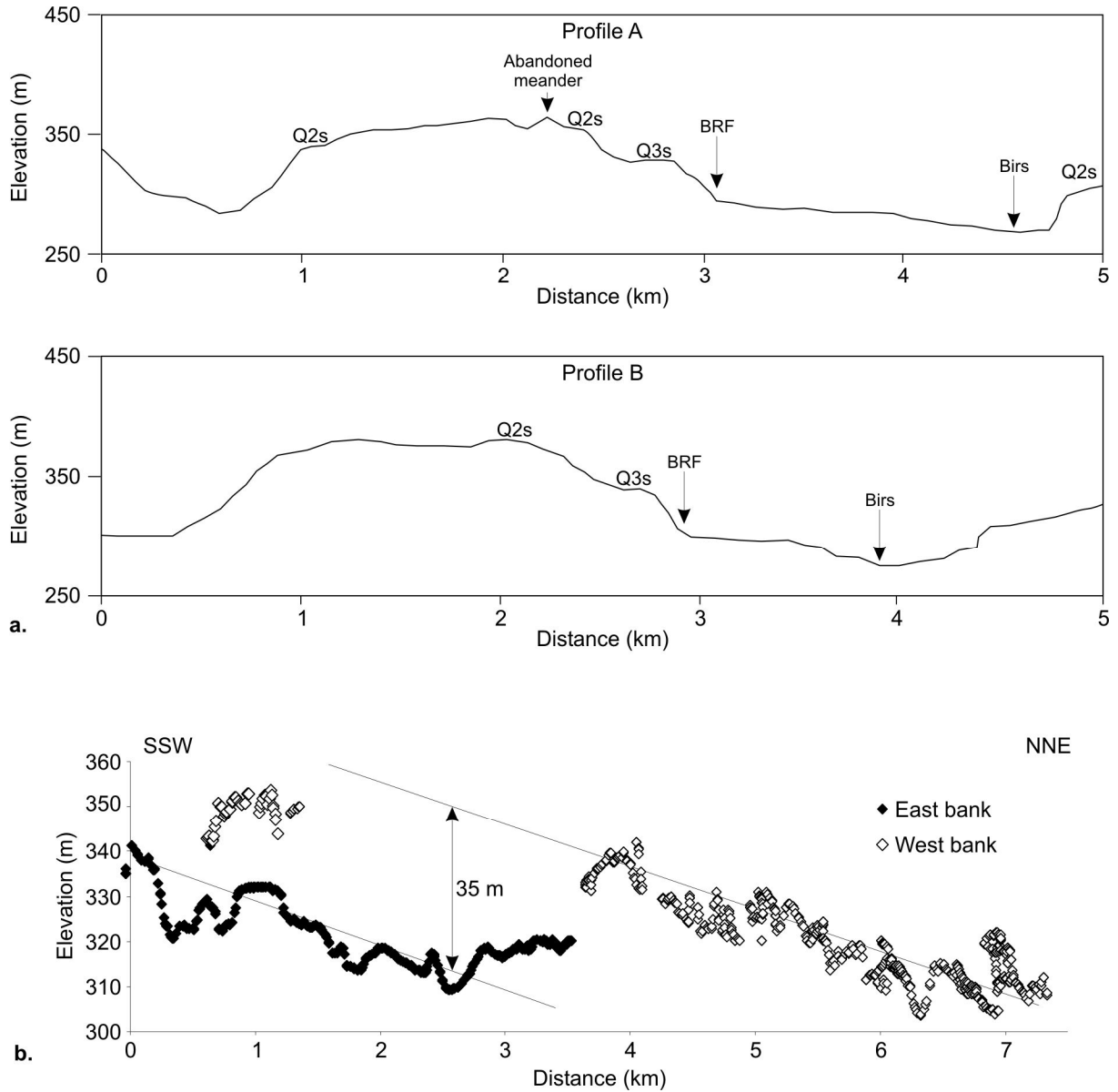


Figure 3.5. a) Across-strike topographic profiles extracted from the DHM25 elevation dataset show the asymmetry of the Bruderholz scarp and the location of the Basel-Reinach fault (BRF) and the Birs River. Topographic flats mark the location of Quaternary terraces Q2s and Q3s. Note the westward dip of Q2s and the difference in elevation between both sides of the valley for Q2s and the apparent absence of Q3s on the eastern side.

b) Distribution of the high terrace (unit Q3s) along the Birs River. White dots from the Bruderholz scarp (uplifted block) and black dots from the Rhine Valley flexure (downthrown block) show a consistent vertical displacement of 30-40 m.

At depth the BR fault intersects an east dipping normal fault as displayed on commercial seismic profiles (Bitterli-Brunner and Fischer, 1988). Figure 3.6-b shows the profile BL24 in the vicinity of Basel, for which we had access to full-length original

hardcopies. At a depth of about 600 m a sharp horizontal reflector (attributed by the authors to the base of the Tertiary) shows 100 m of vertical displacement along a system of high-angle normal faults. The upward prolongation of the main branch intersects the surface at the eastern edge of the BR fault scarp.

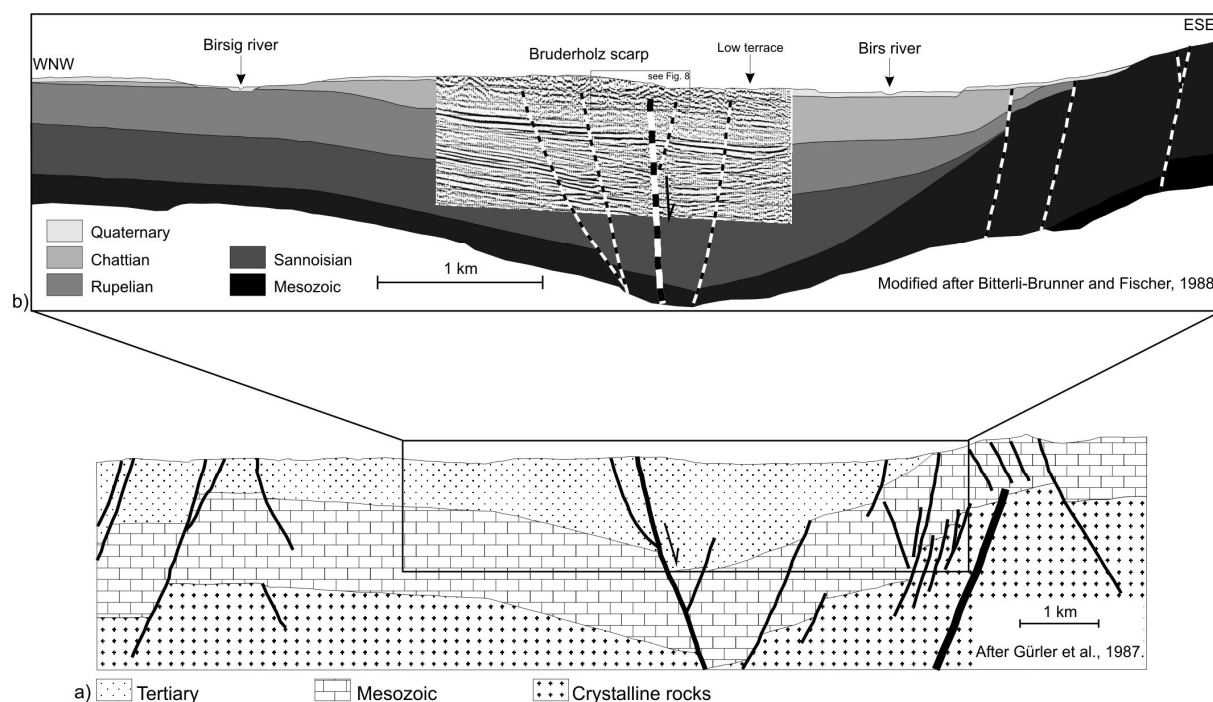


Figure 3.6. a) General tectonic interpretation of the south-eastern Upper Rhine Graben by Gürlér et al. (1987).

b) Public excerpt of commercial seismic line BL24 from 1978 within a general geological interpretation by Bitterli-Brunner and Fischer (1988). Note the near-vertical dip of the main fault at the eastern rim of the Bruderholz scarp. At a depth of ~600 m, the base of the Chattian unit exhibits a clear seismic reflector. It is cut and vertically displaced by ~100 m. Interpreted faults are stopped before reaching the surface due to improper resolution of seismics within the last 200 m. Vertical and horizontal scales are identical. Note that full-length profile and its exact location are not public data at the moment.

3.6. Geophysical Investigations

To investigate the near-surface geometry of the fault and show its continuity from depth to surface, we selected three sites (Fig. 3.4) and conducted geophysical surveys with various resolutions and penetration depths. They proved to be efficient in locating faults and related features within the shallow sub-surface at places where the geomorphologic signature is weak and/or concealed (Camelbeeck and Meghraoui, 1998; Meghraoui et al., 2001).

Hence, a 600-m-long high-resolution seismic line was acquired across the scarp at site 2 (Fig. 3.7). Using a weight dropper and dynamite, we achieved a penetration larger than 200 m with an estimated vertical resolution of 20 m. At the western end of the profile, which is the top of the scarp, a continuous high-energy reflector dips gently to the west ($\sim 15^\circ$). According to borehole data (Bitterli-Brunner and Fischer, 1988), this reflector marks the base of Quaternary gravel deposits (Jüngerer Deckenschotter). It is vertically displaced by 80 ± 20 m along a system of normal faults which form a graben. At the toe of the scarp, the Quaternary units are faulted and show ~ 15 m vertical displacement. This is consistent with field observations and borehole data (Bitterli-Brunner and Fischer, 1988). Hence, the base of the Quaternary units (Jüngerer Deckenschotter) shows a minimum 100 ± 20 m of vertical displacement from its topmost position on the scarp to the bottom of the valley. The base of the Quaternary north of the Bruderholz scarp exhibits a negative magnetic field that indicates an age older than the Bruhnes-Matuyama magnetic reversal (730'000 years, Zollinger, 1991). This yields 0.11 - 0.16 mm/yr for the long-term maximum vertical displacement rate in agreement with the 0.14 mm/yr obtained from the uplifted Q3s terrace. Furthermore, this suggests that seismic activity along the BR fault is probably not older than the Riss ice age ($\sim 250'000$ years).

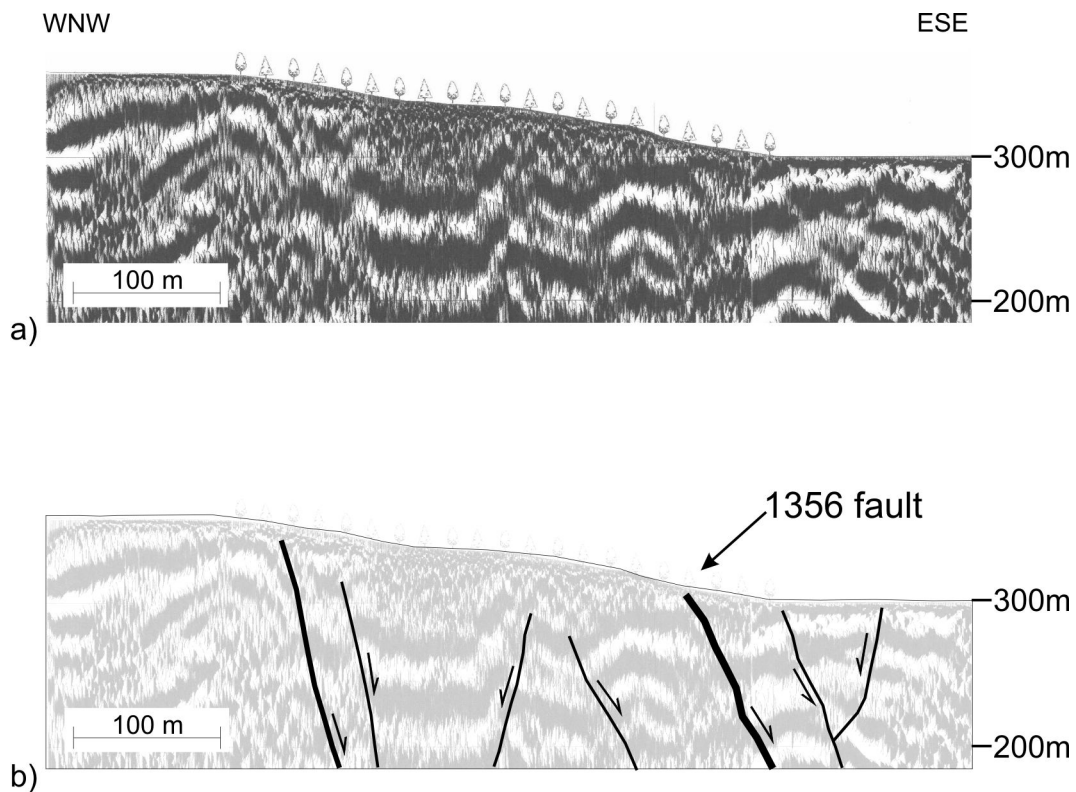


Figure 3.7. High-resolution seismic line surveyed across the Basel-Reinach fault at site 2, on the eastern flank of the Bruderholz block and the corresponding interpreted faults. This line follows a

portion of the exact path of line BL24 (see Fig. 6) and resolves the uppermost 100 m of the fault system beneath the Bruderholz scarp. Again, note that faults are near-vertical.

To improve details in the sub-surface, we also conducted multi-electrode resistivity tomographic surveys (Suzuki et al., 2000). Two main electric units were repeatedly imaged (Fig. 3.8) : a resistant material (100-400 Ω .m) probably composed with carbonates and always located near the surface and a conductive unit (5-40 Ω .m), probably clayey and silty, systematically located below or against the resistive unit. As measured resistivity values were very low, especially close to the surface, we could not use the ground-penetrating radar (measured resistivity should be larger than 50 Ω .m for 100 MHz antennae, see Meschede et al., 1997). We retained three alternative criteria for fault identification i) a distinctly vertically displaced resistivity unit, ii) a sharp sub-vertical contrast separating two different units (lithological contact) or iii) a sub-vertical “intrusion” of low-resistivity material associated with water circulation and possible secondary clay minerals deposition along a fault plane (Fujimoto et al., 2000).

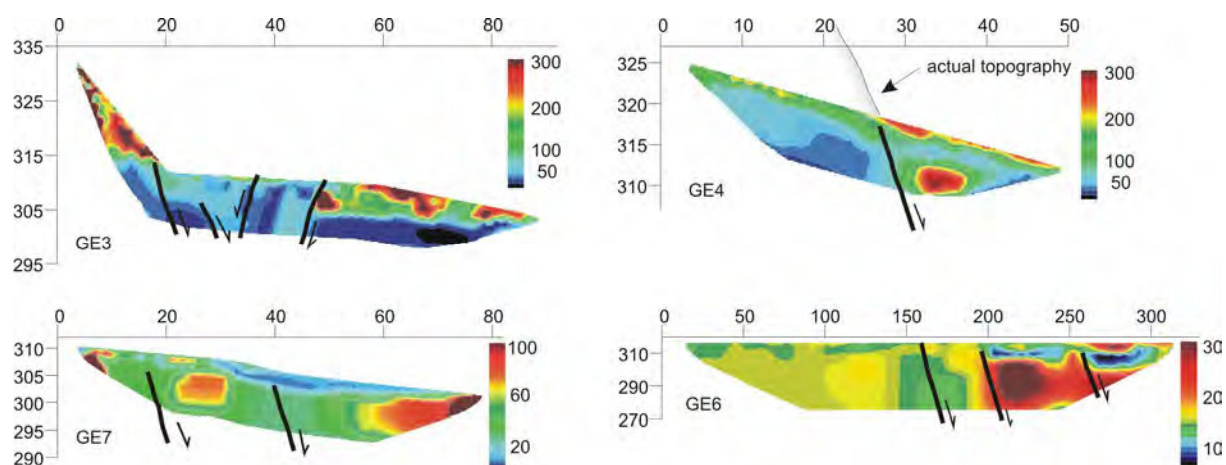


Figure 3.8. Electrical tomography data collected from west to east across the Basel-Reinach fault from north (top profile GE4) to south (bottom profile GE6). Modeled resistivity sections (left) are displayed with individually optimized color scales. X-coordinate is distance in meters from origin, y-coordinate is elevation in meters above sea-level. Resistivity is given in Ω .m. Black lines indicate inferred faults which separate faulted and vertically displaced blocks.

At site 1, profile GE7 (Fig. 3.8) displays faulted blocks which are vertically displaced by about 9 m on two different fault strands to form a step-like morphology. They are overlain with a continuous conductive unit, probably composed with re-deposited clayey loess washed off from the uppermost terrace surfaces.

At site 2, profile GE3 shows a graben-like structure which buries conductive material by more than 11 m (penetration depth of the method) in the graben. Profile GE4 exhibits a patch of resistive material similar to what is observed on the other profiles. This could be a block of the high terrace buried by the fault. Furthermore, it is overlain with a ~2 m-thick conductive unit which we interpret as water-saturated loess deposits. Considering that the loess/high terrace contact could be located at a depth of 4 ± 1 m and that it can be correlated with the high terrace observed at 5 ± 1 m above the topography on the footwall block, this would suggest 9 ± 2 m of vertical displacement on that fault strand since the deposition of the loess layer, probably older than 26900 years (see TL dating in the trench 3 paragraph) and probably younger than the Wurm last glacial maximum estimated at 70 000 years (Bitterli-Brunner and Fischer, 1988). This yields a minimum vertical displacement rate of 0.1 - 0.15 mm/yr on that fault branch for the Holocene and late Pleistocene, in fairly good agreement with results from geomorphologic and seismic investigations. According to these promising results, trenches were excavated at sites 1 and 2 on the exact location of profiles GE3, GE4 and GE7.

3.7. Paleoseismic Trench Analysis

Geomorphologic as well as geophysical results led us to consider several sites favorable for trenching operations. Due to the high density of buildings and thick vegetation cover along the scarp, available sites were much fewer than previously thought. However, original geomorphology with uplifted terraces and sources of recent sedimentation along the fault scarp were the main criteria for paleoseismic site selection (Fig. 3.4 and 3.8).

On the southern section of the fault (site 1) exploratory short trenches were dug in year 1999 to identify recent deformation structures and faulted young deposits and characterize a proper candidate for the source of recent earthquakes.

Site 2 is located three and a half km to the NNE and was subsequently selected for a detailed paleoseismic study. Although hidden by a small forest, a well-individualized fault scarp offers a clear topographic signature as well as favorable geomorphic features with colluvial and alluvial deposits associated to a recent drainage system.

Age determinations were performed using AMS radiocarbon (Table 3.1) and TL methods (Table 3.3). More than 50 samples of organic material including charcoal fragments, bulk soil and a dog tooth as well as 15 sediment samples for TL analysis were collected in trenches. Charcoal fragments are of good size and shape because they have probably been produced locally since the Bronze age (Reto Marti, personal communication). Radiocarbon samples were prepared following the standard procedure described by Schleicher et al. (1998). Calibrated dates (B.C./A.D.) were calculated using the OxCal software (Bronk

Ramsey, 1995) along with the Intcal98 calibration curve (Stuiver et al., 1998) and are given for a 2σ (95.4%) confidence interval.

Location	Depth (m)	Sample name	Lab code	Material	Fraction	Amount of Carbon (mg)	Corrected pMC	δ13C (‰)	Radiocarbon age (BP)	Uncertainty (years)	Calibrated date (±AD) 2σ range (95.4% confidence)
Trench 1	2	Grab 1	KIA12216	Charcoal	Alkali	3.1	58.22	-26.91	4345	35	-3090
Trench 1	2	Grab 1	KIA12216	Charcoal	Humic	2.2	59.39	-25.39	4185	30	-2890
Trench 1	2	Grab 2	KIA12217	Charcoal	Alkali	4.2	60.49	-27.90	4040	35	-2840
Trench 1	2	Grab 3	KIA12218	Charcoal	Alkali	3.9	69.96	-27.67	2870	30	-1190
Trench 1	2	Grab 4	KIA12213	Charcoal	Alkali	4.3	66.61	-25.20	3385	45	-1870
Trench 3	1	F2.2N	KIA12214	Charcoal	Alkali	5.2	76.23	-25.77	2180	35	-380
Trench 3	1	F2.2N	KIA12214	Charcoal	Humic	0.9	75.31	-26.79	2280	35	-410
Trench 3	1	F2.3N	KIA12220	Charcoal	Alkali	1.1	75.05	-25.57	2305	30	-230
Trench 3	1	F2.4N	KIA12215	Charcoal	Alkali	0.8	76.33	-26.97	2170	35	-370
Trench 3	1	F2.5N	KIA12221	Charcoal	Alkali	5	30.04	-27.95	9660	45	-9240
Trench 3	1	F2.5N	KIA12221	Charcoal	Humic	3.6	30.78	-24.37	9465	50	-8600
Trench 3	1	F2.6N	KIA12222	Charcoal	Alkali	0.3	71.36	-30.66	2710	70	-1020
Trench 3	1.5	F2.7N	KIA13416	Charcoal	Acid	0.5	35.49	-28.46	8320	85	-7550
Trench 3	1.7	F2.8N	KIA13417	Charcoal	Acid	1.2	74.97	-25.13	2315	410	-230
Trench 3	1	F2.9N	KIA13418	Charcoal	Acid	0.6	31.66	-28.71	9240	80	-8690
Trench 3	1	F2.10N	KIA13419	Charcoal	AAA	0.8	75.31	-26.47	2280	35	-410
Trench 3	1.5	T3.T01	ETH-256936	Dog tooth	AAA	1.6	78.3	n.a.	1915	50	-240
Trench 3	1.6	Tarc1	KIA12236	Charcoal	AAA	n.a.	77.28	-26.10	2020	40	-160
Trench 3	2.6	Tarc2	KIA12237	Charcoal	AAA	n.a.	59.43	-23.00	4130	40	-2880
Trench 4	0.7	CW1-1a	KIA12605	Bulk soil	Alkali	1.3	76.71	-25.07	2130	30	-360
Trench 4	0.7	CW1-1a	KIA12605	Bulk soil	Humic	1.2	81.81	-24.27	1610	30	390
Trench 4	0.7	CW1-1b	KIA12606	Shell shell	Alkali	0.7	25.65	-7.08	10930	90	-11250
Trench 4	0.5	CW1-2	KIA12607	Bulk soil	Alkali	1.4	94.41	-27.34	460	25	1475
Trench 4	0.4	CW1-3a	KIA13420	Bulk soil	Alkali	2.9	97.27	-25.35	225	30	1630
Trench 4	0.4	CW1-3b	KIA13421	Charcoal	Alkali	4.7	98.55	-27.25	120	25	1670
Trench 4	0.8	CW1-4a	KIA13422	Bulk soil	Alkali	0.8	70.79	-25.09	2775	35	-1000
Trench 4	0.8	CW1-4a	KIA13422	Bulk soil	Humic	0.5	82.06	-28.05	1590	40	380
Trench 4	0.8	CW1-4b	KIA13423	Charcoal	Acid	0.5	94.88	-28.98	420	40	1410
Trench 4	1.5	CM2-1	KIA12608	Bulk soil	Alkali	1	37.86	-27.45	7800	50	-6800
Trench 4	1.1	CM2-2	KIA12609	Bulk soil	Alkali	0.9	57.16	-25.43	4485	60	-3340
Trench 4	1.1	CM2-2	KIA12609	Bulk soil	Humic	1.2	70.78	-24.84	2775	35	-830
Trench 4	1.4	CM2-3	KIA13424	Bulk soil	Alkali	1.4	58.40	-26.95	4315	35	-2680
Trench 4	1.4	CM2-3	KIA13424	Bulk soil	Humic	0.6	60.20	-26.50	4075	45	-2870
Trench 5	1.4	T5.C03	ETH-25632	Charcoal	Alkali	0.7	67.98	-23.90	3050	65	-1450
Trench 5	2.25	T5.C07	ETH-25633	Charcoal	Alkali	0.9	28.51	-21.20	10030	85	-10150
Trench 5	2.3	T5.C12	ETH-25634	Charcoal	Alkali	1.6	24.94	-17.50	11105	85	-11450
Trench 5	3	T5.C16	ETH-25635	Charcoal	Alkali	0.3	25.05	-23.40	11070	145	-11500
Trench 5	0.65	T5.S02	ETH-25637	Bulk soil	Alkali	1.6	99.19	-22.70	Modern	n.a.	n.a.
Trench 5	0.7	T5.S03	ETH-25638	Bulk soil	Alkali	1.4	100.68	-26.10	Modern	n.a.	n.a.
Trench 5	1.55	T5.S04	ETH-25639	Bulk soil	Alkali	1.6	39.78	-19.90	7355	70	-6390
Trench 5	0.5	T5.S05	KIA-19082	Bulk soil	Alkali	2.6	73.54	-26.39	2025	25	-100
Trench 5	0.5	T5.S05	KIA-19082	Bulk soil	Humic	1.2	88.80	-33.73	1265	25	670
Trench 5	0.7	T5.S06	KIA-19093	Bulk soil	Alkali	1.2	86.17	-22.34	1165	25	770
Trench 5	0.7	T5.S06	KIA-19093	Bulk soil	Alkali	1.2	86.17	-22.34	1165	25	770
Trench A	n.a.	Tarc1	Beta-135096	Charcoal	AAA	n.a.	81.63	-26.40	1580	40	400
Trench A	0.65	TB2_M5	Beta-135094	Charcoal	AAA	n.a.	61.46	-25.60	3860	40	-2470
Trench A	1.65	TB2_S4	Beta-135095	Plant	AAA	n.a.	57.53	-29.70	4390	40	-2900
Trench A	n.a.	TC_nord1	Beta-135093	Charcoal	AAA	n.a.	46.33	-24.70	6130	50	-4850
Trench A	0.4	TC_stud3	Beta-135092	Charcoal	AAA	n.a.	61.00	-24.90	3920	40	-2560

Table 3.1. Results for radiocarbon AMS datation of 45 samples from the Basel-Reinach fault. Age determinations were performed by the Leibniz Labor of the Christian Albrecht University, Kiel, Germany (samples KIA) and the University of Zurich/ETH-Zurich, Switzerland (samples ETH). Conventional ages are 2σ-calibrated using OxCal software (Bronk Ramsey, 1995).

3.7.1. Site 1

Figure 3.9. See separate A3 print outs. a) Location map of detailed logs obtained from trench excavations during this study. b), c), d), f) and g) Trench logs with unit descriptions and age determinations from radiocarbon and thermoluminescence data (see text and dating information tables 2 and 4 for details). e) Re-interpreted log of a construction trench opened in Basel and originally described by Barsch et al. (1971).

Site 1 corresponds to the southern part of the fault which is less urbanized and more accessible for field investigations (Fig. 3.9-a). Well-preserved and uplifted alluvial terraces outline the existence of recent tectonic movements along the fault scarp (unit c1, Fig. 3.9-b).

Trenching operations at this site were difficult to lead mainly because of a dense network of gas and water pipes and of a dense forest cover. Hence, we could only dig two parallel trenches (upper and lower parts of composite trench B, Fig. 3.9-b) of 1 m width, 2 m depth and 6-10 m length across the toe of the scarp.

The bottom of trench A shows gently west-dipping (5-10°) hardened sandy layers with interbedded clays which facies corresponds to the Oligocene substratum (unit g). Colluvial wedges (unit e) made of sandy clay with fine and coarse gravels with at the base an erosional surface (units f1-f2), made of fine gravels in a sandy clay matrix (whitish layers) overlay unit g. Units e, f and g show minor normal faulting with vertical displacements ranging between 0.03 m and 0.62 m. Unit c1 is ~1-m-thick massive silty clay with fine gravels overlaying the substratum g. With a flat top surface wedging out against the scarp this unit may result from an old river-terrace meander. The height of the flat top surface is estimated at 3.5 m with respect to the valley flood field. In trench B the substratum is made of organic-rich clay and hardened sandy clay layers (units d1 and d2). Unit d3 is very similar to colluvial wedges e and covers d1 and d2 unconformably. Units c2 and c3 are present in both trenches and correspond to organic-rich colluvial deposits overlain by a brown soil with scattered gravels (units a1 and a2). In the lower part of the trench, units d1, d2 and d3 are faulted and units c2, c3, a2 and ps are warped. This active deformation with a prominent scarp showing about 0.6 m of vertical movement at the surface topography testifies for the occurrence of a young faulting event. Similarly, unit a3 shows 0.6 m of vertical offset that is likely to be younger than c3 dated at 2470-2200 B.C. and may correspond to the 1356 A.D. Basel earthquake. The penultimate event that corresponds to faulted d1 and d2 can be bracketed between d2 (3270-2900 B.C.) and c2 (2560-2280 B.C.). An older event is suggested by the faulting of units f and e in trench C but no dating is available to determine the age.

3.7.2. Site 2

Site 2 is located on the northern section of the BR fault. This area is heavily urbanized and only a few locations are free of buildings. 6 trenches were excavated for a total length of more than 230 m and a maximum depth of 4 m (Fig. 3.9c-g). Oligocene deposits visible in the trench bottom, are composed with poorly cemented grayish sand with micas, clay lenses and seldom hard sandstone cobbles. These fluvio-lacustrine deposits are attributed to Chattian age as described in the Rhine graben (Alsatian molasse, unit O3, in Bitterli-Brunner and Fischer, 1988). It is covered by the alluvial deposits of the high terrace (Q3s, Hochterrasse Schotter, upper Pleistocene) visible in trenches 4, 5 and 6. This unit is a polygenic conglomerate made of crystalline as well as limestone cobbles and pebbles from the Birs river with a sandy matrix and well-stratified sand lenses. It indicates a cold climatic environment and is associated with alluvial deposits of glacial origin. It can be continuously mapped northward to the Rhine River where it is attributed to the Riss age (Bitterli-Brunner and Fischer, 1988). The upper part of the section changes to a monogenic conglomerate of calcareous pebbles described as the Nagelfluh facies. Its matrix changes to a fine-grained unit of clay and silt probably secondarily deposited by the washing-off of the upper loess cover. In trenches 1, 2 and 3 unit Q3s does not appear and Oligocene deposits are directly covered with late Pleistocene and Holocene deposits. These deposits are made of fine sands (probably re-sedimented loess deposits), gravels and fine gravels with a reddish brown and organic-rich clayey matrix. This may indicate a warmer climate with frequent rainfalls. In trenches 1 and 2, the top of the Oligocene exhibits a very corrugated erosional surface covered with conglomerates of calcareous pebbles with a sandy and clayey matrix. In trench 3, the Oligocene is overlain by (1) fan deposits at the foot of the steepest slope, (2) interfingering gravels and silty clays on the lower half of the scarp and (3) loess and massive dark brown soil at the toe of the scarp. In most places along the scarp, young deposits (Holocene) crop out as either alluvial deposits from the Birs River, fan deposits or colluvial deposits. Finally, as trenches 1 and 2 are very similar we document here only trench 1.

3.7.2.1. Trenches 1 and 4

Trench 1 (see Fig. 3.9-f) is 88 m long and was dug at the same location as electric profiles GE2 and GE3. This trench did not show the main active normal fault but it displayed several minor antithetic faults. Indeed, we stopped the excavation upslope at the base of the scarp because of a tree. An additional trench was then opened 10 m aside across the slope (see description of trench 4) below. The uppermost part of the trench, located on the flat surface, is composed with thick silty clays (unit c Fig. 3.9-f) where 4 dated charcoal samples indicate a late Holocene age (see samples Grab1, Grab2, Grab3 and Grab4 in Table 3.2). Unit c does not show any visible layering and is probably re-sedimented reworked loess sediments. The

antithetic faults present some characteristics of syn-sedimentary ruptures but the absence of clear stratified layers made difficult any assessment of successive faulting episodes. The eastern half of trench 1 presented a thick unit of conglomerates with centimeter to decimeter size that probably belongs to the lower terrace (Table 3.3). As shown in Fig. 9-f, the sandy clay substratum (attributed to Oligocene) is truncated (erosion surface) and overlain by the conglomerates. We interpret these outcrops of a deformed old alluvial terrace over the substratum which forms an individual tectonic block (horst) near the main active fault and a small graben-like structure filled by unit c. In short, although trench 1 did not show a chronology of paleoseismic events, it provides evidence for recent active deformation.

	Climate	Trench 1	Trench 3	Trench 4	Trench 5	Trench A	Trench Barsch	
Holocene		unit a	Event Z					
		unit a	unit b					
		unit b	unit d1	unit c	unit c	unit c	unit c	Event Y
		unit c	unit d			unit d		
			unit c1	unit d				Event X
			unit d2	unit e	unit e			
Pleistocene	Wurm		unit c2					
			unit d3	unit f	unit f			Event W
			unit c3	unit g	unit g			
			unit h	unit h				
			unit d4	unit i	unit i			Event V
			unit c4					
Riss		unit d5						
		unit e	unit f				unit a	
		unit g	unit j	unit j		unit b		
Miocene						unit c		
						unit d		
Oligocene		unit f	unit h	unit k	unit k	unit g	unit e	

Table 3.2: Stratigraphic units related with the Birs Valley and the Basel-Reinach fault scarp. Climate from Haas et al. (1998) and Magny et al. (2001).

Moreover, it is of interest to mention the probable existence of a remain of a roman road (Reto Marti, pers. comm.) which consists on a 10 cm thick sandy gravels layer at the toe of the scarp (within unit a, Fig. 3.9-f). The road seems to be strongly warped with ~1 m of vertical separation suggesting the presence of a fault at depth and a recent coseismic movement. On the other hand, resistivity profile GE2 confirms that the warped geometry could be associated with a deeper fault. On the other side of the road, a construction pit (see eastern section of Fig. 3.9-f) displays more than 4 m of alluvial loam and gravels (unit e, Fig. 3.9-f). According to the resistivity and borehole data from the geological map, the contact between unit e and the Oligocene sands should be at 5 to 7 m depth. Combining resistivity with trench 1, we may correlate the flat bottom of the lower terrace (unit e in Fig. 3.9-f) at location 35 m with the same lower terrace limit at location 105 m and infer a minimum 8 m of vertical displacement. According to the geological map (Bitterli-Brunner and Fischer, 1988),

the lower terrace should have taken place after the last glacial maximum, i.e. ~70'000 years ago (Wurm age). This leads to a minimum 0.11 mm/yr vertical displacement rate for the late Pleistocene and Holocene along this branch of the normal fault.

Trench 4 was excavated across the steepest part of the scarp, at the western end of trench 1. It exhibits a clear normal fault rupture up to the surface with alluvial terrace deposits on the footwall block (Riss-age high terrace, unit j on Fig. 3.9-d) juxtaposed to colluvial wedges with Holocene sandy silt and gravel in the hanging block. The fault shows a ~10-cm-thick gouge zone with deformation bands of grey and white stiff clay and oriented pebbles and gravels. The uppermost Holocene units are made of three episodes of colluvial wedges (units a, c and d on Fig. 3.9-d): (1) unit a is 30-40 cm thick and is made of well stratified pebbles in a clayey matrix. It caps the fault, does not exhibit evidence for deformation and its base material has been dated A.D. 1410-1475 and A.D. 1630-1950 (see samples CW1-2 and CW1-3a in Table 3.2). Unit a is overlain with the present-day soil which is ~20 cm thick. (2) Unit c is 50-60 cm thick and shows at its base an erosional surface which is marked by a group of mixed coarse and middle size gravels dated 360-40 B.C. and 1000-830 B.C. (see samples CW1-1a and CW1-4a in Table 3.1) and overlain by thinner levels of fine gravels in a sandy matrix. (3) The base of unit d also corresponds to an erosional surface where fine and coarse gravels lay on fine silty sand deposits dated 3020-2880 B.C. and 3340-3090 B.C. (see samples CW2-3 and CW2-2 in Table 3.1). This 0.8 - 1 m thick unit consists of well-stratified and nearly horizontal 5-10 cm thick sandy and gravel layers with graded bedding (fine elements to the top) bent and deformed near the fault. The uppermost colluvial levels stratigraphy of trench 4 shows a rather consistent succession of seven ¹⁴C ages.

The lower units e, f, g, h and i (Fig. 3.9-d) are made of massive silt and clay with some aligned pebbles which mark the stratigraphy. It consists of massive fine silt and brown clay with a very few gravels. We sampled for TL age determinations and yielded complicated results. The four samples BAS31 to 34 present a succession of ages 8030-6190 B.C., 15800-12220 B.C., 19400-14180 B.C. and 12430-9310 B.C., respectively, with BAS32 and 34 being on the same stratigraphic level. In this succession, as the lowermost level of unit e presents the youngest age (BAS31), these overlapping ages could be due to reworked colluvial sediments which are not suitable for TL dating method. Furthermore, unit e consists on with very fine-grained sediments in steep slope morphology that likely favours relatively fast sedimentation. Nevertheless, one may note that the sample BAS31 which is located at the lower part of unit e (see also Table 3.3) is in good agreement with the ¹⁴C date 6800-6450 B.C. (see sample CW2-1 in Table 3.1). Taking into account this good correlation and the consistent ¹⁴C ages of corresponding units c, e, f and g in trench 5 (see paragraph below), we think that the TL dating BAS32 to 34 in unit e may not reflect the true depositional age.

Unit f is strongly warped and faulted and shows 20 to 30 cm of vertical displacement across two fault splays one of which presents a reverse geometry (Fig. 3.9-d). These two minor fault ruptures indicate the occurrence of a faulting event that postdates unit f and probably took place during the deposition of unit e. This observation may indicate the occurrence of a seismic event between 8030 B.C. and 6450 B.C..

Location	Sample name	Age BP (yrs)	Uncertainty (yrs)	Date BC		Observation
				Minimum	Maximum	
Trench 3	BAS51	25800	3100	26900	20700	
Trench 3	BAS52	14720	1490	14210	11230	
Trench 3	BAS53	>119000		117000	n.a.	Older than TL range
Trench 3	BAS54	14570	1570	14140	11000	
Trench 4	BAS31	9110	920	8030	6190	Correlates with 14C sample CW2-1
Trench 4	BAS32	16010	1790	15800	12220	
Trench 4	BAS33	12870	1560	12430	9310	
Trench 4	BAS34	18790	2610	19400	14180	
Trench 6	BAS75	>119000		117000	n.a.	Older than TL range

Table 3.3. Thermoluminescence datation results for 9 sediment samples from the Basel-Reinach fault.

3.7.2.2. Trench 3

Trench 3 is 94 m long and was excavated in the footwall inside an incision and across the alluvial fan deposits down to the toe of the scarp (Fig. 3.9-g). Here, the trench location depended on the existence of a path in between many trees and although one may expect a strong erosional activity it exhibited three major normal faults F1, F2 and F3 as well as numerous minor faults. Fault F1 is located at the base of the steepest slope and F2 is 35 m down the slope. F1 and F2 dip steeply to the East (~65°) and show 10-20 cm thick altered gouge zones and deformation bands that include many oriented gravels and pebbles. On the hanging block of F1, and from the bottom of the trench, one may recognize three sequences of colluvial wedges made of coarse gravels with a sandy matrix (unit e1, e2 and e3) overlain by fine sands (unit e). The latter unit was dated at three places using TL which provided ages ranging between more than 117ky B.C. to 14210-11230 B.C. (see Fig. 3.9-g and samples BAS52, BAS53 and BAS54 in Table 3.4). If these units can result from the erosion of fault scarps, each sequence may result from a scarp-degraded process and be correlated with a paleoseismic event. Hence, the oldest observable event on that fault could have occurred before 117ky B.C. with a vertical displacement of at least 0.5 m. Another paleoseismic event may have taken place before 26900-20700 B.C. and be responsible for a minimum ~0.5 m vertical slip as inferred from the thickness of colluvial units (Fig. 9-g). A more recent paleoevent took place before 14210-11230 B.C. and produced a larger displacement of ~1 m. As inside any incisions, the uppermost overlaying deposits (alluvial fan deposits a1 and

a2) truncate and cap the fault and erase the geological record (and most probably the most recent displacement). However, down the slope the four generations of fan units a1, a2, a3 and a4, reaching a total thickness of more than 3 m, were deposited after the erosional unit b (possibly artificial?) i.e., after 410 - 40 B.C. (see samples F2.2N, F2.3N, F2.4N, F2.6N, F2.8N and F2.10N in Table 2). Moreover, ¹⁴C dating of sample T3.T01 (lowermost deposits of unit a2, Table 4) indicates that units a1 and a2 are younger than 20 B.C.- A.D. 240. Recent movements on F1 which is truncated by a1 and affect a3 can be at the origin of the fast accumulation of the thick alluvial fan deposits and the most recent movement may have occurred after a2, i.e. after A.D. 240.

The second normal fault F2 exhibits a similar geometry with a minimum thickness of 5 m of accumulated recent deposits on the hanging wall (see Fig. 9-g). Against the fault, unit d5 displays densely packed gravels with a cemented block of sub-vertically oriented pebbles and sandy layers. Close to the surface, unit c5 which is a 20 cm-thick silty loess layer dated 14140 – 11000 B.C. by TL (see sample BAS54 in Table 3) is strongly warped and faulted with ruptures showing a reverse geometry. TL dating of trench 3 concerned samples with a sedimentary environment characterized by both low energy alluvial and colluvial deposits. This is attested by the small size and sandy silty units associated with channel structures and small to middle size conglomerates in colluvial wedge units. Hence, TL age determinations seem to be in good agreement with the stratigraphic succession and the ¹⁴C datations. Tectonic features of trench 3 near F2 can be interpreted as typical of hanging wall structures of a major normal fault (McCalpin, 1996). Faulting events here are at least younger than 14140 B.C.. A sequence of colluvial gravel wedges with units d1 to d4 alternating with thick (1-2 m) silty clay deposits of units c1 to c4 displays a consistent succession of TL and ¹⁴C ages. In fact, ¹⁴C dating of nine samples from units d4 to b spans the time between 8690 B.C. to 40 B.C. (see Fig. 9-g, near fault F2). The hanging block shows a stratigraphy with a progressive dip of ~0°, ~8°, ~19° and ~30° illustrating an anticlockwise rotation increasing with distance from the fault. Four identified gravel wedges constitute reference levels which are composed with rounded limestone gravels with no visible stratigraphy in a silty clay matrix similar to units c1 to c4. As these four units display a typical debris facies followed by a wash facies, they also contain elements only from the footwall and are incrementally deformed against the fault. We infer that they constitute a series of colluvial wedges associated to successive co-seismic displacements on fault F2.

An alternative interpretation could be invoked explaining the progressive anticlockwise tilt of units d as gravity-related landslide process. This interpretation is not supported, however, neither by the antithetic normal faults located east of F2 (see F2', Fig. 9-g) nor by the warped unit c5 with reverse geometry in the hanging block nor by the imbricated parallel main normal faults F1, F2 and F3 visible at the surface and at depth (see

geophysical investigations). Moreover, deformation bands and warping of numerous white CaCO₃ levels in the footwall block near the gouge zone reflect the long-term deformation with high level of friction that does not support the landslide interpretation. The microscopic study of grain size, related mineralogy and structure of the gouge zone reveals two stages of deformation with i) a ductile deformation with folding and production of chlorite, and ii) a brittle behavior with fractured minerals and development of illite in the gouge zone (Orellana, 2002).

On the hanging wall, three meters east of F2, unit b which constitutes the base of unit a4 seems to be slightly warped and broken upon the flexured silt layer unit c5. It thickens to 1 m as it interfingers eastward with the sequence of units d and c. The numerous ¹⁴C datations of unit b (all younger than 410 B.C.) predate the youngest deformation event probably associated with a movement of a hidden fault at depth.

Between stations 65 m and 75 m, thick gravel deposits (unit d5) display well-stratified levels with ~20 cm thick loess lenses which are warped and displaced by minor antithetic normal faults with ~10-20 cm vertical displacements. The easternmost loess lens is cut and displaced by a major antithetic normal fault that shows ~1 m of vertical separation, truncated by the alluvial fan deposit unit a4. More to the east, several other antithetic faults marked by sandy lenses are sharply truncated by unit a4.

On the eastern side of the road, a team of archaeologists from the Canton of Basel opened several excavations in 1999, one of which is aligned with trench 3 (see lower section on Fig. 9-g). The trench was enlarged for us to allow investigations on the fault zone. A small and well-expressed vertical fault with a ~10-cm-wide gouge zone showing oriented pebbles and gravels and a clear cut of a pottery-rich Bronze Age unit were exposed (unit d in Fig. 9-g). In this trench, the relationship between faulted d covered by units c and b (supposed roman road) indicates the occurrence of the penultimate paleoearthquake between 2880 - 2570 B.C. and 160 B.C. - 80 A.D. (see samples Tarc1 and Tarc2 in Table 1).

3.7.2.3. Trench 5

Trench 5 was excavated on a similar location as trench 4 and about 30 m to the south. It unveils very similar structures to trench 4 as well as complementary information on stratigraphy and successive faulting episodes (see Fig. 9-c). A sharp rupture cuts through alluvial terrace deposits (Riss-age high terrace, unit j) and slope deposits from the base of the trench up to a depth of 1 m below the surface. A 20 to 30-cm-thick gouge zone displays deformation bands with two fault strands at depth with numerous oriented gravels and pebbles. As in all the other trenches opened at site 2, Oligocene sands (unit k) crop out at the base of the footwall and can be considered as the substratum (pre-Quaternary bedrock). At the contact between unit k and the main fault, a 40 cm thick zone shows very high clay

content, iron oxide coloration, a shear fabric and a significant increase of water content. Terrace deposits composed with conglomerates of crystalline origin, and boulders and pebbles in a sand-rich matrix (unit j) overlay the substratum. Two small secondary faults affect and displace sandy gravel units with ~ 20 cm of vertical separation. Unit a, dated 'modern' (see sample T5.S02 in Table 2), caps the fault and shows no sign of deformation. It overlays a 1-1.2 m thick unit made of massive clayey silts of 'modern' age and contains some scattered gravels near the base (unit b). Unit b covers a wedge of 1-m-thick densely packed limestone gravels with a clayey matrix (unit c). That unit pinches out down slope and displays graded bedding upon an erosion surface. It is dated 1450-1110 B.C. (see sample T5.C03 in Table 2). Close to the main fault, unit c is ruptured and vertically displaced by two fault splays which form a 30 cm deep small graben. Unit c lays unconformably over unit e, composed with massive brown clay with scattered limestone gravels. In accordance with age determinations from trench 4, unit e topmost part is dated 6390-6060 B.C. (see samples T5.S04 and CW2-1 in Table 1), suggesting either an unlikely gap in sedimentation processes or a strong erosion of unit e before deposition of unit c. Unit e covers unit f, another colluvial wedge made of more or less stratified gravels in a dark clay matrix. Laying over an erosional surface, the base of unit f contains some large charcoal pieces (over 0.5 cm³), one of which is dated 10150-9250 B.C.. This is consistent with results from trench 4 where the base of unit e was dated 8030-6190 B.C.. Unit g is made of massive clayey silts which contain some scattered gravels. A few imbricated pebbles suggest a source located up the slope and charcoal samples provided very close radiocarbon dates with 11450-10700 B.C. for the top, and 11500-10700 B.C. for the base (see samples T5.C12 and T5.C16 in Table 1). Note that the content of carbon extracted from sample T5.C16 is very small (0.3 mg), which may not provide an accurate date. Underlying unit h is made of dark beige silts with gravels and dips ~40° towards the valley. Its upper part is completely incorporated into the gouge zone and indicates a strong degree of deformation. Unit i is very similar to unit h but it contains fewer gravels. It is highly warped and deformed and almost completely reworked within the shear zone. Both units h and i do not contain enough organic material to ensure proper radiocarbon dating and their grain-size content is not suitable for TL analysis.

Trenching operations as well as sub-surface geophysical surveys suggest that a young (Holocene) fault branch should be located exactly below the road. About 50 m north of site 2, trench 6 (see Fig. 9-a) was opened to check if a fault strand could be detected beside the road. Excavating operations were limited by man-made structures and stopped 4 m before reaching the road. The absence of a fault affecting young alluvial and colluvial units in trench 6 confirmed the geophysical results.

Commercial excavations opened in 1962 for construction purposes were located coincidentally on the northern continuation of the fault (Barsch et al., 1971). The authors provide a detailed geological description of trench walls and recognized clear fault ruptures affecting young sediments with oriented gravels and pebbles within a damage zone (Fig. 9-e). The presence of a fault affecting late Quaternary units 2.5 km NNE of paleoseismic site 2 and along the BR fault scarp indicates the likely northern continuation of the BR fault into the city of Basel.

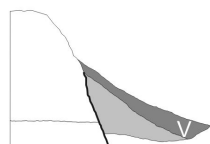
3.8. Summary

3.8.1. Paleoseismic events inferred from trenching

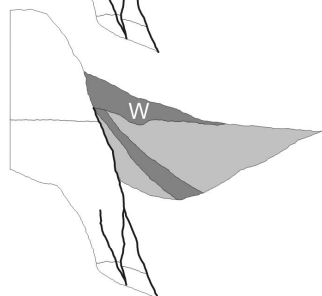
The two paleoseismic sites along the BR fault scarp have revealed evidence for Holocene and late Pleistocene normal surface faulting. Sedimentological conditions combined with the successive movements on the fault allowed the record of past seismic events. Furthermore, the analysis of fault displacements and sedimentary units leads to the identification of coseismic events. We present in the following the successive paleoseismic events beginning with the most recent:

- event Z (A.D. 500 – A.D. 1450): this event can be observed at site 2 on fault 1 (see unit a in Fig. 9-d and unit a in Fig. 9-c), on fault 2 as a flexure of units b and a4 and probably at site 1 (see warping of the present-day soil). It displays a minimum vertical displacement of 0.5 m. This yields a minimum moment magnitude of $M_w = 6.2-6.5$. We correlate the faulting event with the last known historical seismic event of A.D. 1356.
- event Y (2490 B.C. – 2210 B.C.): this event can be observed at both sites on all major fault branches as very well expressed colluvial wedges (see unit c in Fig. 9-d and Fig. 9-c and unit c3 in Fig. 9-b). It was probably the strongest Holocene event on the BR fault. The minimum vertical displacement measured in trench 5 gives 1 m, which yields a minimum moment magnitude of $M_w = 6.4-6.7$.
- event X (6200 B.C. – 3200 B.C.): this event can be observed at site 2 on fault 1, inside trench 4 (see unit d in Fig. 9-d). In trench 5, the very rough top surface of unit e suggests that intense erosion processes may have removed the corresponding event horizon. With a thickness of 0.8 m, unit c corresponds to a minimum $M_w = 6.4-6.6$ event.
- event W (8030 B.C. – 7300 B.C.): this event is observed at site 2, on faults 1 and 2 and it is associated with the well expressed colluvial wedge of unit d3 (Fig. 9-g). The colluvial wedge displays a thickness of at least 0.7 m. This yields a minimum moment magnitude of $M_w = 6.3-6.6$ for event W.

- event V (11200 B.C. – 9500 B.C.): this event is observed at site 2 on both fault 1 (see unit f in Fig. 9-c and Fig. 9-d) and fault 2 (see unit d4, Fig. 9-g). The associated colluvial wedge has a thickness of 0.8 m, which corresponds to a minimum Mw= 6.4-6.6 event.

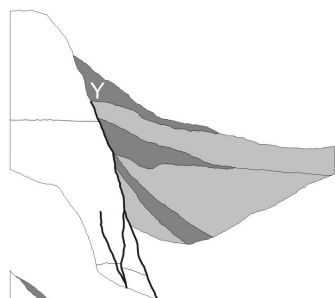


Event V. During background deposition of unit i, the fault breaks up to the surface. Then, a colluvial wedge (unit h) is deposited as an event horizon.
Vertical displacement: 0.8 m.
Date: 11200 B.C. - 9500 B.C..

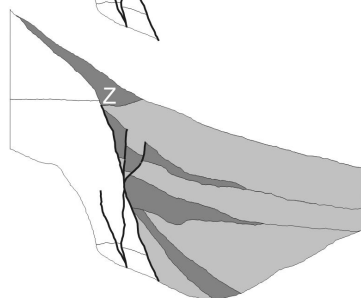


Event W. Background sedimentation goes on as deposition of clayey silt with few gravels (unit g). The fault breaks again and a second event horizon (W) is deposited.
Vertical displacement: 0.7 m.
Date: 8600 B.C. - 7300 B.C..

Event X. This event is not strong enough to produce surface ruptures as it does in trench 4 or intense erosion processes erased related geologic information.
Vertical displacement: 0.8 m.
Date: 6200 B.C. - 3200 B.C..



Event Y. Less clayey silt (unit e) is deposited until the next event. This third colluvial wedge (unit c) contains numerous stratified pebbles and is very well expressed.
Vertical displacement: 1 m.
Date: 2490 B.C. - 2210 B.C. (from site 1).



Event Z. Deposition of Y seems to continue nowadays. It has been faulted during event Z and truncated by the associated horizon.
Vertical displacement: 0.5 m.
Date: A.D. 500 - A.D. 1450.
 This event corresponds to the 1356 Basel earthquake.

Figure 3.10. Reconstruction of faulting events identified in trench 5. Each event is characterized by its corresponding event horizon (colluvial wedge), the associated vertical displacement and the time range of occurrence for the event, as determined by the Bayesian statistical analysis (see Fig. 11). The last situation is the actual trench log (Fig. 9-c).

Reconstruction of paleoseismic events of Figure 3.10 illustrates the successive faulting events in trenches 4 and 5. The Bayesian analysis of 17 radiocarbon dates and one TL age (Fig. 3.11) is performed on a stratigraphic sequence basis. Events are inserted with respect to their stratigraphic position. The output provides a consistent chronology of deposition and faulting where each sample is characterized by its agreement ratio within the model and an optimized time bracket for the occurrence of each event. This analysis is completed for each major fault branch and with a combination of observations from all trenches (Fig. 3.12). The synthesis of trench observations and correlation of faulting events indicates that events Z and Y are well constrained and their related surface ruptures were probably visible along most of the BR fault scarp. Events X, W and V are relatively less well constrained but the faulting analysis suggests that coseismic surface ruptures took place on both F1 and F2 fault branches. The paleoseismic analysis shows that events Y and W are bracketed within 280 and 800 years, respectively. These results allow us to extract an average recurrence interval of 2300 - 2600 years for earthquakes similar to the 1356 event.

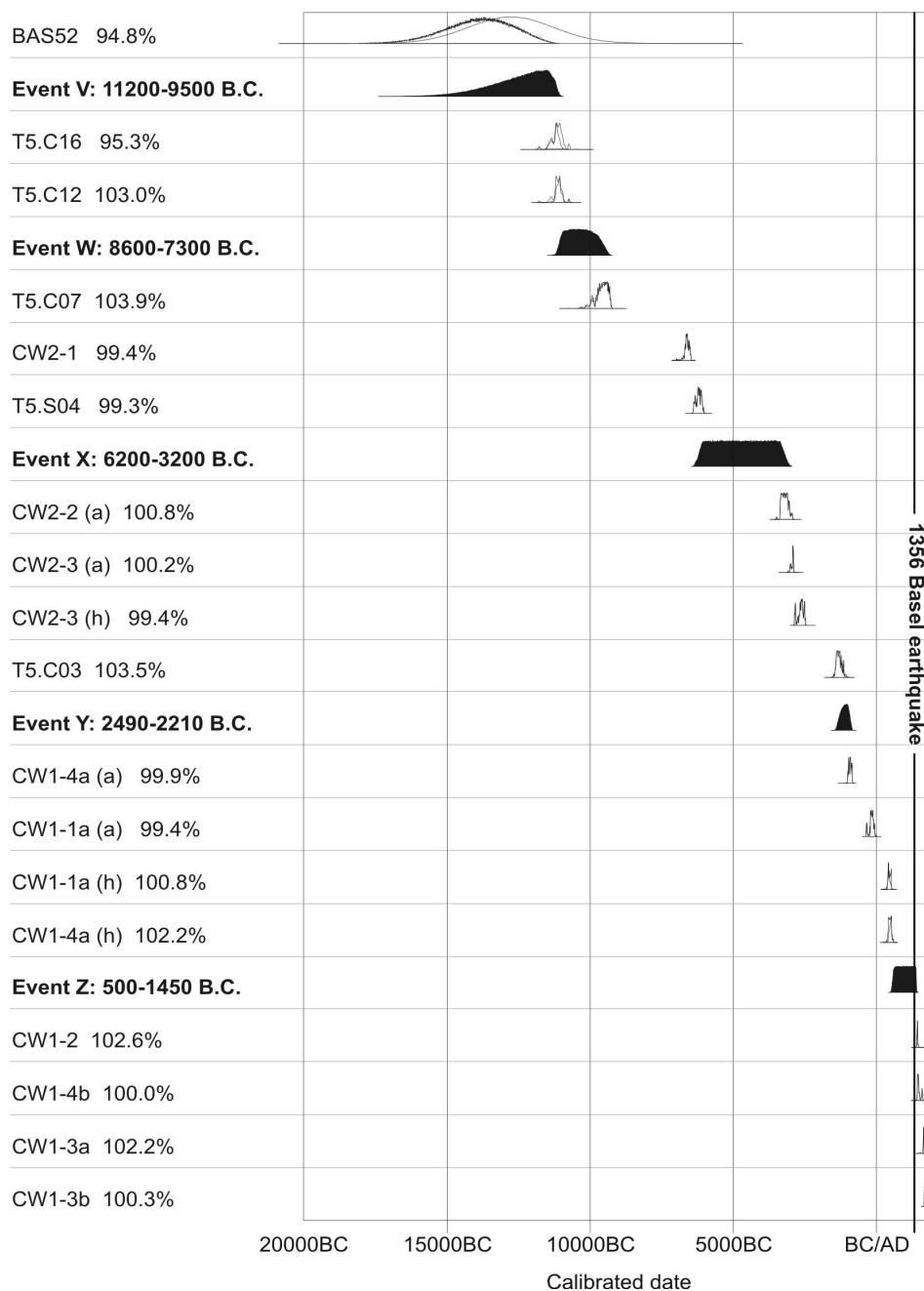


Figure 3.11. Bayesian statistical analysis of radiocarbon data for fault 1 at site 2. Radiocarbon ages are ordered in a sequence following stratigraphic relationships deduced from trench observations. Events were included on the same basis. Percentages indicate individual agreement of data within the sequence. Overall agreement is 100.2%. Atmospheric data from Stuiver et al. (1998); OxCal v3.8 see Bronk Ramsey (1995). The process was performed for each fault branch at each site and for the overall dataset.

Moment magnitudes estimated following Wells and Coppersmith (1994) relations taking into account a fault length ranging from 11 km to 15 km and a thickness of the seismogenic crust ranging from 12 km to 20 km yield $M_w = 6.2$ to 6.7 . However, for a normal

fault scarp with displaced horizontal surfaces and related erosion processes (Wallace, 1977), the thickness of a colluvial wedge may reach half of the co-seismic scarp height, i.e. half of the vertical co-seismic displacement. The amount of vertical co-seismic displacement could therefore be underestimated and a larger vertical slip would yield $M_w > 6.7$.

3.8.2. Events identified within other geological archives

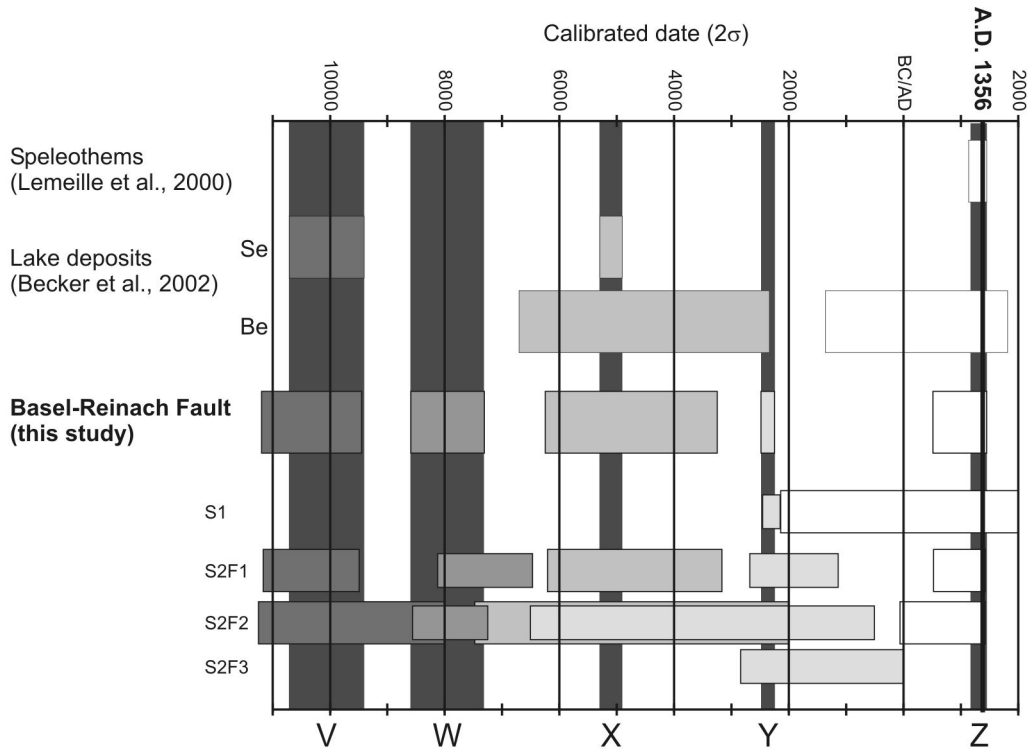


Figure 3.12: Holocene seismic history of the Basel-Reinach fault as deduced from trench investigations at sites 1 and 2 compared to events inferred from various independent geological archives in the epicentral area of the 1356 Basel earthquake. Light shades of grey refer to events identified for individual fault branches (S1: site 1; S2F1: site 2, fault 1; S2F2: site 2, fault 2; S2F3: site 2, fault 3) or individual archives (for lake deposits, Se is for lake Seewen, Be is for lake Bergsee. See Fig. 3 for location). Darkest grey indicates correlated events with time ranges minimized following individual datations. Note that events Z (1356 Basel earthquake) and Y clearly produced surface ruptures at both sites and along 2 of 3 branches at site 2. Older events X, W and V were only identified at site 2 but on two fault branches. Events Z and X are clearly correlated across independent geological archives (BR fault and lakes Seewen and Bergsee), thus potentially improving the datation of event X.

Recent studies in the epicentral region of the 1356 Basel earthquake investigated various indirect evidence of past earthquakes using geological archives. Damage to speleothems

were studied in two caves located on the Blauen anticline, south of the Birs valley (Fig. 3), and yielded the identification of an event dated A.D. 1165-1400 well correlated with the 1356 Basel earthquake (Lemeille et al., 1999). On the other hand, sedimentary records of Lakes Seewen and Bergsee (Fig. 3) were drilled and dated and the seismites analysis permitted the detection of three events for the last 12000 years (Becker et al., 2002). Compared chronologies (Fig. 12) show a fairly good correlation between events X and V inferred from our paleoseismic investigations and from speleothems study and seismites in Lake Seewen.

3.9. Discussion

The identification of a seismic source for the 1356 Basel earthquake is achieved by means of a paleoseismic analysis along an 8-km-long fault scarp. The successive vertical displacements on the BR fault and related colluvial wedges document the occurrence of five earthquakes in the last 13200 years and suggest a recurrence interval of ~2500 years for large to moderate earthquakes. The 54 dating results of radiocarbon and TL analysis provide the timing of the faulting episodes and yield an uplift rate of about ~0.27 mm/yr in the Holocene and late Pleistocene (Fig. 3.13-a). This uplift rate averages at 0.1 mm/yr over the Pleistocene.

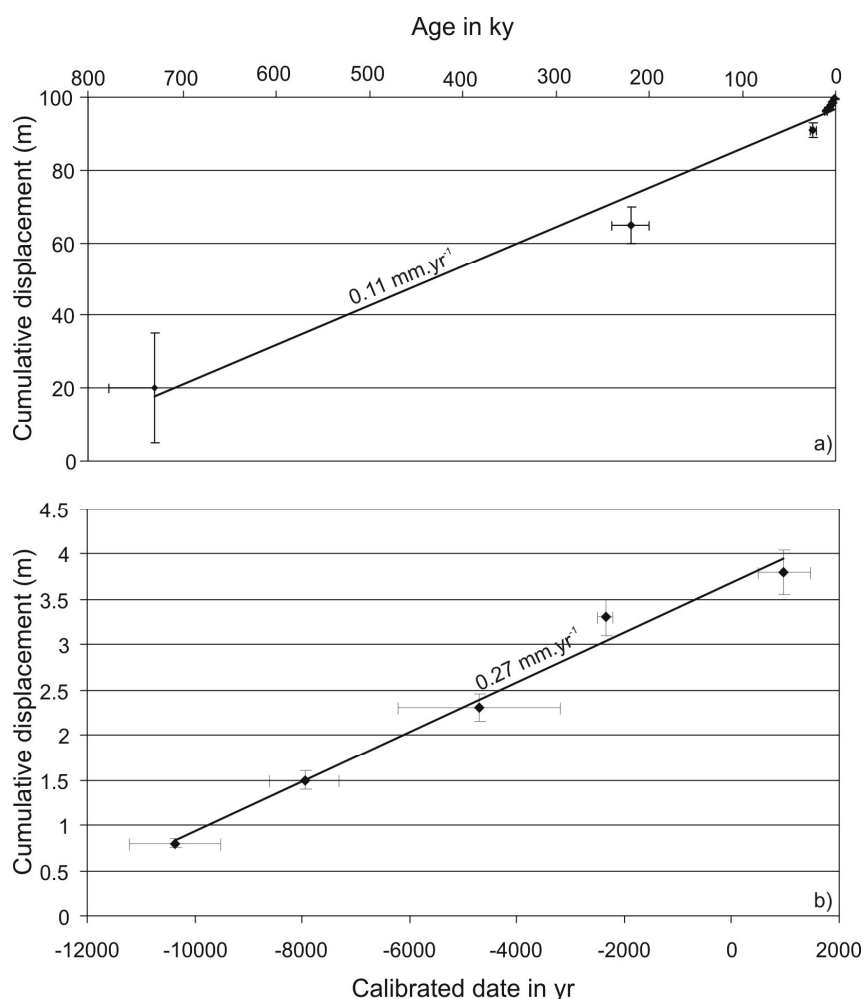


Figure 3.13. a) Long-term uplift rate as determined from Quaternary alluvial terraces cropping out along the BR fault scarp.

b) Cumulative displacement as a function of time for the late Pleistocene and the Holocene along the Basel-Reinach fault. Inferred displacement rate of 0.27 mm/yr is in good agreement with previous results (Meghraoui et al., 2001). Trend line fits well data points with $R^2 > 0.98$.

3.9.1. Faulting geometry and length extension

Trenches across the BR fault have revealed a complex surface faulting geometry. In trench 4, where the bedrock crops out over a depth of 2 m, the fault dips from 75°ESE as it cuts through a fluvial terrace (unit j) to 50°ESE in the bedrock (unit k). This suggests that significant opening may be expected as part of the co-seismic displacement close to the surface. Besides, the 94-m-long trench 3 shows the existence of a double branching of the main fault to form en-echelon blocks with probable simultaneous successive displacements. This is attested by the occurrence of well-expressed colluvial wedges on the hanging wall with progressive tilt of gravels and fine sand accumulation in the nearby small graben structure of site 2 (Fig. 3.9-g). Complex seismogenic ruptures show about 50-100-m-wide surface breaks with main faults, antithetic and secondary cracks along normal faults during large earthquakes such as the Borah Peak large event (Ms 7.3, 1983 in Idaho, Crone et al. 1988). Rotated sedimentary units in the hanging wall of an active fault illustrate a coseismic flexural deformation likely associated with an antithetic fault at depth. A similar faulting structure was observed in trenches excavated across the Wasatch normal fault at Kaysville where the bending of the hanging wall sedimentary units leans progressively toward the fault plane (Swan et al., 1980; Stephenson et al., 1993 and McCalpin et al., 1994).

The Bruderholz scarp provides a surprisingly clear geomorphic signature for the BR fault over a distance of 8 km. This is a minimum observed length while the dislocation model of a fault capable to produce vertical co-seismic displacements of 1 m may reach a Mw 6.7 and related intensity IX-X earthquakes (Kanamori and Anderson, 1975; Ambraseys and Free, 1997). This suggests that the fault likely extends to the north and/or to the south. The northern rim of the Bruderholz scarp is completely erased by the Rhine River and dense urbanization. However, early 1960s construction works along the BR fault in the southern suburbs of Basel (Barsch et al., 1971) exhibits evidence for late Pleistocene-Holocene faulting (Fig. 9-e). Hence, a northern extension of the BR fault through the city of Basel is very likely. It may then connect to the Wiese valley which similar morphology is mainly inherited from the Rhine Valley flexure.

To the south, the BR fault does not display a noticeable morphology as it meets the frontal folds of the Jura Mountains. The topographic signal of the Blauen fold (see Fig. 4) strongly overprints any component related to the fault. However, field investigations permitted us to find broken and faulted limestone units on the crest of the Blauen along the rigorously southern extension of the fault. Besides, the electrical tomography profile GE6 (see Fig. 8) exhibits resistivity contrasts which geometry suggests the presence of a major fault with more than 40 m (penetration depth) of vertical displacement at station 200 and two secondary recent faults at stations 250 and 300 which affect shallow sediments. Such a detectable vertical displacement indicates that site 3 is not the southern end of the BR fault which probably extends partly through the Blauen.

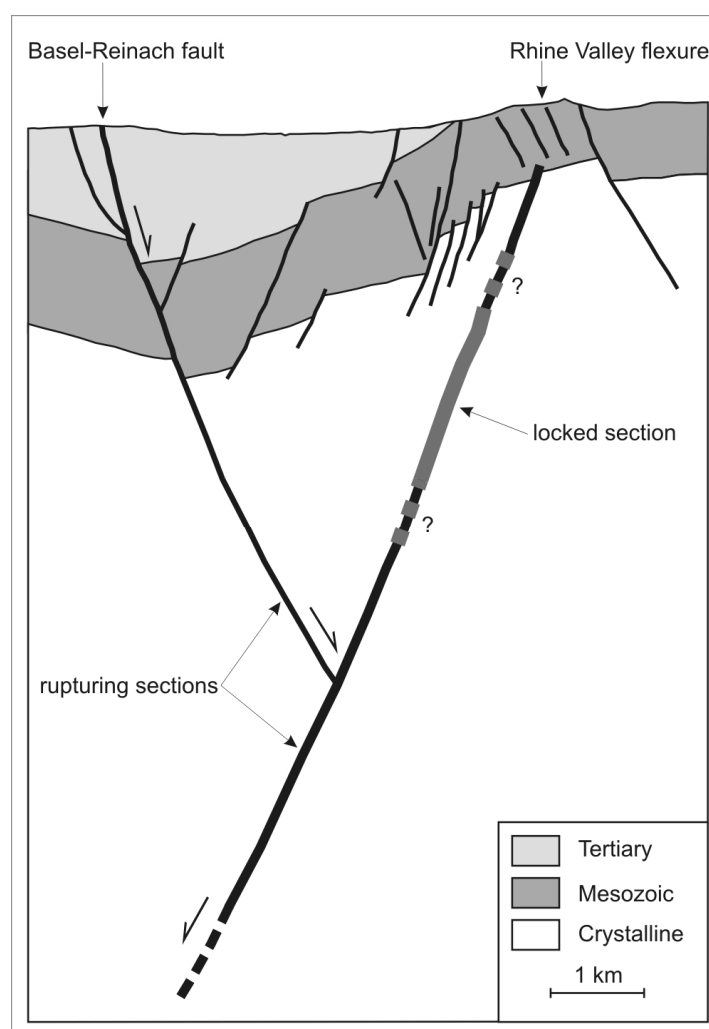


Figure 3.15: Geometry of the Basel-Reinach fault (BRF) at depth. Rupture nucleation possibly occurs close to the junction point and propagates upwards along the BRF as the upper section of the Rhine Valley flexure fault (RVFF) is locked. The rupture area probably encompasses the whole seismogenic crust and a length comparable to the RVFF's, i.e. 20 km. Activity is only recorded on the BRF. Modified after Gürler et al., 1987.

At depth, the Basel-Reinach fault should intersect the regional Rhine Valley flexure fault (RVFF) at a depth of 6 to 7 km (Fig. 15). However, it is unlikely that the BRF cuts through the RVFF and should rather be considered as a well-developed splay or antithetic fault. As we could not evidence any sign of recent activity on the RVFF, we suggest that ruptures nucleate at depth, possibly close to the faults junction and propagate downwards along the RVFF and upwards along the BRF as the upper section of the RVFF would be locked. Consequently, the border RVFF system is likely to be active and its activity documented along the BRF.

3.9.2. Seismotectonic characteristics and deformation rate

If the best stress tensor found by the inversion of the regional focal mechanism (Plenefisch and Bonjer, 1997) is applied to the BR fault, assuming that the fault dips 80° to the East, a normal component of motion is inferred but with a dominant left-lateral motion. Results from the geomorphological and paleoseismological investigations point toward a dominant normal faulting component on the fault without excluding a strike-slip component.

This apparent contradiction may signify that the fault is not responding in a straightforward way to the regional stress tensor. Hence, the regional stress tensor obtained from small to moderate size earthquakes may not reflect very local stress conditions, and the solution found by the inversion should be representative of the actual regional stress tensor. A possible explanation for the inconsistency may be that some left-lateral motion on the BR fault exists but has not been observed because our trenches are dug normal to the fault and because strike-slip offsets on slow faults are more easily erased by erosion than vertical offsets. Near-surface stress measurements (Becker, 2000) indicate that the maximum horizontal stress displays smooth variations around an N-S direction over NE Switzerland. Nonetheless, it also points to a well-constrained strong heterogeneity marked by E-W measurements at the eastern edge of the Laufen basin (Fig. 3.3) located south of the Birs valley. If applied to the deeper crust, this could bias the representativity of the stress tensor inferred from focal mechanisms.

Plotting cumulative displacement as a function of time (Fig. 3.13) reveals a very constant vertical deformation rate of 0.27mm/yr for the late Pleistocene and the Holocene in good agreement with previous works in the Rhine graben (Meghraoui et al., 2000; Meghraoui et al., 2001). It is as well-consistent with a recent study of the ITRF97 velocity field (Nocquet et al., 2001) which suggests active NW-SE extension of 1-1.5 mm/yr within the lower and upper Rhine graben structures. In their paleoseismological analysis of the Bree fault, Meghraoui et al. (2001) inferred a mean vertical deformation rate of 0.07 mm/yr and a mean recurrence interval of ~15,000 yrs for the Bree fault. These parameters are similar to those

determined for other stable continental regions (Bossu et al., 1996 and Crone et al., 1997) but differ somehow from those of the BR fault. With a mean vertical deformation rate of 0.27 mm/yr and a mean recurrence interval of 2500 yrs, the BR fault seems to display a faulting behavior similar to what has been observed along the Apennines ranges in Italy (Pantosti et al., 1993, D'Addezio et al., 2001).

3.9.3. Implications for the seismic hazard

In areas of slow faults and moderate seismicity, the historical record is too short to cover the cyclic recurrence of large earthquakes. Paleoseismology may extend the historical record and provide a basis for a more realistic evaluation of the seismic hazard. Our objective is to achieve a probabilistic seismic hazard assessment to produce models of earthquake recurrence and subsequently estimate probability of ground shaking. We calibrate the earthquake recurrence model introducing the paleoearthquake record of the Basel-Reinach fault.

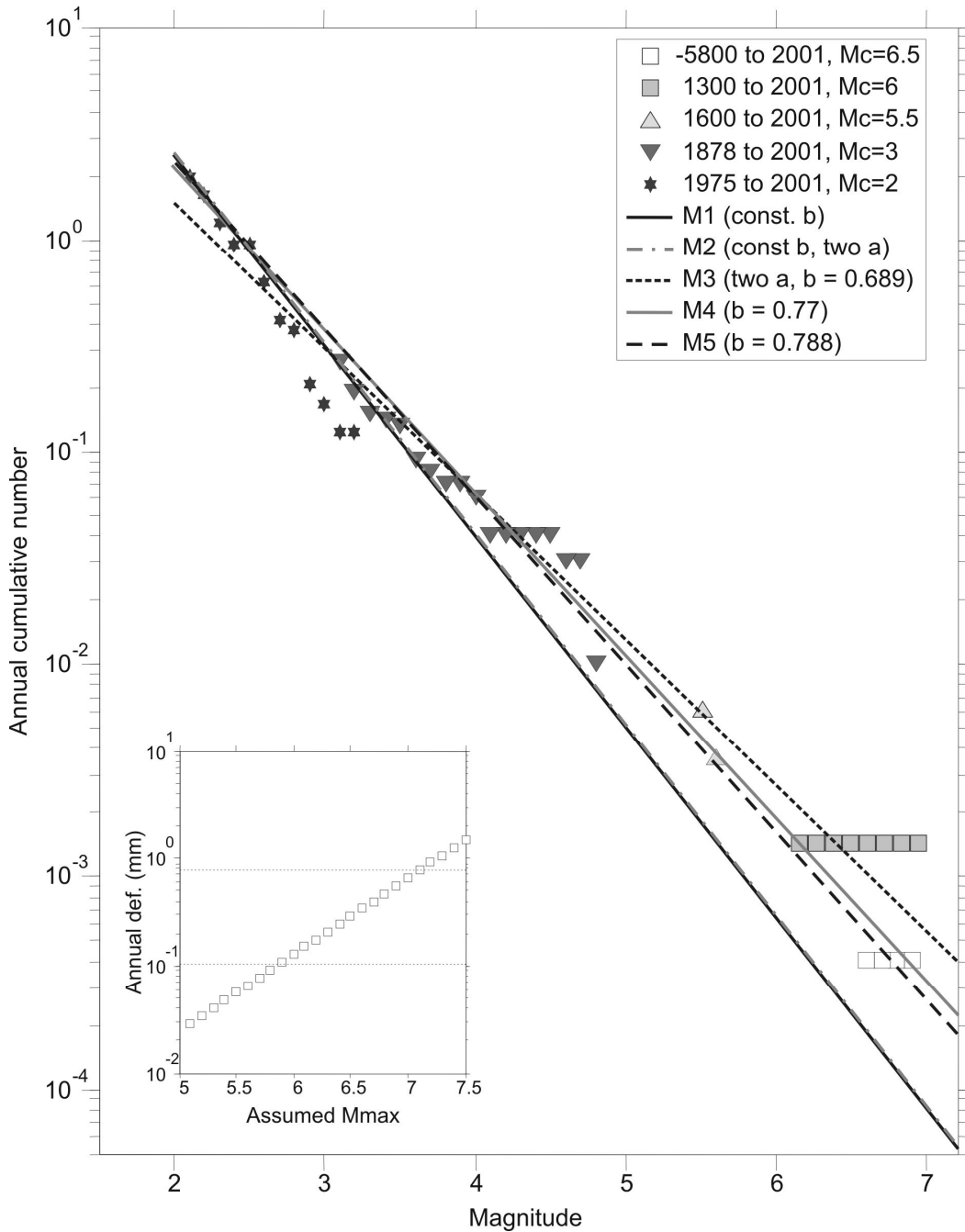


Figure 3.14: Cumulative annual rate of events as a function of magnitude for events in the Basel region. Symbols indicate five different completeness periods models: M1, fixed $b = 0.9$, variable a -value (AIC: 66.505, a -value = 2.2, b -value = 0.9, weight = 0.18); M2, fixed $b = 0.9$ and two variable a -values, one for the instrumental data (1975 – 2001) and one for the historical period 1878 – 1975 (AIC: 68.487, a -value = 2.22, b -value = 0.9, weight = 0.068); M3, variable b -value and two variable a -values (AIC: 66.322, a -value = 1.56, b -value = 0.69, weight = 0.2); M4, variable b and a -values (AIC: 65.81, a -value = 1.89, b -value = 0.77, weight = 0.26); M5, Bayesian error weighted b -value (the weight between 0 and 1 is determined proportional to the uncertainties and sample sizes of the two b -values, AIC: 65.589, a -value = 1.94, b -value = 0.79, weight = 0.29). The small inset displays the annual strain rate in mm as a function of assumed M_{max} , using a Kostrov model (Kostrov, 1974) with a 15 km depth extend of the seismogenic zone. The annual rate of deformation is about 0.2 mm/yr on the basis of

paleoseismological data (Meghraoui et al., 2001), and about 0.8 mm/yr on the basis of historical data solely (Fäh et al., 2003).

Using the Earthquake Catalogue of Switzerland from A.D. 1300 (Fäh et al., 2003), de-clustered following the Reasenber approach (Reasenber, 1985), we defined the Basel seismic source according to the polygon: 48.07N-7.60E, 48.05N-8.01E, 47.43N-7.76E and 47.45N-7.35E. In addition, we add the three most recent earthquakes for the past 7800 years including the AD 1356 event, as observed on the Reinach fault paleoseismic study ($M_w = 6.4 - 6.7$ from Meghraoui et al., 2001 and this study). According to the recent re-evaluation of the historical seismicity of Switzerland (Fäh et al., 2003), we assume that all of the three events have the same magnitude $M_w = 6.9 \pm 0.5$. The recurrence parameters are calculated using the maximum likelihood approach that incorporates the completeness periods (Bender, 1983) and its ZMAP implementation (Wiemer, 2001). We assess the fit of five models to the long-term and short-term seismicity in the Basel region (see M1-M5 in Fig. 14). The selection of the preferred model is based on the Akaike Information Criterion (AIC) score (Imoto, 1991; Ogata, 1999).

Models 4 and 5 obtain the best fit to the seismicity of the Basel region, as seen in Figure 14. A key element is the single paleoseismic point (3 events in 7800 years). This point receives a high weight in the inversion as it provides a constraint over a long period of time. Our preferred b -value (0.79) is significantly lower than the national 0.9 average, and provides an overall good fit to the instrumental, historical and pre-historical seismicity. If only the historical record was available, we would obtain a b -value of 0.68, resulting in an erroneous, too large contribution of large earthquakes in the assessment of seismic hazard. This is a consequence of the different return period for the 1356 event as estimated from the historical record and in the paleoseismic record.

Finally, we perform a simplistic estimation of the annual strain rate in the Basel region for the best fitting model, assuming that all earthquakes have the same focal mechanism, and adopting a Kostrov formulation (Kostrov, 1974) with a 15 km thickness of the seismogenic layer. The annual deformation across the Basel area is displayed in Figure 3.14 as a function of the assumed M_{max} . For example, $M_{max} = 5.9$ would result in an annual deformation of 0.1 mm, while $M_{max} = 7.2$ results in a deformation rate of about 0.21 mm/yr (inset Figure 3.14, dashed horizontal line). This estimate is derived using the best model in Figure 14, and thus including the paleoseismic data for the last 7800 years.

Acknowledgements

We are grateful to many earth scientists who visited the trenches and provided fruitful discussions. Walter Frey (Geoconsult) conducted high-resolution reflection seismics, Leibniz Labor (Kiel) and ETH Zurich radiocarbon datations and Quaternary TL Surveys TL datations. We thank the students and colleagues who helped for fieldwork, especially Peter Schürch, Ina Spottke and Hubert Mvondo and the technical team from IPG Strasbourg. We are grateful to Stefan Wiemer for his contribution to Figure 14 and to discussion about earthquake recurrence. We thank the community of Reinach and the Bürgergemeinde of Reinach for providing access to properties and technical help in the field. Early investigations along the Basel-Reinach scarp were funded by the PNRN (CNRS – N° ...). More detailed investigations were supported later on by the SAFE project of European Commission (EVG1-2000-22005), the Swiss National Fund and the HSK (Swiss Federal Nuclear Safety Inspectorate).

Note: for publishing reasons, Figure 15 could not be included in the final published version. However, part of the related discussion was included.

Figure 3.09

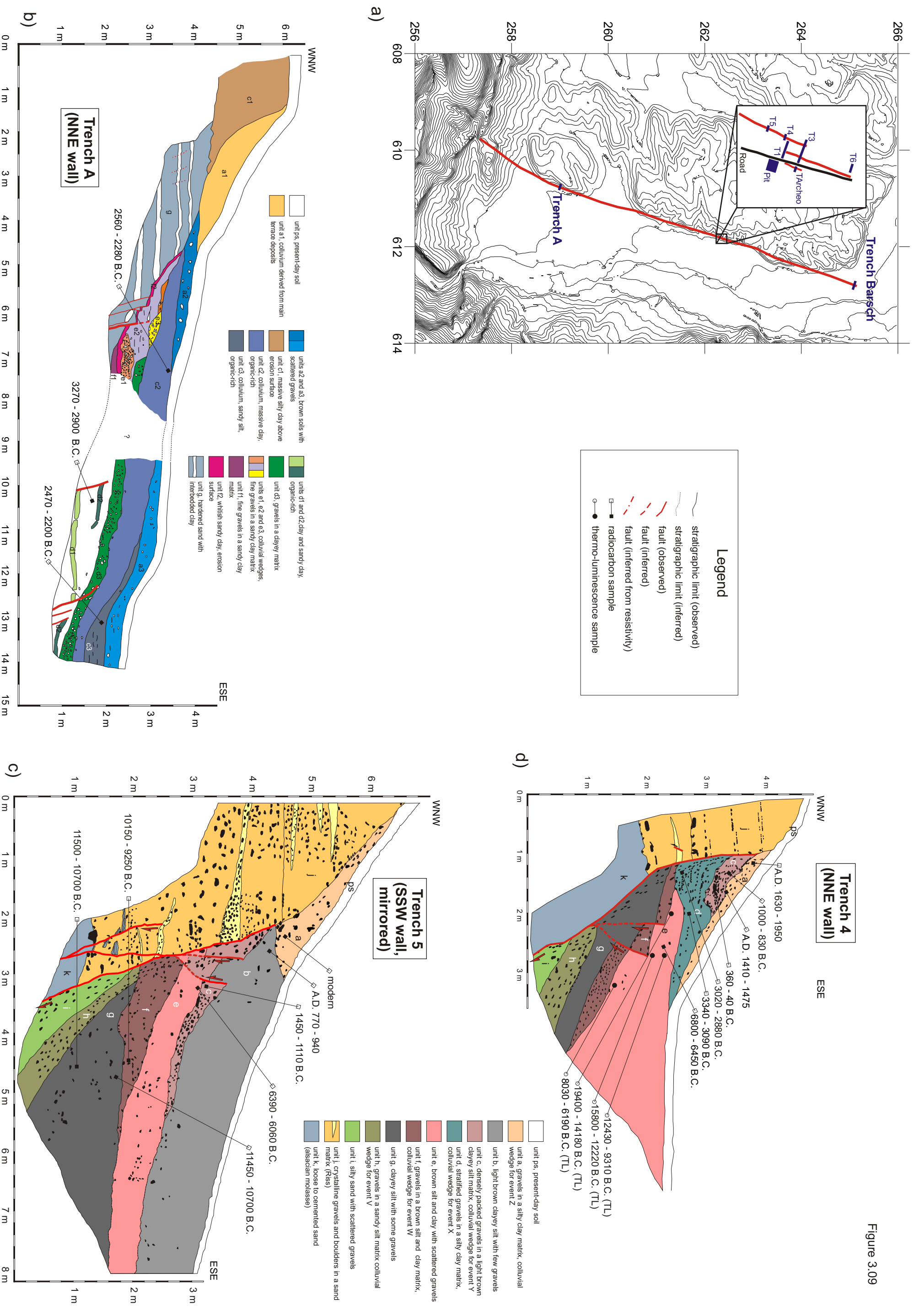
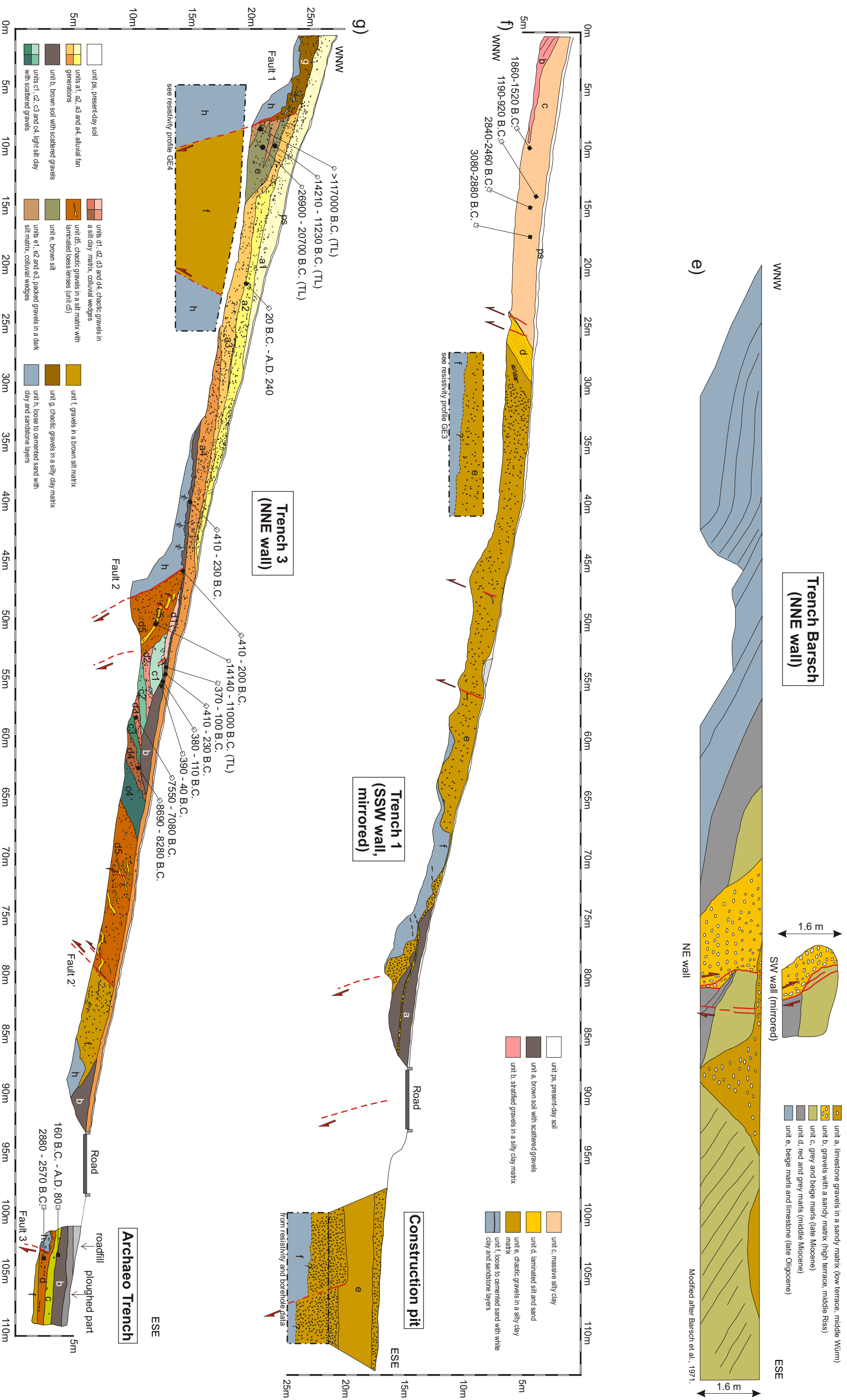


Figure 3.09 (continued)



Chapter 4

Ground-penetrating radar investigations along the North Anatolian fault near Izmit (Turkey): Constraints on the right-lateral movement and slip history

*Ferry, M., Meghraoui, M., Girard, J.-F., Rockwell, T.K., Kozaci, Ö.,
Akyuz, S. and Barka, A.*

(*Geology*, 2004, Volume 32/1, pp. 85-88)

Abstract

We analyze ground-penetrating radar (GPR) profiles made across and parallel to the August 1999 earthquake ruptures of the North Anatolian fault. The profiles document cumulative right-lateral offset of stream channels and the successive faulting of a medieval (Ottoman) canal. The dominance of fine sand to coarse gravel in the sections imaged allows for reasonably deep penetration, and processed radar signals clearly image visible reflectors within the uppermost 5 m. Near Köseköy, buried fluvial-channel deposits, exposed in some trenches dug to determine paleoseismicity, are also visible on profiles and show a maximum 6.7–7.4 m of lateral displacement. Younger channel units display 4.5–4.9 m of right-lateral displacement at 2–3 m depth and show that the penultimate rupture along the Izmit segment produced a similar amount of displacement as in 1999. At the Ottoman canal site, GPR profiles complement a trench study and provide consistent results showing the occurrence of three faulting events after A.D. 1591, the date of canal construction. This study demonstrates that the use of GPR method in paleoseismology contributes to better identify cumulative slip along active faults.

Introduction

Study of surface ruptures associated with the 1999 earthquake sequence along the North Anatolian fault contribute key observations for the understanding of major continental seismogenic faults. In addition, the correlation between coseismic and cumulative movements is critical for field investigations on past seismic events through geomorphological and paleoseismic studies. Surface ruptures associated with the $M_w = 7.4$, August 1999 Izmit earthquake were mapped over 115 km length and exhibited 2–5 m of right-lateral displacement along four distinct segments (Fig. 4.1; Barka et al., 2002). The segmentation pattern and related seismic deformation appear to be persistent, as attested to by the well-documented historical seismicity (Ambraseys and Finkel, 1995) and by paleoseismic investigations (Rockwell et al., 2001, 2002). Therefore, the geomorphology and distribution of Holocene deposits along the coseismic ruptures should provide good conditions to better constrain the long-term faulting behavior.

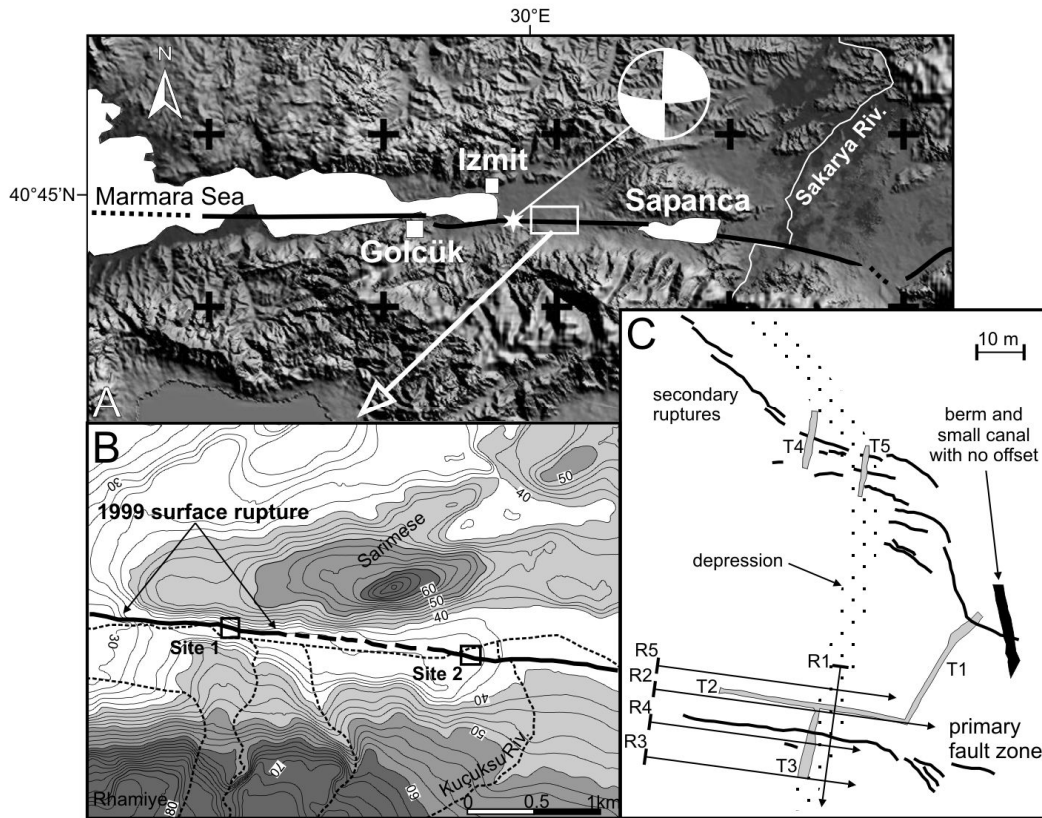


Figure 1. A: August 1999 Izmit earthquake area and related surface rupture with main segments. Focal mechanism is from Harvard CMT (Centroid Moment Tensor) solution. B: Topographic map of study area east of Izmit. Thick lines are surface ruptures; dashed lines are drainages. C: Location map of 1999 surface ruptures and GPR profiles at site 1 (Köseköy). R1 to R5 are GPR profiles, T1 to T5 are trenches (Rockwell et al., 2001). Note trend of stream and related alluvial deposits (dot-filled area) across main fault.

Although the 1999 earthquake sequence allowed collection of a wealth of data on the fault zone, the relationships between this surface rupture and past ruptures remain among the major problems to be solved by paleoseismic investigations. In this context, trenching operations require considerable field work and are generally limited to 3–4 m depth. The use of subsurface geophysics and, in particular, GPR (ground-penetrating radar) profiles, complements trenching studies and may provide a detailed picture, down to 10 m in depth, of the successive faulting episodes and their relationship to the surrounding sedimentary environment.

In this paper, we describe GPR profiles acquired at two selected sites along the surface ruptures produced by the $M_w = 7.4$ 1999 Izmit earthquake (Fig. 4.1B). They show clear images of the near-surface fault geometry and its complex structure as well as evidence of cumulative right-lateral and vertical movements. The individual and cumulative

offset combined with trench results document the slip history and illustrate that geophysical studies of the shallow expression of faulting are a valuable tool to characterize the faulting parameters for past events (geometry and displacement).

GPR Method And Site Selection

Ideally, GPR may provide high-resolution (down to 0.1) images of the subsurface over a depth range of several meters to exceptionally 50 m. However, the quality of the data and the depth of penetration strongly depend on the dielectric properties of the investigated material and the frequency range of the antennae used (Davis and Annan, 1989). Indeed, the best results have been obtained for stratified, clay-free, dry or freshwater-saturated sand or gravel (Smith and Jol, 1995).

For this study, our main objective was to test the applicability of GPR imaging across very recent surface ruptures, as well as to determine its capacity to complement paleoseismic investigations. We used a Sensors and Software PulsEKKO IV GPR unit equipped with two 100 MHz unshielded antennae to ensure a vertical resolution ranging from 0.3 m to 0.5 m. The pulse voltage was set to 400 V, and we acquired traces over total time windows of 512 ns to 640 ns. The antennae separation was set to 1 m and the step size to 0.2 m to avoid aliasing. Standard processing included automatic shift of first arrivals, dewow correction, envelope amplification, and band-pass frequency filtering. A ringing phenomenon (Nobes, 1999) was persistent over the whole data set. After an initial interpretation stage, we filtered horizontal reflections to obtain improved sections. Dipping reflectors are enhanced, and channels appear more clearly, whereas horizontal geologic reflectors are most often degraded. Our interpretations combine elements from both filtered and unfiltered sections.

In order to identify fault-related structures, several features attributed to lithologic changes, deformation, or discontinuities were investigated. Among the criteria we found to be useful are (1) a group of reflectors that end abruptly along a line, (2) a change from one radar facies to another, (3) a change in the dip of a reflector, (4) a strong diffraction hyperbola, and (5) a change in the frequency and/or amplitude of the radar signal. We describe each of these phenomena as they are applied in this study to the interpretation of earthquake history and in assessing lateral slip on buried channels.

Profile Analyses

Köseköy Site

The Köseköy site is located in an area of complex surface rupture (Fig. 4.1B). The primary fault zone (Fig. 4.1-C), which sustained a little over 2 m of right-lateral slip at this site

in 1999, exhibits a clear E-W trending and south facing fault scarp with a vertical throw of 0.5 – 0.6 m. Oblique to it, a secondary rupture zone of discontinuous strands extends tens of meters to the northwest. An ~0.2-m-deep elongated depression, most likely left by a recently active channel, extends from the base of an east-west oriented ridge located at the northern side of the site down to the stream, located ~20 m south of the primary fault zone. We surveyed five GPR profiles for a total length of 340 m at the Köseköy site. Here we present an excerpt of profile R1 surveyed across the main fault scarp as well as profiles R2, R3, R4, and R5 surveyed parallel to the main 1999 rupture and across the recent channel to image older buried channels and their relationship to the fault.

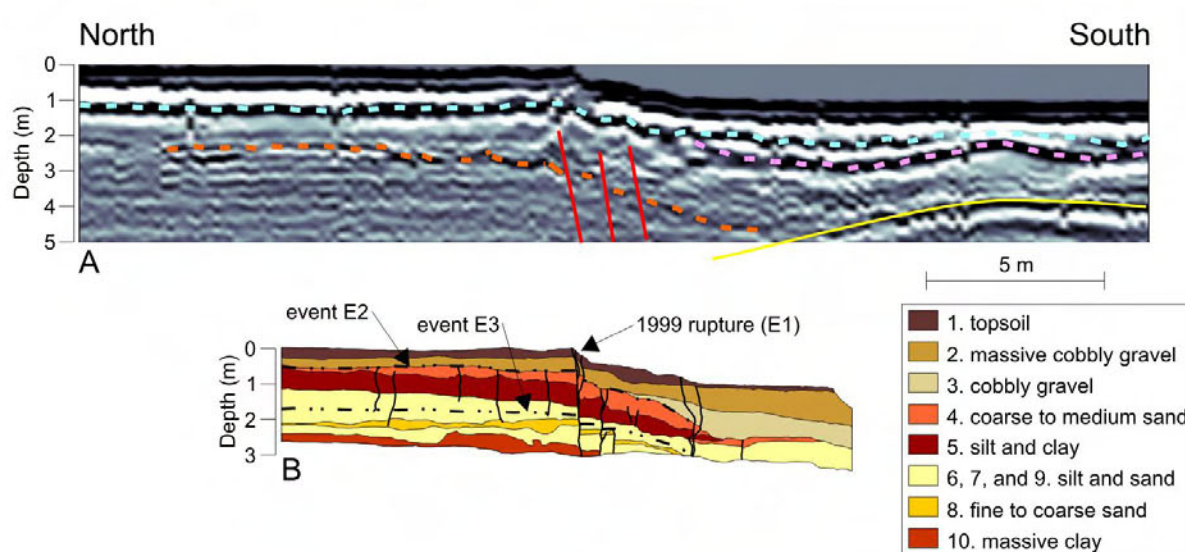


Figure 2. A: Subset of GPR profile R1 across main 1999 surface rupture. Time-depth conversion was applied with a velocity of 0.09 m/ns on the basis of CMP measurements surveyed along R5. Colored lines outline main reflectors described in text. Thick red lines indicate inferred faults. Because of a diffraction hyperbola induced by a nearby tree (yellow line), it is not possible to determine whether lower reflector also forms a basin. B: Simplified log of trench 3. Units are numbered according to Rockwell et al. (2001). Black dashed lines indicate event horizons associated with events E2 and E3. Main dielectric contrasts are provided by occurrence of clayey units (namely, units 5 and 10) below cobbly or sandy units (namely, units 4 and 9).

Profile R1 displays three clear reflectors: (1) at ~1 m depth, a strong flat reflector (blue line in Fig. 4.2A) broken and vertically displaced where it crosses the 1999 rupture; (2) south of the fault, an arcuate reflector (pink line) that outlines a 12-m-wide and ~0.5-m-deep basin capped by the blue reflector; and (3) at ~2 m depth, a weaker reflector (orange line) broken and vertically offset by the fault before it dips to the south deeper than the penetration

depth. The blue and orange reflectors are not parallel, thus suggesting a greater amount of deformation for the lower reflector.

Parallel to R1 and very close to it, we opened trench T3, the simplified log of which is presented in Figure 4.2B (Rockwell et al., 2001). The exposed section is mainly composed of cobbles, sand, silt, and clay with strong lithologic contrasts that may provide adequate dielectric contrasts for GPR imaging. Indeed, various field experiments indicate that strong reflectivity is driven by conductivity and permittivity contrasts (Davis and Annan, 1989). At 0.6–1 m depth, the contact between unit 2 and unit 4 corresponds to the blue reflector in terms of depth and geometry. Similarly, south of the fault, the base of unit 3 corresponds to the pink reflector. Finally, at ~2.3 m depth the top of unit 10 is overlain by sand and probably corresponds to the orange reflector. On the basis of paleoseismic investigations, Rockwell et al. (2001) have shown that the contact between units 4 and 5 has sustained two major surface ruptures (E1 and E2), whereas the contact between units 7 and 8 has sustained three ruptures (E1, E2, and E3), including that from the 1999 earthquake.

The channel structures observed in GPR profiles R5 and R2 present similar shapes as the youngest channel feature in trench T2 (Fig. 4.1-C). Hence, we could recognize in profiles R5 and R2 several channel features, four of which provide clear signatures. At ~1.2 m depth, two ~0.5-m-deep channels (highlighted in purple and green in Fig. 3A) correspond to the blue reflector identified on R1 and may be associated with the top of unit 5. At ~2.5 m depth, the orange channel corresponds to the orange reflector identified on R1 (i.e. to the top of unit 10). The red channel was exposed in fault-parallel trench T2 but it was flooded before any detailed description. Profiles R4 and R3 exhibit features similar to what is observed on R5 and R2, especially the four previously described channel structures.

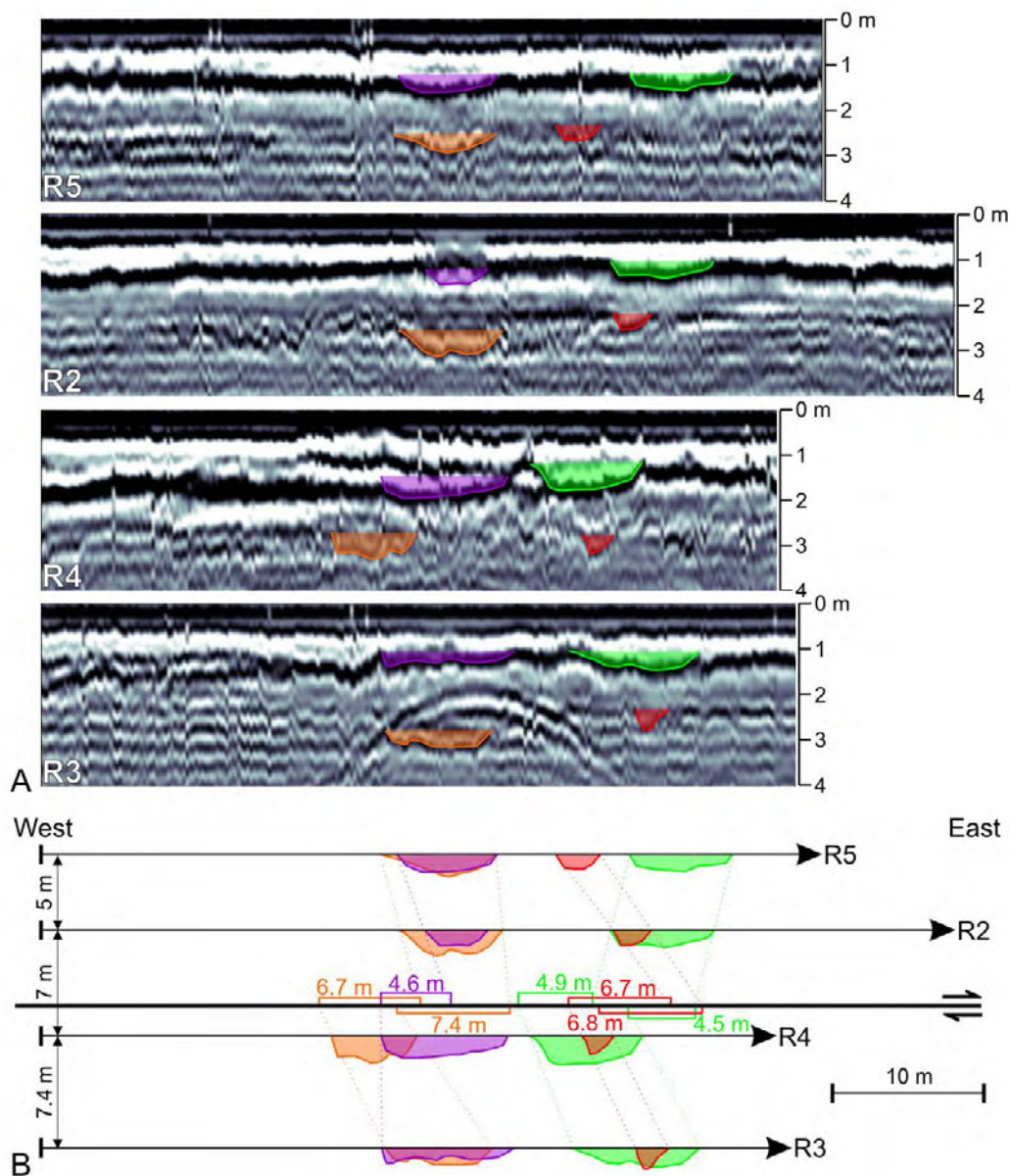


Figure 3. A: Parallel GPR profiles R5, R2, R4, and R3 collected along main 1999 surface rupture at site 1. Four channels (highlighted in different colors) may be consistently identified on all sections. Depth are given in meters (with respect to top of each profile). B: Map of occurrence of channels with respect to fault (thick black line with arrows). Channel edges are projected onto fault plane to indicate their horizontal cumulative displacement.

The four channels could not be equally imaged in GPR profiles due to attenuation variations of the signal, aerial diffractions, penetration depth and persistent ringing. However, channels can be identified through their shape (edges and apex) and dielectric contrasts between channel deposits and related substratum. In profiles, the purple channel is best

characterized by its western edge whereas the three other channels may be characterized by both edges.

For each channel, we assumed a simple, linear drainage pattern on each side of the fault, with the inferred deflection being the result of coseismic slip. First, specific features were identified and linked between profiles R5 and R2 and between profiles R3 and R4. Then, we projected the inferred position of each of the channels to the fault. The difference in intersection (piercing) points between corresponding features yields the inferred horizontal offset. As shown in Figure 4.3B, the upper channels (purple and green) are consistently deflected 4.5–4.9 m in a right-lateral sense, approximately twice the amount of strike-slip observed in 1999. From the paleoseismic analysis, these channels are embedded within that part of the stratigraphic section that has been subjected to only two surface ruptures (Rockwell et al., 2001). Thus, we interpret that the penultimate earthquake along the Izmit segment resulted in a similar amount of slip as in 1999.

Similarly, the lower channels (orange and red) are deflected by 6.7–7.4 m when projected across the main fault. These lower channels are interpreted to have been subjected to three surface ruptures. From this analysis, we infer that event E3 identified in trenches (Rockwell et al., 2001) also was associated with ~2–2.5 m of lateral slip, similar to that in 1999. These observations suggest that the Izmit segment may have produced characteristic slip, at least for the past three events.

The A.D. 1591 Ottoman Canal Site

After an initially Roman effort, construction during the Ottoman regime led to the incomplete construction of a 17-km-long canal between the Izmit Bay and the Sakarya River in early A.D. 1591 (Finkel and Barka, 1997). We analyzed aerial photographs and identified two segments of the canal, one of which parallels the modern canal as it passes south of Sarimese. They inferred a maximum width of 40 m and a maximum depth of 20 m. As the canal was dug in alluvial sediments and later filled with stratified sandy to clayey deposits, the bottom surface should provide a noticeable dielectric contrast adequate for GPR imaging and a valuable time mark for paleoseismic investigations.

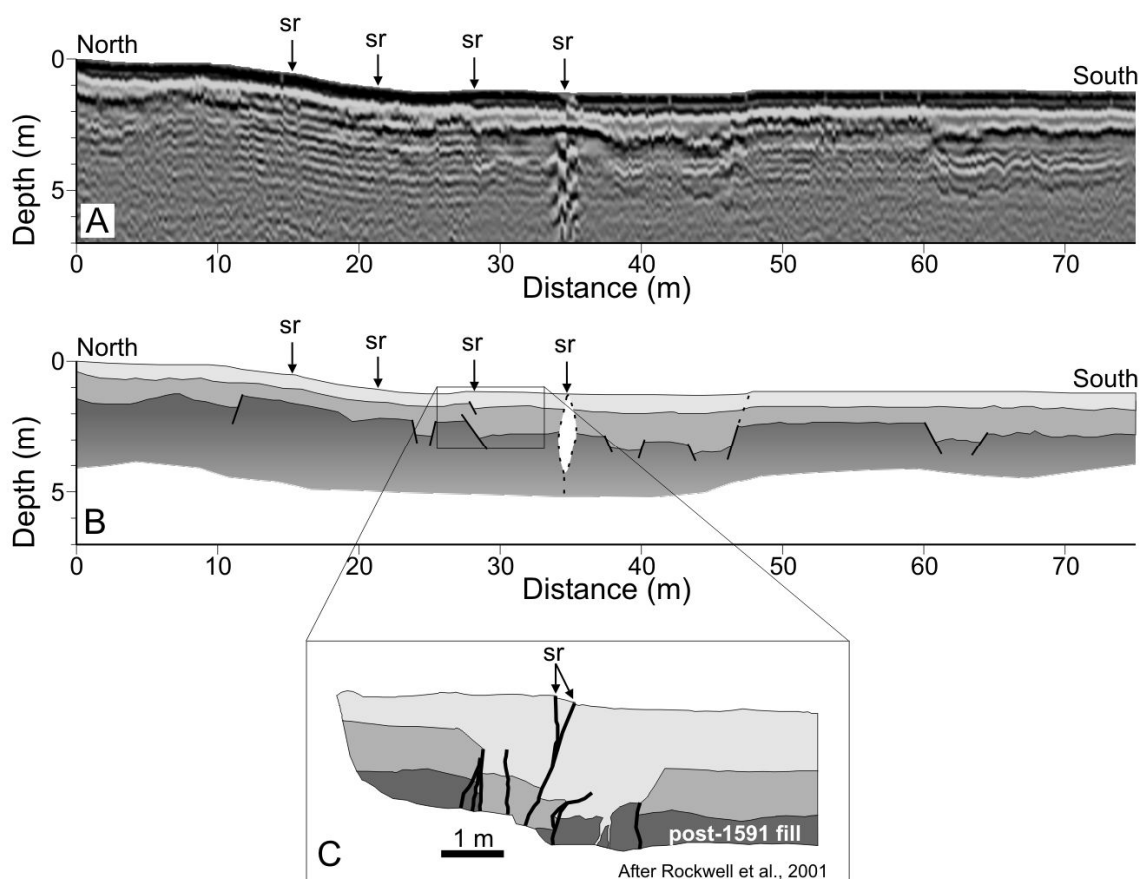


Figure 4. A: GPR profile across former Ottoman canal at site 2 with a nominal frequency of 100 MHz. B: Interpreted section with surface observations; sr—surface rupture. Unusual lozenge-shaped anomaly at station 34 m probably marks presence of an open crack produced by 1999 rupture. C: Simplified log of a trench dug parallel to GPR profile (Rockwell et al., 2001).

At this site, GPR profile C1 (Fig. 4.4A) was surveyed across the former Ottoman canal where Barka et al. (2002) mapped the 1999 surface ruptures. Close to the surface, a strong reflector (bottom of the light gray unit in Fig. 4.4B) can be continuously followed along the profile. It may scarcely be distinguished from the direct or first arrival, except between stations 28 m and 48 m. Another prominent reflector (bottom of the medium gray unit in Fig. 4B) starts close to the surface at the top of the canal berm (station 5 m) and deepens into the canal at a steeper angle than the topography along the slope, perhaps representing the original canal slope. It is broken and vertically displaced by a series of subvertical faults (thick lines in Fig. 4B). This reflector separates a low-frequency homogeneous radar facies from a zone affected by a severe ringing effect, presumably very clayey. We interpret all of the horizontal geologic reflectors within the canal as imaging part of the post-A.D. 1591 fill

derived by flooding from the Kuçuksu River, located less than a couple hundred meters from our trench and GPR profile.

The base of the medium gray unit is broken and vertically displaced by up to 1 m by strike-slip faults, many of which also broke in 1999. These faults form two small depressions between stations 28 m and 48 m and south of station 60 m. In the northern depression, between stations 27 m and 33 m, Rockwell et al. (2001) excavated a 2.5-m-deep trench that exposed faulted stratified fluvial and canal fill deposits, all of them younger than A.D. 1591 (see Fig. 4.4C). They interpreted three displacement events recorded in the canal-fill alluvium.

There are two major contributions of the GPR profiles to understanding the geologic context of the Ottoman canal paleoseismic site. First, the primary fault is well imaged as a reflection to at least 6 m depth and is expressed as a vertical zone of disruption. Second, a much broader fault zone is interpreted from the GPR data, with additional faults present that did not break in 1999. It is important to note that although we achieved decent penetration, we are nearly certain that we did not image the entire depth of fill in the canal, which is expected to exceed 10 m in this area.

Furthermore, the trench was emplaced across the primary surface break. From the GPR profile, it appears that other faults with dip separation are present, and it would have been useful to have exposed them during the trenching phase. In that the GPR data were not processed in the field, we were not aware of these buried faults at the time of the trenching. In hindsight, it is important to have the preliminary geophysical data interpreted prior to opening trenches, as we would probably have acquired a better record and improved our confidence in event E2.

Discussion And Conclusions

Ground-penetrating radar investigations were conducted at two sites along the 1999 Izmit earthquake surface rupture and provide complementary information to paleoseismic trenching. Our field surveys consisted of a single frequency of 100 MHz that appears to be a good compromise between resolution and penetration depth. Obviously, some specific parts of the profiles need enhancement of the resolution to image displacements with a greater accuracy. Furthermore, extending the penetration depth would be useful to image deformation from older events and to estimate the amount of cumulative slip over a longer time range.

We also find that considerable uncertainty remains as we only ran two GPR lines on each side of the fault for lateral control. However, paleoearthquakes E2 and E3 display right-lateral displacements with average amounts similar to the 1999 slip. In future studies, we suggest either a full three-dimensional GPR survey or, at the least, a sufficient number of

two-dimensional lines to characterize the subsurface geometry of buried channels. Additional fault-parallel lines at Köseköy could serve to reduce the uncertainty in slip on these buried channels and further test slip repeatability.

Finally, complete GPR survey of a site prior to paleoseismic excavations may lead to better trench siting in general, as well as the targeting of specific buried features. In particular, identification of subsurface linear features that cross fault traces is critically important in the interpretation of past strike-slip events and their magnitudes of slip, as trenches typically sample the geology perpendicular to the direction of slip. Thus, GPR may provide slip in lieu of extensive three-dimensional trenching, which is both costly and time consuming.

Acknowledgments

This work is presented here in the memory of Aykut Barka, who facilitated major advances in the understanding of the neotectonic framework of Turkey. Without his enthusiasm and guidance, none of us would have ended up working in Turkey and coming to love its land and people. We thank Maksim Bano for lending the PulseEKKO IV (GPR) equipment. This research was supported by the Swiss Seismological Service (Ferry), the CNRS-INSU/ACI-Turquie and ACI-Catastrophes Naturelles (Meghraoui), and by the Southern California Earthquake Center (SCEC) and Pacific Gas and Electric Company (Rockwell). SCEC is funded by NSF Cooperative Agreement EAR-0106924 and USGS Cooperative Agreement 02HQAG0008. This is publication 1315 of the Institute of Geophysics, Eidgenössische Technische Hochschule, Zürich, 010XX of the Institut de Physique du Globe, Strasbourg, and SCEC contribution number 744.

Chapter 5

Paleoearthquake History of the western portion of the North Anatolian Fault in Western Turkey from paleoseismic data, and implications to the seismic hazard of Istanbul

*Rockwell, T.K., Seitz, G., Langridge, R., Barka, A., Aksoy, E., Uçarkus, G., Akbalik,
B., Satir, D., Meltzner, A., Ragona, D., Klinger, Y., Meghraoui, M. and Ferry, M.*

(Submitted to Bull. Seism. Soc. Am., 2004)

5.1 Abstract

We excavated 26 trenches across the 1912 rupture of the Ganos strand west of the Marmara Sea to resolve slip and constrained the earthquake history on a channel-fan complex that crosses the fault at a high angle. A distinctive well-sorted fine sand channel that served as a marker unit was exposed in 21 trenches totaling over 300m in length. Isopach mapping shows that the sand is channelized north of the fault, and flowed as a fan complex across a broad fault scarp to the south. Realignment of the feeder channel thalweg to the fan apex required about 9 ± 1 m of reconstruction. Study of the rupture history in several exposures demonstrates that this displacement occurred as two large events. The age of the sand channel is radiocarbon dated as post-1600 A.D., so we attribute the two surface ruptures to the large regional earthquakes of 1766 and 1912. If each was similar in size, then about 4-5 m of slip can be attributed to each event.

We also excavated six trenches at two sites along the 1999 Izmit rupture to study the past earthquake history along that segment of the North Anatolian fault. One site, located in the township of Köseköy east of Izmit, revealed evidence for three surface ruptures during the past 400 years. The other trench was sited in an Ottoman canal that was excavated (but never completed) in 1591. There is evidence of at least two and possibly three large surface rupturing events in the upper 2 m of alluvial fill within the canal at that site, located only a few kilometers from the Köseköy site. One of the past events is almost certainly the large earthquake of 1719, for which historical descriptions of damage are almost identical to that of 1999. Other earthquakes that could plausibly be attributed to the other recognized rupture of the Izmit segment are either the 1894, 1878, or possibly the 1754 events, all of which produced damage in the region and for which the source faults are poorly known. Our paleoseismic observations suggest that the Izmit segment of the North Anatolia fault ruptures every one and a half centuries or so, consistent with the historical record for the region

Release of about 4m of seismic slip both west and east of the Marmara Sea this past century (1912, 1999) support the contention that Istanbul is at high risk from a pending large earthquake. In that historical records suggest that the last large central Marmara Sea event occurred in 1766, there may be a similar 4m of accumulated strain across the Marmara basin segment of the North Anatolian fault.

5.2 Introduction

Information on the size and timing of past earthquakes is important in understanding fault behavior, a key element in forecasting future seismic activity (Sieh, 1996). The North Anatolian fault (NAF) in Turkey (Barka, 1992) (Fig. 5.1a) is an ideal candidate for understanding fault behavior over multiple earthquake cycles because there is a long and excellent historical record of large earthquakes going back over 2000 years (Ambraseys and Finkel, 1987, 1991, 1995) (Fig. 5.2). Furthermore, Like the San Andreas fault of southern California, it is a fast-moving fault (~23 mm/yr, Straub and Kahle, 1995; Straub, 1996; Reilinger et al., 1997) resulting in many earthquakes for each fault segment during this long historical period. It is also fairly segmented, and most of the fault zone has ruptured this past century. Thus, there is the opportunity to collect information on the patterns of large earthquake generation over many earthquake cycles, as well as their sizes and repeatability. In this paper, we present new results that further quantify the earthquake history of the North Anatolian fault both east and west of the Marmara Sea.

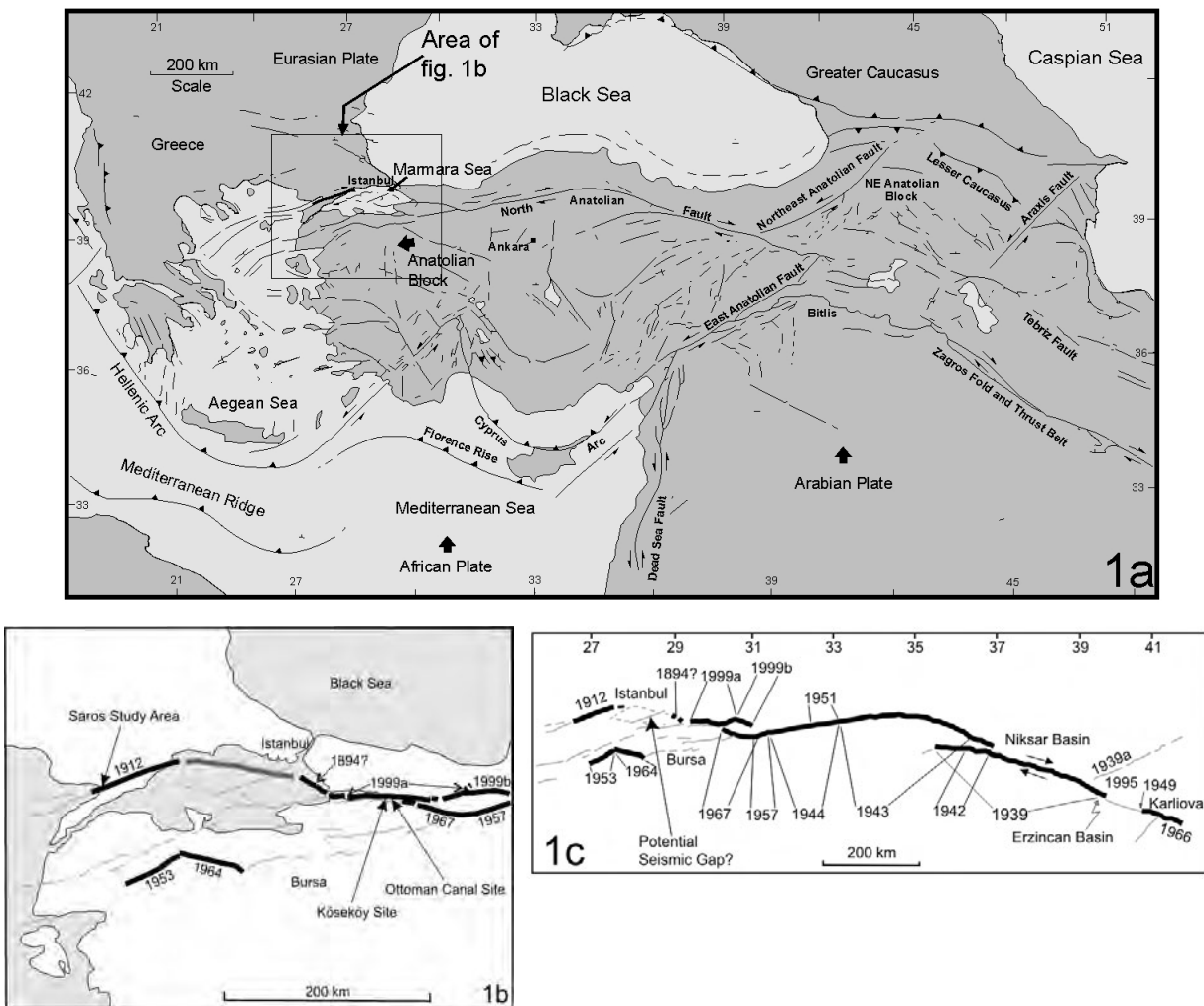


Figure 5.1: A) General tectonic map of the Anatolian block and surrounding regions. The Ganos fault (thick black line) is the continuation of the North Anatolian fault west of the Marmara Sea. B) Close-up over the Marmara Sea region displaying recent rupture and study areas. C) Westward migration of fault activity along the North Anatolian fault during the 20th century with pertaining potential seismic gap located within the Marmara Sea.

To the west near the Gulf of Saros, we continued paleoseismic investigations and resolved slip for the past two large earthquakes that struck the Gallipoli region in 1766 and 1912. The Saros study area lies within the township of Kavakköy (Fig. 5.1b and 5.2) close to where we completed earlier studies (Rockwell et al., 2001). We had determined that four surface ruptures have occurred near where the fault passes offshore into the Gulf of Saros during the past 1100 years or so. However, the dating was insufficiently precise to confidently resolve which of the historical events these were. In this new study, we focused on a young (post-1600 A.D.) stream channel that crosses the fault at a high angle and is offset by the fault across a narrow zone. Twenty-two trenches were excavated at this new site to resolve total slip on the channel and to further constrain the timing of ruptures that produced the slip.

East of the Marmara Sea, we continued efforts between Izmit and Lake Sapanca that we had begun prior to the August 1999 Izmit earthquake. Specifically, we excavated new trenches within and adjacent to an Ottoman canal, dated at ca 1591 from historical data (Finkel and Barka, 1999; C. Finkel, personal communication) to resolve the history of surface ruptures for the past 400 years east of Izmit Bay.

Each of these studies bear on the impending seismic hazard to Istanbul, which lies close to the NAF beneath the Marmara Sea. Our observations support the contention that the NAF near Istanbul should be close to failure based on the distribution and size of earthquakes during the past 400 years, and that the recent earthquakes to the east (Izmit and Düzce events in 1999) have further loaded the fault segments beneath the Marmara Sea (Parsons et al., 2000).

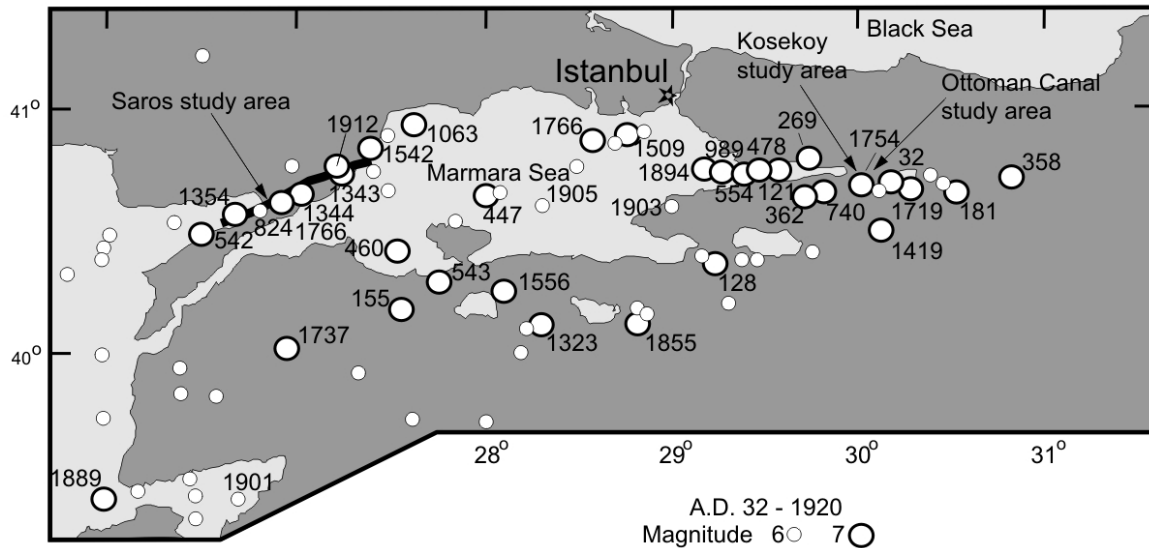


Figure 5.2: Strong earthquakes in the Marmara Sea region for the last two millennia. Reference earthquakes are the 1912 event west of the Marmara Sea and the 1999 event east of it. The 1766 and 1509 earthquakes are best candidates to bridge rupture from both sides of the sea.

5.3 The Saros Site

Earlier paleoseismic results at Kavakköy in the Gallipoli Peninsular region near the Gulf of Saros indicate that four earthquakes have ruptured the surface in that area during the past 1000-1200 years, and that two of these post-date a sand channel dated to younger than the fourteenth century. One of these is almost certainly the surface rupture of the 1912 M7.4 earthquake, which was photographed east of our site towards the Marmara side of the peninsula (Ambraseys and Finkel, 1987a).

We analyzed low altitude stereo photography of the fault along the westernmost few kilometers before it passes offshore into the Gulf (Fig. 5.3), to search for the best sites to resolve slip. In the area of T-1 from the Rockwell et al. (2001) study, we recognized the presence of an abandoned tributary channel to the Kavak River that crosses the fault at a high angle, and is the likely source for the sand exposed in our original T-1 trench. At the fault, sediments in the abandoned channel appear in the aerial photography to splay out southward across the fault, indicating that a low scarp is present where the fault crosses the channel. We hoped to expose buried elements of the channel system and resolve slip on buried piercing points, to better constrain the age of these channel deposits, and to further resolve the number of earthquakes that affect the buried sand channel sediments. Towards this aim, we focused our efforts on the margins of the channel and excavated a total of 26

trenches across and parallel to the fault (Fig. 5.3). The central part of the channel is now occupied by an elevated highway and berm and was no longer available for study.

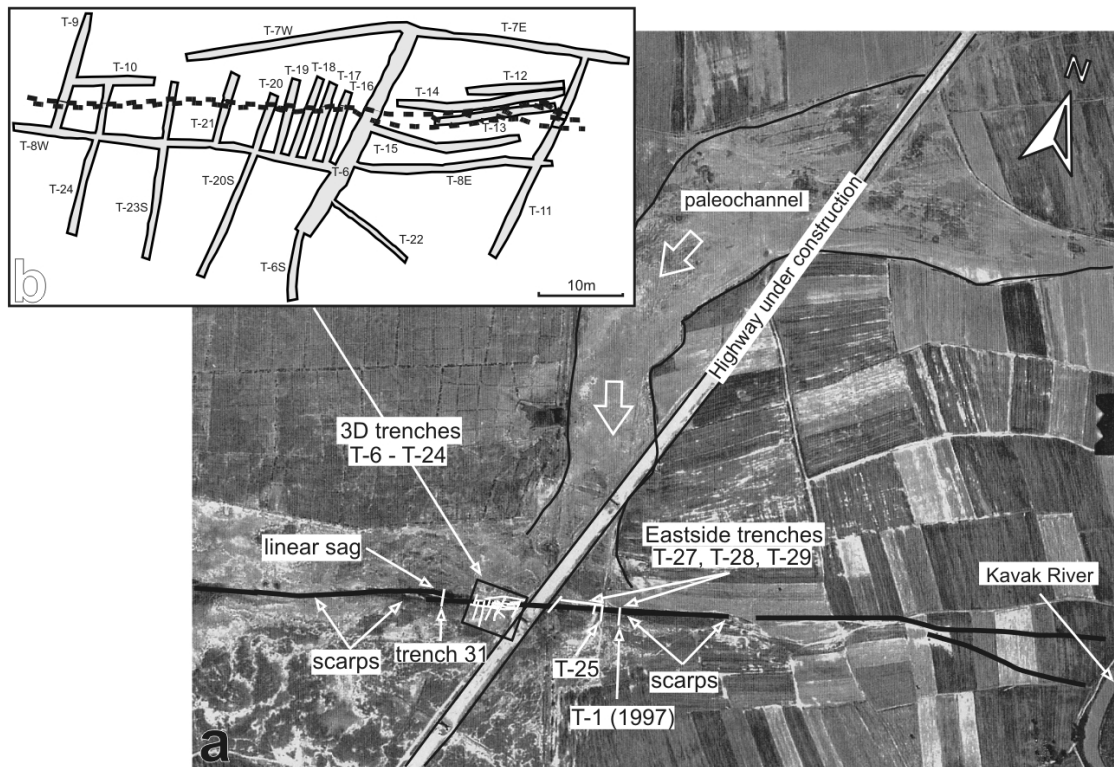


Figure 5.3: A) Aerial photograph of the Saros site at the western tip of the Ganos fault (thick black line). The fault crosses and affects a recent paleochannel at an ideally steep incidence angle. A dense grid of 3D trenches unveiled recent lateral offset affecting the youngest parts of the channel. B) Close-up view of the 3D trench site showing trench layout with respect to fault strands. This is the place of our bigger effort.

Several of the trenches that contained important information on past surface ruptures were logged in detail on photographs and later entered into the computer in rectified form. Many of the trenches, however, were excavated for the sole purpose of tracing out the distribution of the distinctive well-sorted sand body, and data from these trenches was collected on the thickness of the sand but they were not logged in detail. All trench locations, including sand thickness control points, were surveyed with a Wild TC-2000 total station, and all have the same reference elevations established by surveyed horizontal string lines. Further, all critical contacts, relevant stratigraphic pinch outs, etc. were surveyed to precisely locate them in 3D space.

5.3.1 Site Stratigraphy

All of the trenches exposed a similar succession of young sediments, with or without a distinctive clean, well-sorted channelized sand. Fig. 5.4 is a detailed log of the east face of trench T-6, and shows the typical stratigraphy of the site, with unit 200 being the distinctive sand that is only exposed on the south side of the fault in this trench. This sand is the same as unit 3 described in trench T-1 by Rockwell et al. (2001), and was also exposed in new trenches near the original T-1 on the east side of the highway (Fig. 5.5 and 5.6). We use the lateral extent of this distinctive sand to constrain cumulative slip on the most recent surface ruptures. In this section, we briefly describe each of the primary units and the associated radiometric control on their ages.

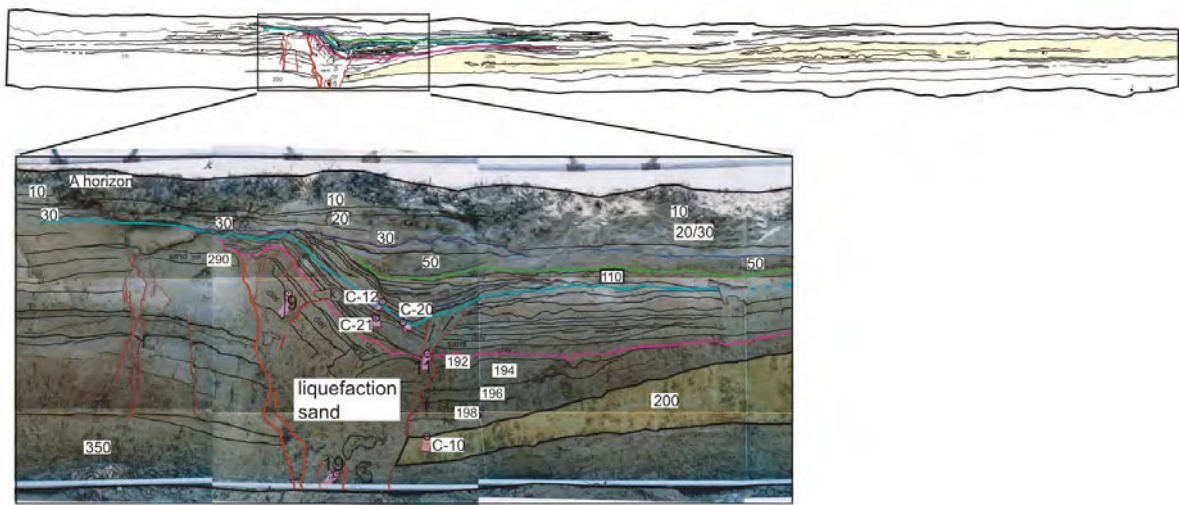


Figure 5.4: Detailed log of trench T-6 established on the basis of trench observations. Color photographs were shot in the field and developed overnight. Paper prints were then assembled manually and covered with transparent plastic where log was reported. Outlined unit 200 (pale yellow layer on log and slightly lighter lay on photograph served as a reference layer surveyed in the different trenches.

We identified several primary units, along with dozens of secondary contacts, within the section exposed in the trenches. Units are given numeric designations ranging from 10 (topsoil; youngest) to 350 (oldest). Within a given trench, correlation of units both laterally along the trench and from wall to wall is fairly certain, and is based on the character of several distinctive strata contained within the section. Conversely, unit designations in the upper section of T-6 may be generally similar to those in the trenches east of the highway, but their correlation is by inference because we did not connect trenches between these

sites (because of the highway). Thus, unit 100 at T-6 may not be exactly the same stratum as unit 100 in the East Saros trenches, although it is similar and falls in the same part of the section. The only unit for which we feel confident to be the same in all exposures is the distinctive well-sorted sand of unit 200. Even this unit, however, may have some variance in age across the overall study area (few decades or less?) as the sand in the eastern group of trenches was associated with the main channel deposits whereas the sand at T-6 was deposited by a secondary tributary overflow channel, as discussed later.

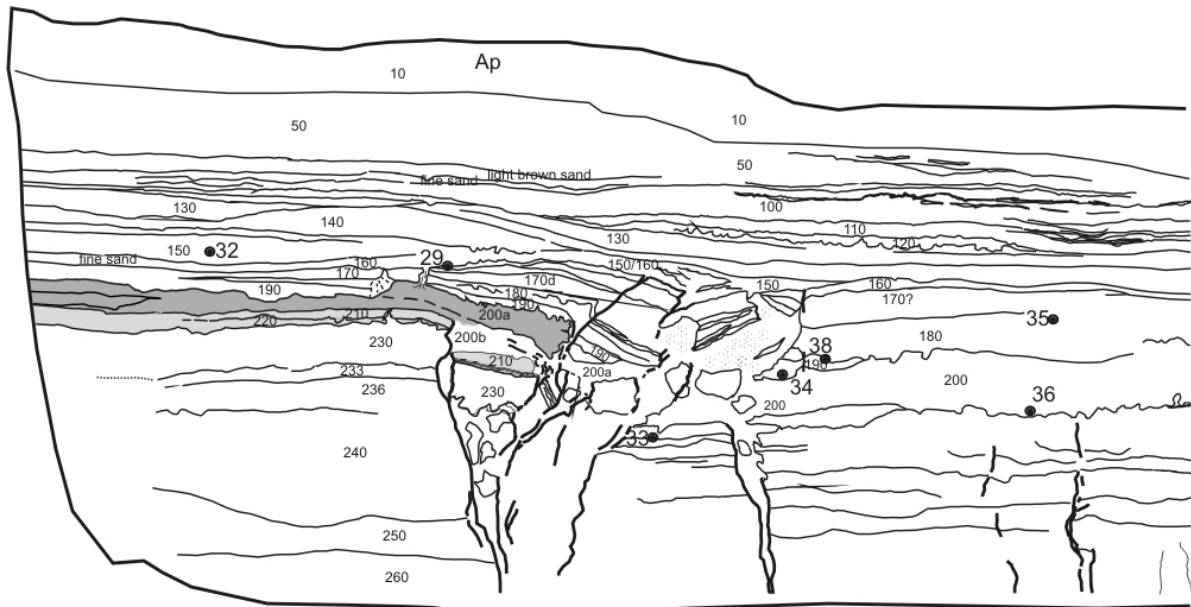


Figure 5.5: Detail of trench T-1's log centered on the fault zone and showing relationships between recent deposition and faulting events. The present figure is similar to Figure 6 which is not reproduced here.

The deepest (oldest) stratum, unit 350, was exposed at a depth of about 1.5 m on the north side of the fault in T-6, just above the water table. Units 210 through 350 are generally fine-grained silt and clay strata interpreted as a succession of over-bank deposits to the main Kavak River. The only age control for this part of the section is from two dates on a sample split (T6-6) from near the base of this section that yielded consistent calibrated ages of about 1-2 centuries BC. As this sample could have been re-worked or have been resident in the system for some period of time, this represents a maximum age for this part of the section.

Unit 200 is the distinctive well-sorted sand that we use to constrain lateral slip, and is therefore of considerable interest. The sand is channelized and its distribution is locally restricted or absent. In our analysis of the aerial photography (Fig. 5.3), we interpret a

tributary or overflow channel to the Kavak River as the primary source for this sand. Within this tributary system, we exposed the sand in most of the trenches and can make some general observations about its extent.

East of the highway, the sand fills a major, broad channel, and the sand is locally over a meter thick. We excavated a trench parallel to the fault between T25 and the highway, and the sand locally extended to below the depth of the 2-m-deep trench. This was an exploratory trench to determine the character of the sand and was not logged in detail because of safety constraints. Nevertheless, it was clear to us that the primary fluvial channel lies east of the highway, and our trench 25 lies near the margin of this system. Trench T-1 of Rockwell et al. (2001), which lies within 10 m to the east of T25, also exposed this sand unit (unit 3 in their trench log).

West of the highway, unit 200 is substantially more restricted in its aerial extent. North of the fault, the well-sorted sand is restricted to a narrow and shallow (<20 cm) “feeder” channel that flowed from north to south across the fault. South of the fault, the sand thickens dramatically and locally reaches over 40 cm in thickness. We collected observations on the sand thickness in all exposures to provide a basis for developing an isopach map of the sand (Fig. 5.7). We collected these observations at a maximum spacing of 50 cm and tied all measurements to a common, surveyed system of horizontal string lines. We also measured the absolute height of the top and bottom of the sand relative to the string datum to provide a complete spatial reference. These data are presented later to resolve slip on the channel fill of unit 200.

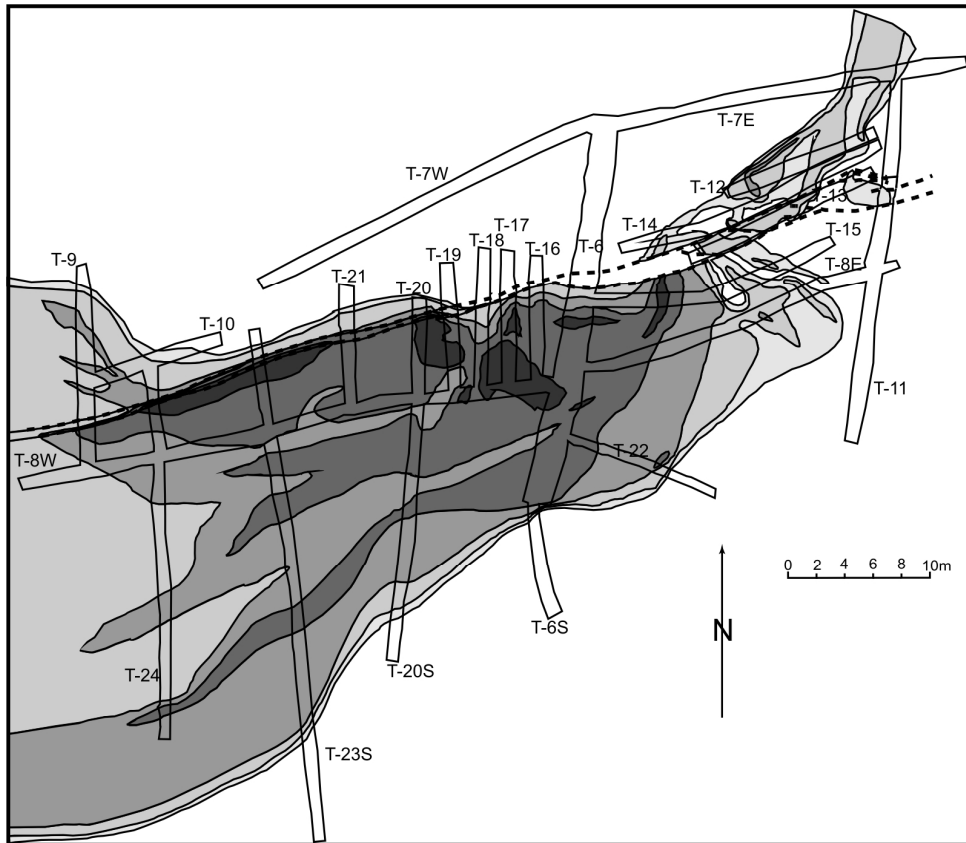


Figure 5.7. Thickness map for reference unit 200 at the Saros site. Patterns do not coincide on both sides of the fault zone, especially concerning apices (locus of maximum thickness). This suggests some lateral movement affected these units since they deposited.

The age of unit 200 is well constrained to be younger than A.D. 1655. We dated several samples from this unit, along with those above and below it, and use the youngest date to constrain its maximum age. All of the samples constrain the sand to the past 500 years, but sample T6-43, recovered from stratified alluvium within the channel, can be no older than A.D. 1655 and may be considerably younger. Thus, we interpret all of the C-14 samples that lie above this unit and that have older apparent ages to be the result of either reworking of detrital charcoal, or more likely, the consequence of the charcoal (and its original wood) having been resident in the system for some period of time. The post-1655 date places strong constraints on which earthquakes may have produced surface rupture at this site and added to the observed amount of offset on unit 200, as discussed below.

The stratigraphic units above unit 200 can be designated as either sedimentation within the fault zone, possibly due to formation of a depression along the fault, or the result of overbank sedimentation by the Kavak River and its tributary channels. Units 192-198, recognized in T-6E (Fig. 5.4) and in adjacent trenches to the west, are interpreted to be a

fine-grained deposit that fills a narrow trough between the unit 200 fan and a low fault scarp. Although this may be interpreted as the result of deformation along the fault, we prefer an interpretation that invokes purely stratigraphic mechanisms to produce this deposit because there is no direct evidence for a surface rupture in this part of the section. Furthermore, the isopach map of the sand in Fig. 5.7 clearly shows a fan that splays out and flows west, parallel to the fault, thereby producing a slight low along the fault. Thus, there is no need to require a faulting event to produce this low.

In contrast, units such as 110-140 in trench T6 fill a depression that formed immediately after a surface rupture, as indicated by faulting and fissuring up to the base of that section. In these cases, the units may be only very locally preserved along the fault, although their significance to the interpretation of the event stratigraphy may be profound.

Units 10-100 are sandy to silty sediments that bury the fault scarp and are presumably derived from flood events from the Kavak River. Unit 10 is the A horizon developed in this uppermost section and is also the active plow pan in areas that are farmed, such as to the east of the highway. We dated a number of detrital charcoal samples from units 10-190 to provide preliminary constraints on the age of the overall section. Because unit 200 was found to be younger than A.D. 1655, all higher units must be as well. The C-14 results demonstrate a variety of dates ranging between about A.D. 600 and 1630, with no particular order in the section. We interpret all of these as having had a small to large component of resident age prior to their incorporation into the sediments exposed in our trenches. From this, we interpret the entire section from unit 200 to the surface as being deposited during the past 350 years or so. As this corresponds to the part of the C-14 calibration curve that cannot be resolved without very precise ages, we did not pursue further dating of this section.

5.3.2 Evidence for Earthquakes

There was evidence observed for two large surface ruptures in nearly every trench that we excavated across the fault. In many of these, there were two deposits of well-sorted fine sand that appear to have been ejected out of the fault zone and derived from unit 200. In trench T25, we designate the earlier of these ejecta deposits as unit 195. We also observed structural evidence for two surface ruptures, with faults and fractures extending up to a specific stratigraphic level and then being overlain by unfaulted deposits. We did not construct detailed trench logs of most exposures due to the lack of time and because our focus for many of these trenches was to map out the extent of unit 200. Nevertheless, both T6 and T25 record both of these events and are discussed herein.

Evidence from trench T6 – The fault in T6 is narrow, less than 0.5 m at the base of the trench. Within this fault zone, faulting has produced liquefaction, brittle faulting, fissures, and a narrow trough into which sediment accumulated. The interpreted event horizons for each of these phenomena are coincident and correspond to the base of unit 190 and the base of unit 150.

In T6E, fractures extend to the base of unit 190 and are overlain by well-bedded stratigraphy of units 150-190. Within the fault, the section is replaced by a massive, well-sorted fine sand that we interpret as liquefaction sand derived either from unit 200 or another sand below the base of the trench. In some trenches, we exposed a deeper well-sorted sand below unit 350, and considering that the pipe extends to the base of the trench, we interpret the lower sand as the most likely source. This liquefaction sand is also overlain by unit 190 along both margins of the fault zone in this exposure. Finally, along the northern edge of the fault zone, a narrow depression is filled by finely laminated stratigraphy of units 150-190. We interpret the depression to be a direct result of a surface rupture.

East of the highway, we constructed detailed logs of the fault zone in trench T25 to further constrain the timing and number of events that post-date the unit 200 sand. At the time of the field exercise, we did not know that the sand was younger than can be adequately addressed with C-14. Nevertheless, our observations provide additional constraints on how many events post-date unit 200. It should be noted that the earlier study by Rockwell et al. (2001) also found evidence for only two surface ruptures after deposition of their unit 3, which is identical to unit 200 described herein. Trench T25 lies within 10 m of Rockwell et al.'s (2001) trench T-1.

In the east wall of T25, the northernmost fractures extend up through unit 200 and are overlain by another clean sand (unit 195) that we interpret as ejecta derived from unit 200. Massive clean sand fills the main fault and is also interpreted to be the result of liquefaction of unit 200. Overlying unit 195 is a sequence of bedded silt and sand units (units 160-190) that are not faulted by the northernmost strand of the zone. These observations all indicate a surface rupture that occurred when unit 200 was at the surface.

Another set of fractures displaces all units up through 160, including unit 195 (liquefaction sand from the penultimate event). Chunks of bedded stratigraphy, comprised of units 160-190, lie floating within the fault zone in a massive, fine sand matrix that we interpret as the result of re-liquefaction of the unit 200 sand.

In the west wall, similar relationships indicate two liquefaction events, one immediately after deposition of unit 200 and another after deposition of unit 170. After the second liquefaction event, finely laminated silt and sand was deposited on the southern, downthrown side of the fault. There is not clear evidence for two fracturing events, presumably because the most recent event re-liquefied material and erase such evidence.

Nevertheless, the vertical separation of unit 200 is considerably more than that of unit 190, indicating more than one event. Further, unit 195 is again interpreted as liquefaction ejecta that resulted from the earlier event.

The above observations indicate two surface ruptures preserved in the stratigraphy, one at the contact at the base of unit 190 and one before deposition of unit 150. These are identical to the relationships determined in trench T6 and we interpret these to be the same two events. Thus, at these and all other exposures that we examined in our field exercise, we note evidence for two ruptures that produced liquefaction, surface faulting, and consequent sedimentation along the fault. Both of these events must have occurred after deposition of the channel sand of unit 200, or after A.D. 1655. The only two large events that may be ascribed to these surface ruptures are the large regional events of August 1766 and November 1912 (Ambraseys and Finkel, 1987a, 1987b, 1995, Rockwell et al., 2001). Thus we attribute lateral slip on unit 200 to be the cumulative result of these two earthquakes.

5.3.3 Determination of Lateral Slip

The channelized nature of unit 200 is ideal for resolving cumulative slip for the two events that post-date its deposition. From the aerial photographic analysis, it appeared that the paleo-channel containing unit 200 flowed at a high angle to fault. We chose the area west of the highway to conduct the detailed 3D portion of this study because the area is devoid of agriculture and we were unrestricted in our ability to excavate long trenches both across and parallel to the fault zone.

In the preliminary excavations such as trench T6, we were not certain as to the aerial distribution of the unit 200 sand, so we began fault-parallel excavations to determine its extent. In all, we excavated 19 trenches and trench extensions to resolve the geometry of the unit 200 deposit. All exposures were surveyed with a Wild TC 2000 total station to provide accuracy. Further, a surveyed string line was emplaced in all trenches at the same elevation to assure accurate measurement of the sand thickness and the relative elevations of its top and base. Because we couldn't make detailed logs of all exposures in the amount of time we had in the field, we instead took over 1500 detailed measurements on the thickness of the sand, including the exact locations of the pinch outs, to construct an isopach map of its distribution (Fig. 5.7).

Unit 200 is much thicker on the south side of the fault than on the north. We take this to indicate that a low scarp was present at the time the channel flow across the fault. North of the fault, the sand is confined to a narrow channel and never exceeds 20 cm in thickness. The channel slopes to the south, towards the fault, and then thickens to over 40 cm where it crosses the fault. The overall form is that of an alluvial fan, and we interpret the channel to

have splayed across the fault scarp, resulting in deposition of the main fan on the south side. The fan deflects downstream, towards the coast to the west, and only extends south of the fault for 5-10 m. As seen in trench T6, the fan has a convex-up cross profile and is multi-lobed. The apex of the fan is exposed in trench T15, and the fan rapidly thins to the east and pinches out in trenches T8 and T15. To the west, the fan is bound on the north by the fault for a distance of about 30-35 m, and then the edge of the fan crosses the fault with 10-15 cm of deposition north of the fault. In the vicinity of T6 and the area of the feeder channel, unit 200 is thickest away from the fault except at the fan apex.

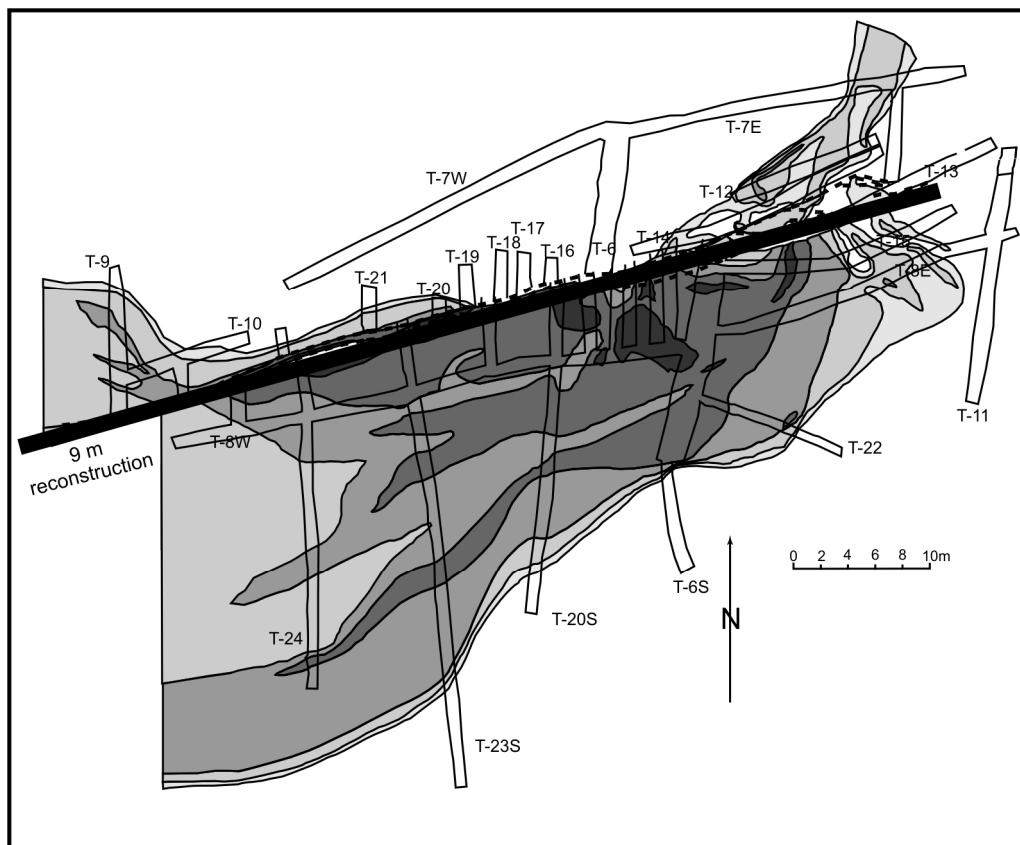


Figure 5.8: Reconstructed isopach map of unit 200 fan from trench observations and microtopographic survey. Proper match is obtained after 9 m of right-lateral displacement is retrodeformed.

We reconstruct the fan apex with the deepest portion of the feeder channel to resolve about 9 m of lateral slip (Fig. 5.8). A secondary smaller channel west of the main channel also reconstructs to a secondary fan apex, and the margins of the fan to the east of the feeder channel all realign. Furthermore, the thickest portion of the fan that ponded adjacent to the fault west of T-6 realigns to the thinner section of sand that spilled across the

fault to the north. The uncertainty in the 9 m estimate is on the order of about a meter, based on the realignments and their mismatches if the reconstruction is less than 8 m or greater than 10 m. We take this 9 ± 1 m value as the cumulative slip produced by both the 1766 and 1912 earthquakes. If each earthquake produced similar slip at this site, then the ~4-5 m of presumed slip is similar to the average values for many of the large earthquakes that have ruptured the North Anatolia fault this century. It is also consistent with the amount of slip predicted by Ambraseys and Finkel (1987) for the 1912 earthquake, based on the inferred size and expected amount of slip.

5.4 Izmit to Sapanca Segment

We initiated paleoseismic studies along the Izmit-Sapanca fault segment in October 1998 prior to the earthquake. In our preliminary work, we focused on dating a canal feature that was possibly the result of an effort by the Ottomans in 1591. After the earthquake, we returned to the canal to resolve how many earthquakes had affected the canal stratigraphy. We also began trenching west of the end of the canal along a small fluvial channel in the township of Köseköy with the purpose of resolving a longer record. As will be shown, the records at both sites are similar and only record fault activity for the past 400 years or so.

5.4.1 The Ottoman Canal Site

Multiple periods of canal construction have been discussed in the literature (Finkel and Barka, 1999), with at least two known efforts of excavation. The earliest effort is pre-Roman and was intended to connect Lake Sapanca with Izmit Bay, thereby opening up commerce and access to the inland forests and other resources. A number of subsequent efforts were “discussed” (mentioned in court records, etc.) although most of these were never undertaken. The most recent effort, for which there is direct historical documentation and known expenditures, was undertaken by the Ottomans in 1591. In a preliminary effort in 1998, we excavated the south margin of a large, abandoned canal at Tepetarla with the purpose of dating the construction of this prominent feature that crosses the fault zone between Tepetarla and Köseköy. The canal extends from near Lake Sapanca westward about half of the distance to Izmit Bay, consistent with historical accounts for the 1591 effort. The purpose of our initial trench was to resolve whether this was the Ottoman effort of 1591 or an earlier canal effort.

We observed that there were numerous pieces of small to large detrital charcoal, some that were associated with burn zones, that we interpret represent cooking fires or fires to boil water for tea (as is a common practice today in Turkey). We collected eight large samples and dated four of the samples to place maximum ages on the berm construction,

and therefore the canal excavation project. In that it is likely that the workers burned dead wood for their fires, and as there are numerous large trees in the area today, we surmise that all of the samples will be older than the actual age of the berm. As it turns out, the ages of the detrital charcoal pieces range from a maximum age of 112 BC to as young as AD 1402. We therefore infer the berm and canal construction to post-date the youngest sample dating to the 14th century, and to be the effort funded by the Ottomans in 1591. Thus, all of the alluvial fill within the canal must date to younger than 1591 so we did not attempt further C-14 dating in the canal fill.

5.4.1.1 Site stratigraphy

In the summer of 2000, we excavated a trench across the 1999 rupture west of Tepatarla where the fault is entirely contained within the canal fill (Fig. 5.1b). The trench site was chosen about 2 meters west of a small several-meter-long open extensional fissure resulting from a 1 meter-wide releasing step-over. The trench exposed predominantly fine-grained, bedded clayey canal fill, although distinctive sand was found to fill a fissure zone within the fault zone, apparently resulting from a prior rupture (Fig. 5.9). The fault zone is approximately 3 meters wide in the trench, although the 1999 rupture zone is narrower.

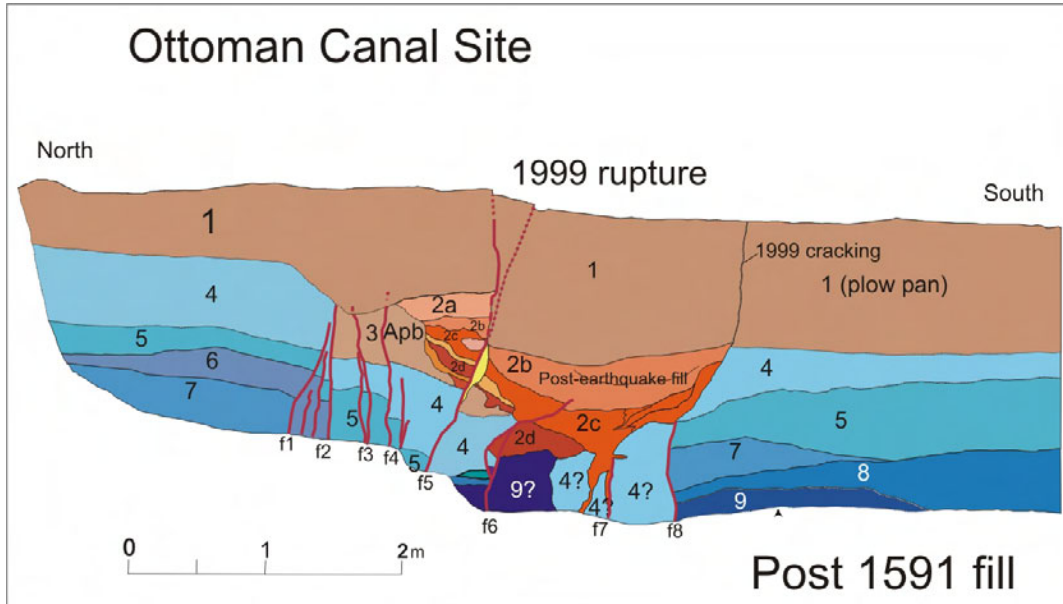


Figure 5.9: Log of trench opened on a trace of the North Anatolian fault within an Ottoman canal near Tepatarla, east of Marmara Sea. Investigating recent surface faulting (1999 Izmit earthquake) led to the observation of previous surface rupturing events.

The stratigraphy was differentiated into nine units, with the topmost and youngest unit (unit 1) interpreted as a plow pan. Unit 1 is massive silty clay, similar in texture to several of the underlying strata. Unit 2, which is bedded and further subdivided into several subunits, is in part an alluvial fill within the fault zone. Unit 2a is a fine silty sand that is only present north of the 1999 rupture trace. Unit 2b is clayey silt that fills a depression within the fault zone. In contrast, unit 2c is a coarse gravelly sand which not only fills the depression in the fault, but also extends downward in the fractures to the base of the trench. This unit grades upward in to sand at its top. Unit 2d is well-sorted fine sand and we interpret this unit to be the result of liquefaction and is likely derived from a clean sand below the base of the trench. Units 2a through 2d may comprise a fill sequence in a fissure within the fault zone following an earthquake.

Unit 3 appears to be a buried topsoil unit that was incorporated into the fault zone and bound by fault strands from an earlier event. Unit 4 is massive pebbly clay to clayey sandy silt (varies laterally) that grades down to the pebbly silty clay strata of units 5 and 6. These units are interpreted as quite water canal fill alluvium, although the presence of scattered pebble clasts may alternatively suggest a debris flow origin. Unit 7 is oxidized, finely bedded silt grading downward to sand, whereas unit 8 is a well-sorted sand. Unit 9 is a sandy gravel of probable fluvial origin, and units 9 through 7 apparently represent a fining upward fluvial sequence. The unit designated as 9? Within the fault zone is lithologically similar to both unit 9 and unit 2c and may be part of the section that liquefied or was mobilized during liquefaction of unit 9.

We did not directly radiocarbon date any of the strata within this trench, although detrital charcoal was abundant and we collected over 50 samples from this trench. However, as the base of the canal was not encountered (the base should be greater than 5 m depth), we infer the entire section to post-date A.D. 1591. In that many or most samples likely have some residence age (growth plus burning prior to burial), and because of problems with calibrating C-14 dates after about A.D. 1600, we did not see the utility in spending the effort to further date the section. Nevertheless, all earthquakes recorded at this site must also post-date A.D. 1591, which is fairly well-recorded in the history for this region.

5.4.1.2 Evidence for Prior Earthquakes

There is clear structural and stratigraphic evidence for at least one and possibly two events prior to that of 1999. For discussion purposes, we have numbered the individual fault cracks as f1 through f8 from north to south. In a couple of cases, minor faults are grouped with more major ones. Several of these faults moved in at least one prior event, whereas only a couple appear to have been reactivated in 1999, which is referred to as event E1.

The 1999 (E1) rupture localized along a narrow crack, fault f5, near the center of the trench and displaces all strata up through unit 1 to the surface. A second surface crack aligns with fault f8, and this fault becomes the edge of a 2-m-wide pull apart that produced a narrow sag in 1999 only 2 meters east of this trench face. In the trench wall, this fault appears to have only cracked and no evidence of any significant displacement could be resolved. The base of the soil may be offset by a couple of centimeters, but that was not clear. Below the cracked soil, however, fault f8 defines the southern edge of the fault zone and was clearly active and a main player in an earlier event. Along fault f5, the principal 1999 displacement surface, different units are juxtaposed and similar units have significant variations in thickness across the fault. We attribute these relationships to the ~3-4 m of lateral slip recorded for the 1999 earthquake in this vicinity.

At least one earlier event, E3, is strongly indicated by the occurrence of a number of fault strands that break units 3-9 but are overlain by the unbroken soil of unit 1. Fault f2 drops an older topsoil horizon, unit 3, down against units 4 and 5, and the mismatch in unit thicknesses across this fault indicates substantial lateral slip. Faults f1, f3 and f4 also cut units 3 through 7 but are overlain by unit 1. There is no indication that any these faults were activated in 1999. Faults f6, f7 and f8 also appear to have activated in this earlier event, which apparently resulted in an open fissure at the surface that was subsequently filled by unit 2. Unit 2d is a fine sand that may be the result of a sand blow. Unit 2c, in contrast, is a gravelly sand that is intrusive downward into the fault zone and is very similar to the sandy gravel of unit 9. We observed gravelly sand mobilized during the 1999 earthquake, resulting from liquefaction and lateral spreading on the shoreline at Sapanca, so we surmise that this gravel may also be a consequence of liquefaction, in spite of its coarse nature. In any case, the occurrence of the unit 2 deposits precisely within the fault zone virtually requires that an open fissure was present after deposition of unit 4 and the development of the soil of unit 3. We attribute the presence of the unit 2 deposits to this earlier faulting event.

A third event that is intermediate in age between events E1 and E3 is suggested by the breakage of the unit 2 fill by fault f6, which juxtaposes units 2d and 4, and causes a significant mismatch in the thickness of unit 2c. The upward termination of fault f6 appears to be in unit 2b, and we could not trace any evidence of this fracture upward to the modern ground surface. Based on the mismatch in stratigraphic thicknesses and the juxtaposition of dissimilar units, we infer that this fault must have significant lateral slip. The problem with a surface rupture interpretation at this stratigraphic level is that unit 2b apparently fills the depression left by event E3 and it is difficult to believe that the depression lasted for too long after the surface rupture. Thus, event E2 must have either occurred soon after event E3 or the site was closed to significant deposition for some extended period of time after event E3, which is possible considering the sites presence within the canal.

An alternative explanation is that fault f6 deformation is absorbed in the fine-grained fill of units 2b and 1 and that this fault was activated in 1999. Support for this idea is weak, but is based on the inference that unit 2b is only slightly younger in age than unit 2c, which appears to have directly resulted from the earlier event. However, the evidence for lateral slip along fault f6 is strong and would require a significant amount of strain being absorbed in unit 2b.

A third possibility is that unit 2c is a fluvial deposit that filled/eroded along the fault after event E3 and was faulted by both faults f6 and f7 during event E2. The fissuring of unit 2c downward into the fault could be explained by this mechanism and therefore would not require liquefaction of the sandy gravel of unit 2c.

We attribute event E3 to the large event of 1719 that had descriptions of damage that closely parallel those of 1999. It is the first large event after 1591 for this area and was apparently as large as 1999, consistent with the trench observations that indicate event E3 was a major surface rupture. Considering the case that event E2 occurred soon after that of E3, we attribute that deformation to either afterslip or possibly the 1754 earthquake, which is known to have produced damage in this region but for which the source is unknown. Later earthquakes, such as 1878 or 1894, appear to have occurred too long after event E3 and the surface soil of unit 1 would almost certainly have developed by that time.

5.4.2 The Köseköy Site

The Köseköy site lies along a section of rupture in the southeast corner of the township of Köseköy, south of Izmit and west of the end of the Ottoman canal. Rupture in this area in 1999 included about 2 m of slip along the primary fault strand, and secondary rupture along faults that splay off to the north from the main strand. Rockwell et al. (2002) report offsets of surveyed trees adjacent to this site to be on the order of 1.8-2.25 m, consistent with slip values reported from rupture mapping after the earthquake (Barka et al., 2000). To both the east and west of the Köseköy area, slip along the Izmit-Sapanca rupture segment generally exceeded 3 m in 1999, and slip values as high as 3.8 m based on surveyed data were reported by Rockwell et al. (2002). We interpret this to mean that slip is distributed across multiple strands in the Köseköy area. We chose this site in part because the secondary faulting could be demonstrated to be principally dip slip, making past earthquake recognition and reconstructions easier. Furthermore, paleo-earthquake events can often be easier to recognize where multiple fault splays are present as some secondary faults may rupture in only one or two events. Finally, part of our group (Ferry et al., 2004) conducted ground-penetrating radar (GPR) profiles at this site and identified an offset buried paleo-channel that is apparently offset about 6.6 m, roughly three times the 1999 slip. We had also hoped

to establish a longer record than that at the Ottoman canal site, but as will be shown, the upper 2 m of section generally covers the same time period – the past 400 years.

5.4.2.1 Site stratigraphy

We excavated five trenches at this site (Fig. 5.10), with only trench 3 crossing the main fault. Trench 1, which is presented in detail (Fig. 5.11), was excavated across a purely dip-slip fault that experienced about 60 cm of slip in 1999. A nearby small flume displayed no evidence of lateral slip (Fig. 5.10), thereby confirming the normal slip inference for the fault in trench 1. Thus, no out-of-plane transfer of sediments is expected and past events should be recognized by similar dip-separations.

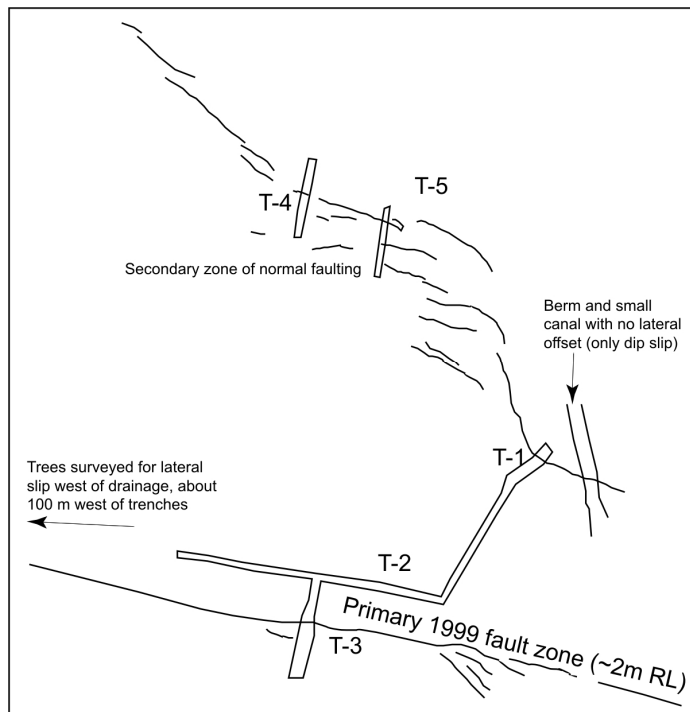


Figure 5.10: Location map of the Köseköy trench site showing surface rupture produced by the 1999 Izmit earthquake as well as trench layout.

The stratigraphy in trenches T-1 and T-3 is composed of a sequence of coarse and fine-grained strata that are interpreted as fluvial channel and overbank deposits (Fig. 5.11). Unit 1 is a dark brown plow pan (topsoil A horizon) unit that was tilled frequently. Units 2 and 3 are bedded channel deposits, with unit 2 being a distinctive sandy gravel and unit 3 being a stratified coarse to fine sand. These units pinch out to the north across a paleo-scarp (Fig. 5.11) and locally scour into the underlying unit 4. We interpret this part of the section to represent a period of sedimentation prior to the current incision of a drainage located a few meters south of the southern end of trench T-3.

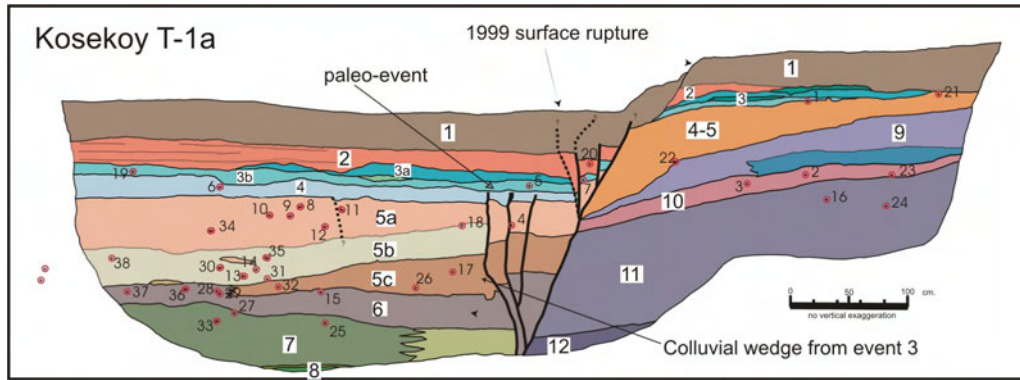


Figure 5.11: Log of trench T-1 from the Köseköy site. Poor lithological correspondence between both sides of the fault zone and colluvial wedges point to predominant vertical displacements.

Unit 4 is a dark brown, massive, clayey silty sand (loam) that we interpret as a buried A horizon or topsoil. This unit was easily mappable south of the fault but north of it, unit 4 appeared to become less distinct so we grouped it with unit 5 to the north. Unit 5 itself is a weakly stratified clayey silt with sand that grades downward to a pebbly, sandy clayey silt. North of the fault, the equivalent unit, unit 4-5 is a massive pebbly clayey silt that we interpret as a colluvial unit.

Unit 6 is a very distinctive plastic clay that was only exposed south of the fault and appears to thicken towards the fault. We interpret unit 6 as an overbank deposit, although it may be clay derived from overbank sedimentation ponded within the fault zone. Unit 7, in contrast, is a gravelly clayey silt that appears very similar to unit 5. The gravel content is sparse away from the fault but increases towards the fault, suggesting a colluvial origin for this unit as well. Finally, south of the fault, unit 8 is a distinctive coarse sand interpreted to be fluvial in origin. This sand was traced laterally towards trench T-3 and forms the channel deposit imaged by Ferry and Meghraoui in their radar survey.

North of the fault, trench T-1 exposed several older units below unit 4-5. Unit 9 is a bedded coarse sandy, clayey gravel interpreted to be fluvial in origin. There was no equivalent for this unit exposed south of the fault, although it is the probably source for the gravelly colluvium of unit 7. Unit 10 is a distinctive silty fine sand with scattered gravel, unit 11 is a coarsely bedded gravel containing abundant pottery and tile shards, and unit 12 is a distinctive coarse sand. Collectively, units 9 through 12 are interpreted as a fluvial sequence of strata preserved on the northern upthrown side of the fault zone.

Age control for the stratigraphy in T-1 is provided by dating of individual detrital charcoal samples. Charcoal was abundant in our exposures, and we collected over 200 samples from the Köseköy site. In T-1 alone, nearly forty samples were collected and we

dated six. Four samples were dated from units 3 through 7 and two from the older units north of the fault.

All four samples from units 4-7 yielded modern or nearly modern results. The sample from unit 7 yielded a calibrated age of AD 1688-1927, requiring that all over lying units are also no older than 1688. Thus, most of the exposed section south of the fault was deposited during the past 335 years or so.

North of the fault, two samples were dated from units 10 and 11, with the lower sample from unit 11 yielding a slightly younger calibrated date range of AD 444-630. As both sample ages are indistinguishable at 2σ , and as they both place the age of these units at about the 5th-6th century AD, we accept these dates as the approximate age of this older fluvial section. Thus, there is over a thousand year hiatus in deposition on the northern side of the fault, although much of the record may be preserved at depth below the current base of T-1 to the south.

5.4.2.2 Interpretation of Past Earthquakes

We recognize evidence for at least one and possibly two events recorded in the stratigraphy south of the fault exposed in T-1. The most recent event is obviously the August 1999 Izmit earthquake, and is designated as event E1. Earlier events are easiest to recognize once the 1999 deformation is removed. In that the 1999 earthquake produced no lateral slip at trench T-1, we reconstruct the pre-1999 section assuming no out-of-plane motion (Fig. 5.12a), which required about 53 cm of dip reconstruction.

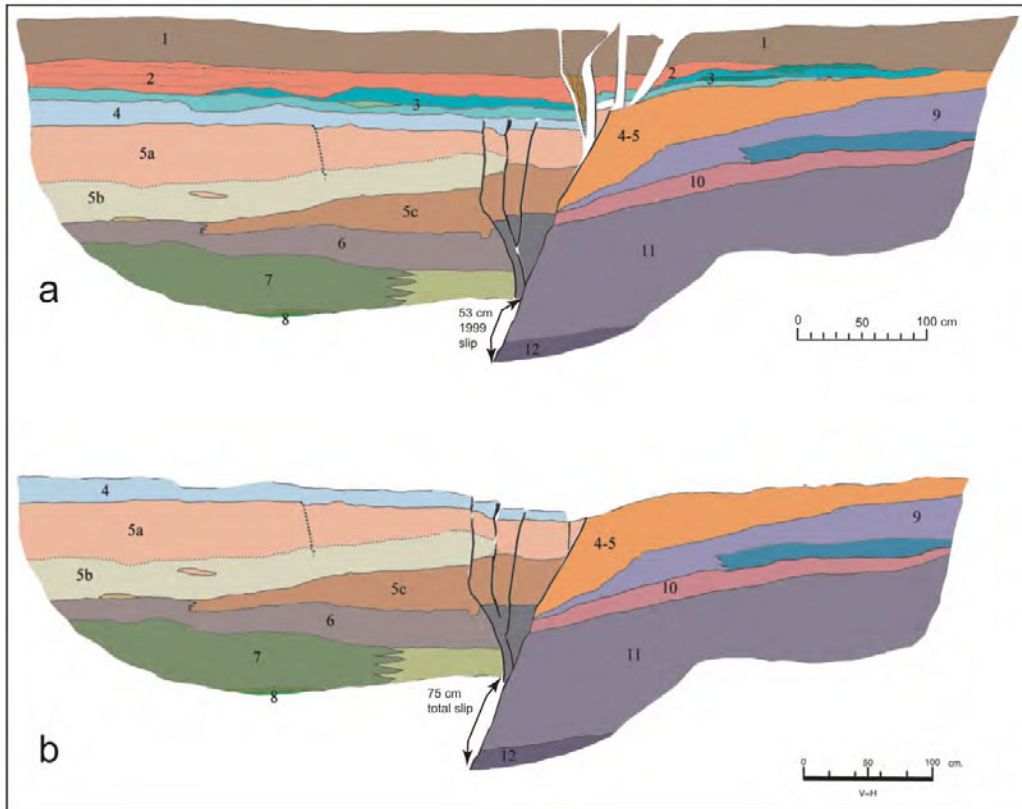


Figure 5.12: A) Retrodeformation of trench T-1 results in removal of deformation induced by the last event (1999 Izmit earthquake). It reveals a previous event (E2) occurred after the deposition of unit 4 and before the deposition of unit 3. B) Retrodeformation of event E2 indicates a total of 75 cm of dip-slip for the last two events (cumulated E1 and E2).

Evidence for the penultimate event (prior to 1999) is clear in Fig. 5.12a, where several secondary strands break up through unit 4 but are planed off and buried by unit 3. Unit 3 also pinches out north of the fault, indicating the presence of a scarp at that time. In the reconstructions of Fig. 5.13a, these relationships are even more obvious, with units 2 and 3 pinching across a buried fault scarp produced by the penultimate event. Units 6 through 4 are faulted by the secondary strands and overlain by units 1-3. A degraded scarp supported by units 4 and 5 is evident. From these observations, we interpret event E2 to have occurred after the deposition of unit 4 and prior to the deposition of unit 3. Based on the ages of these units, E2 must have occurred after AD 1688.

We attempted to remove the deformation of event E2 with further reconstruction of the units faulted in E2 (Fig. 5.12b). We reconstructed units 4-6 across the secondary strands, and restored or re-matched units 4 and 5 south of the fault to unit 4-5 north of it. This required an additional 22 cm of reconstruction, or about half of that required to remove

the 1999 deformation. This reconstruction resulted in an apparent depression along the fault, part of which is explained by the subsequent uplift and erosion of unit 4 during and after event E2. The balance is explained by erosion of unit 4-5 on the north after the formation of the scarp. The volume represented by this depression was evidently removed by the unit 3 channel deposits.

Several important observations can be made about an earlier event, E3, from the reconstruction presented in Fig. 5.12b. First, units 4 and 5 appear to have been deposited against and across a scarp underlain by unit 9 north of the fault. This interpretation is based on the observation that these units pinch out northward, similar to what happened to units 2 and 3, requiring the presence of such a scarp. However, in detail, unit 5c is thickest at the fault and thins southward, indicating that it may be a colluvial wedge derived from the scarp itself. This would require that the lower part of unit 4-5 was already present at the time of the event. In this case, unit 4-5 is older than unit 5 and our numbering scheme is in error. Alternatively, units 4 and 5 (and 4-5) represent slow accumulation of colluvial materials across a scarp, largely derived from uphill to the north, and the wedge-like appearance of unit 5c is in part due to the massive character of unit 4-5 north of the fault and non-recognition of that contact. In this interpretation, event E3 occurred before deposition of unit 5 altogether.

In the reconstruction in Fig. 5.12b, units 6 and 7 appear to be in fault contact. This requires that they were either faulted down into this position or that they were deposited against the scarp (or derived from it) after an event. In that the relationships within the fault zone have been obscured by the two subsequent events, either interpretation is permissible. Unit 6 is very fine-grained clay that is only present south of the fault and thins to the south. The thinning may be an artifact of our limited exposure. Nevertheless, it is thickest at the fault. This may be localized quiet-water sediment within the fault zone due to the presence of a depression. This would require an event after deposition of unit 7, and there is no other evidence for this assertion. Unit 7, in contrast, has the appearance of being a fault-derived colluvial unit, as it is coarsest at the fault and fines southward. This observation suggests that it was derived off of a scarp to the north, possibly in large part to erosion of units 9-11. If this is the case, then event E3 occurred shortly before deposition of unit 7.

The above observations are not all consistent on when event E3 occurred. Nevertheless, it is difficult to envision how units 4 through 7 were deposited in the current configuration without a scarp-forming event, as that would have required a steeply dipping free face exactly coincident with the fault.

Another observation that is consistent with the occurrence of three events after deposition of unit 8 is based on a GPR survey conducted by M. Ferry and M. Meghraoui at this site (Ferry et al., 2004). Prior to trenching, they ran GPR surveys parallel to the 1999

rupture and imaged buried channels on each side of the fault. North of the main rupture, we encountered one channel in our trench 2. The channel deposits fine northward to become the coarse sand of unit 8. South of the fault, the interpreted correlative channel is laterally displaced about 6.5 m westward. We attempted to trench to the depth of the channel. However, saturated conditions and a collapsing trench wall precluded a direct look at this deposit south of the fault. If the GPR correlation and estimate of slip is valid, approximately three times the amount of slip as occurred on the main rupture would be required to restore the lateral offset of the unit 8 channel. This is consistent with our inference that three events are required to explain all of the relationships observed in trench T-1.

Event E1 is the 1999 Izmit rupture. Event E2 is possibly the large 1719 earthquake that apparently broke the same section of fault based on historical accounts (Ambraseys and Finkel, 1995). However, our observations suggest the vertical slip in event E2 was smaller than that of 1999 whereas the 1719 earthquake appears to have been as large. It is possible that 1719 ruptured through the site from a different direction, making displacement observations on secondary faults of less value. It is also possible that this secondary fault displays variable amounts of slip in each earthquake. Another possibility is that event E2 is more recent than 1719, and is possibly 1754.

Event 3 must have occurred after deposition of unit 8 but before unit 5. The detrital charcoal date on unit 7 indicates that it is no older than AD 1688. Thus, it is possible and even likely that both events E2 and E3 post-date 1688. If this is the case, then event E3 may be the 1719 surface rupture.

5.5 Discussion of Results

We have demonstrated that west of the Marmara Sea step-over along the Saros-Ganos fault, ~9 m of lateral slip has been released along the North Anatolia fault during the past few hundred year. We have identified two large surface ruptures that produced this slip, and the historical record indicates that these are probably the large regional earthquakes of August 1766 and November 1912.

To the east of the Marmara Sea, we excavated trenches across the 1999 Izmit rupture at Köseköy and in a 1591 Ottoman trench. At both sites, we can demonstrate that three surface ruptures have occurred at each site. In the case of the Ottoman canal, we can only constrain these to post 1591. At the Köseköy site, however, it appears that all three post-date 1688. Furthermore, the middle event, E2 at each site, appears to be the smallest of the three. These may be the earthquakes of 1719 and 1754 or 1878, with the latter two being arguably smaller based on historical accounts (Ambraseys and Finkel, 1995). The

1999 main rupture trace at Köseköy had low slip relative to sites to the east and west (Rockwell et al., 2002), in part related to some off-fault deformation. If the 3 ± 0.5 meters of slip is more representative for the Izmit segment, as implied by Rockwell et al. (2002), then as much as 9-10 m of slip may have occurred along the Izmit segment in the past 330-410 years. Thus our results indicate similar amounts of strain release during the past several hundred years both to the east and west of the Marmara Sea.

Hazard to Istanbul

An assessment of the likelihood of a large earthquake beneath the Marmara Sea near Istanbul must account for not only the recent behavior of the North Anatolian fault, as has been done by Parsons et al. (2000), but the past history of the fault zone based on paleoseismology.

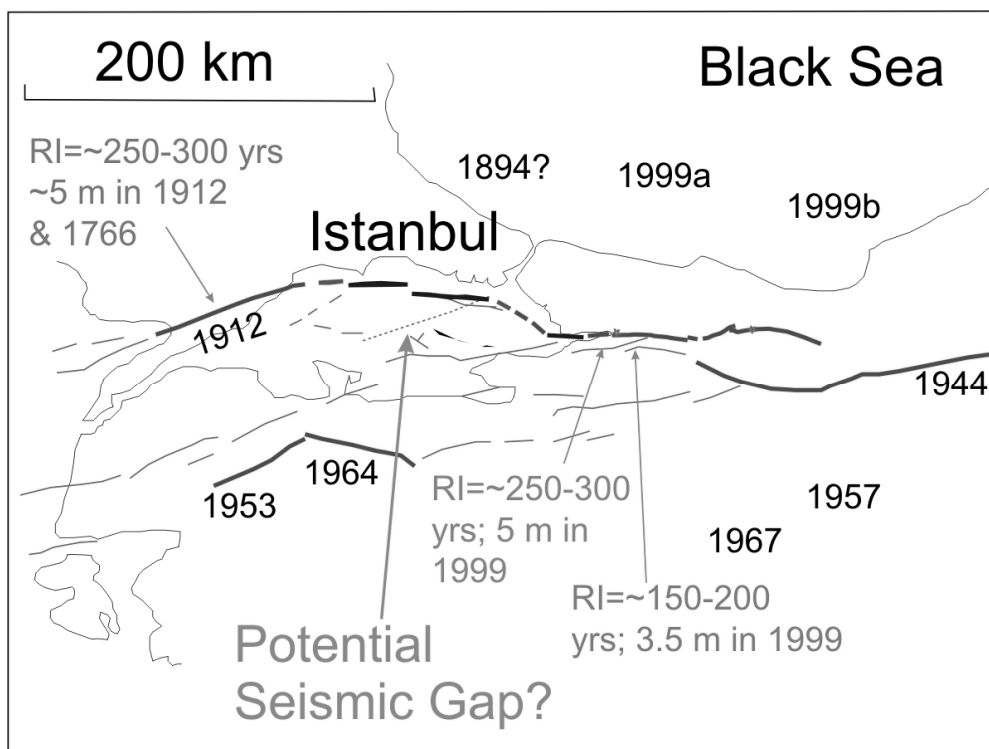


Figure 5.13: Summary of results from the present study along with recent strong events in the Marmara Sea region. RI: recurrence interval.

The North Anatolian fault has experienced a sequence of earthquakes this past century that is unprecedented. The fault zone has essentially unzipped from east to west in this sequence, beginning in 1939 with the M7.7 Erzincan earthquake. A westward progression of earthquakes followed, with large ($m > 7$) earthquakes rupturing westward in 1942, 1943, 1944, 1957, 1967 and 1999 (Stein et al., 1997) (Fig. 5.1). There were also

earthquakes that occurred to the east after the 1939 event. The 1999 earthquakes culminated this sequence, with ≥ 4 m of rupture now having occurred along the entire fault since 1939 from east of Erzincan to about the Hersek peninsula, west of Gölcük.

West of the Marmara Sea, the North Anatolian fault experienced rupture in the 1912 earthquake from the Marmara to at least the Gulf of Saros, which followed an M7 earthquake to the west in 1893 offshore in the Gulf along the Greek coast line (Nick Ambraseys, personal communication). Thus, the NAF has experienced rupture along most of its length this century, except in the vicinity of the Marmara Sea.

Stein et al. (1997) used a model of increasing Coulomb stress to explain the westward progression of failure. They predicted that the Izmit section, west of the 1967 surface rupture, was likely to go next and gave a high probability of failure during the subsequent 30 years. Their prediction was followed by the Izmit and Düzce earthquakes only two years later in 1999. The Düzce earthquake filled in a gap along a northern strand; the 1967 Mudurnu Valley earthquake ruptured a southern trace. After the 1999 earthquakes, Parson's et al. (2000), using the same methodology as Stein et al. (1997), calculated that the fault zone in the Marmara region experienced an increase in static stress, and considering the absence of recent earthquakes there, suggest that it is the next to fail.

The historical record of earthquakes for this region is rich. In addition to the aforementioned earthquakes this century, a M7 event in 1894 also did damage to Istanbul and was believed to be centered in the eastern Marmara Sea region. Another event in 1878 may have occurred farther east, possibly in the Izmit to Sapanca section of the fault. Other than these, one must go back to a sequence in the 18th century for the truly large events to have struck the region. A very large event struck the central segments of the NAF in 1668, followed by the M7.5 1719 earthquake in the Izmit region. This was followed by the M7 1754, also somewhere east of the Marmara Sea, and the M7.6 April 1766 event within the Marmara. Three months later, the M7.6 August 1766 earthquake ruptured the Gallipoli segment along the Saros-Ganos fault. It appears, then, that the previous sequence, which occurred over a period of nearly 100 years, ruptured at least the entire western half of the fault zone. Based on our paleoseismic work, seismic slip in these events was high, similar to that in the 1999 earthquakes.

The central Marmara Sea section of the fault zone, in contrast, has not sustained significant rupture since the 1766 earthquake, and before that, the 1509 earthquake. Considering that the entire fault to the east and west has ruptured this century with ± 4 m of slip, and considering that the 1999 earthquakes increased the state of stress along the fault zone in the Marmara region, failure of the fault near Istanbul is probably imminent.

Acknowledgements

This work was funded by the USGS NEHRP program, award No. 00HQGR0034, and by Pacific Gas and Electric Company (PG&E). We are indebted to the many landowners who allowed access, the mayors of Kavakköy and Köseköy for their support, and to Lloyd Cluff and Woody Savage of PG&E who supported the field effort, allowing for the students from SDSU and ITU to be involved in this work. Finally, none of this work would have been possible without Aykut Barka. Although a coauthor, he deserves special attention and thanks, and his death in February, 2002 is a profound loss to the earthquake science community in Turkey as well as the World. He will be sorely missed.

Conclusions and Outlook

In the present thesis, we developed and applied two distinct shallow geophysics-oriented facets of the paleoseismological approach to determine recent fault behavior and slip history. Studied regions were in two very different fault settings related to the Africa/Europe collision, namely the intraplate low deformation rate Basel-Reinach fault (Switzerland) and the interplate high deformation rate North Anatolian fault (Turkey).

In Central Europe's slowly deforming region, recurrence intervals for large earthquakes are usually longer than observation windows for instrumental and historical seismological data. Hence, we carried out extensive and integrated geomorphological and geophysical surveys to identify the fault and characterize its geometry, dimensions and slip mechanism. Numerous geological, and non-geological, limiting factors restricted the resolution we could achieve. Specifically, a strong erosion/deformation ratio prevents subtle morphological features to be preserved and visible today, thus prompting to use relatively high-penetration/low-resolution methods. However, at some punctual sites, combined trench, geomorphic and geophysical observations yield original mid-term deformation rate values and recent event chronology. Hence, we could demonstrate that the 1356 Basel earthquake is related to a complex deeply-rooted normal fault system that displays a mean recurrence interval of ~2600 years and ~0.2 mm/yr deformation rate over the Holocene and late Pleistocene. This constitutes the first comprehensive paleoseismic study for that region with direct application to the seismic risk level which has been consequently noticeably lowered.

In the Middle East, where the Africa/Europe collision is intense and displays a complicated pattern involving the Arabia plate, recurrence intervals are shorter by an order of magnitude with respect to Central Europe's and as many as 3 or 4 events have been observed and reported for single fault segments during the last millennium. Furthermore, a sequence of large and destructive earthquakes has occurred along the North Anatolian fault during the 20th century and provides unambiguous surface faulting features to start with. A low erosion/deformation ratio helps preserve morphology and local conditions produce fine sand to gravel deposits, favorable to high-resolution electromagnetic techniques and high-resolution trenching. There, geophysical surveys were dedicated to detect concealed recent fault strands and pertaining buried offset features to optimize and complement trench

investigations. Indeed, we could determine coseismic slip for two previous historical events and show that characteristic earthquakes occur on the Izmit-Sapanca segment of the North Anatolian fault with direct impact on earthquake recurrence models.

Considering that little is known about destructive active faults' behavior in slow tectonic regimes, due to i) the relative intensity of erosion with respect to deformation, ii) the incompleteness of the instrumental and historical records with respect to earthquake recurrence intervals and iii) the pertaining apparently low risk level, we would recommend that historical earthquake catalogues be systematically re-evaluated and paleoseismic studies -at least geomorphological and geophysical investigations to detect and identify- be carried out in vulnerable regions. This is especially important in regions of presently low seismic activity where instrumental data may be misleading and historical data are the only insight on past destructive events. For Switzerland, we would recommend a first assessment of potentially active faults in vulnerable regions through detailed geomorphic studies. Indeed, it is still not clear whether recent glacial periods completely erased modifications in the landscape. There may be sites with sufficient remaining geomorphic signature to demonstrate activity and lead to proper trench sites.

In regions of present-day high seismicity where coseismic displacements are larger than 1 m, high-resolution geophysical surveys such as GPR and electrical tomography may help complement and improve standard trench investigations by i) unveiling concealed recent surface rupture, ii) detecting buried features and documenting related deformation and/or iii) displaying details about the complexity of the fault system. Limitations of GPR equipment prevents it from being used in areas with rough and steep topography and flat areas (e.g., fluvial deposits, terraces) should be preferred. We would suggest setting up systematic surveys on strike-slip faults with co-seismic slip larger than 1 m wherever trench investigations are planned, with time enough to survey, process and interpret sections in order to better lay out trenches and minimize their extent and overall cost. This should be done along major strike-slip faults such as the North Anatolian fault, the San Andreas fault and the Dead Sea fault, for instance.

References

- Ahorner, L., 1975. Present-day stress field and seismotectonic block movements along major fault zones in Central Europe, *Tectonophysics*, **29**, 233-249.
- Ambraseys, N.N. & Finkel, C.F., 1987a. The Saros-Marmara earthquake of 9 August, 1912. *Earthquake Engineering and Structural Dynamics*, v. 15, 189-211.
- Ambraseys, N.N. & Finkel, C.F., 1987b. Seismicity of Turkey and neighboring regions, 1899-1915, *Annales Geophys.*, v. 5B, p. 701-726.
- Ambraseys, N.N. & Finkel, C.F., 1991. Long-term seismicity of Istanbul and the Marmara Sea region: *Terra Nova*, v. 3, p. 527-539.
- Ambraseys, N. & Finkel, C., 1995. The seismicity of Turkey and adjacent areas: A historical review, 1500–1800 AD, M.S., Eren pub., Istanbul, 240 p.
- Ambraseys, N. & Free, M.W., 1997. Surface-wave magnitude calibration for European region earthquakes, *J. of Earthquake Eng.*, **1/1**, 1-22.
- Baer, M., Deichmann, N., Fäh, N., Kradofer, U., Mayer-Rosa, D., Rüttener, E., Schler, T., Sellami, S., & Smit, P., 1997. Earthquakes in Switzerland and surrounding regions during 1996, *Eclogae Geol. Helv.*, **90/3**, 557-567.
- Barka, A.A., 1992. The North Anatolian fault zone: *Annales Tectonicae*, v. 6, p. 164-195.
- Barka, A., Akyüz, H.S., Altunel, E., Sunal, G., Akir, Z., Dikbas, A., Yerli, B., Armijo, R., Meyer, B., de Chabaliere, J.B., Rockwell, T., Dolan, J.R., Hartleb, R., Dawson, T., Christopherson, S., Tucker, A., Fumal, T., Langridge, R., Stenner, H., Lettis, W., Bachhuber, J., & Page, W., 2002. The surface rupture and slip distribution of the 17 August 1999 Izmit earthquake (M 7.4), North Anatolian fault, *Bull. Seism. Soc. Am.*, **92**, 43–60.
- Barker, R.D., 1990. Improving the quality of resistivity sounding data in landfill studies. In: Ward, S.H. (ed.), *Geotechnical and Environmental Geophysics. Vol. 2: Environmental and Groundwater*, Society of Exploration Geophysicists, Tulsa, USA, 245-251.
- Barsch, D., Hauber, L. & Schmid, E., 1971. Birs und Rhein bei St. Jakob (Basel) im Spätpleistozän und Holozän, *Regio Basiliensis*, **12/2**, 286-314.
- Becker, A., 2000. The Jura Mountains – an active foreland fold-and-thrust belt?, *Tectonophysics*, **321**, 381-406.

- Becker, A., Davenport, C.A. & Giardini, D., 2002. Palaeoseismicity studies on end-Pleistocene and Holocene lake deposits around Basle, Switzerland, *Geophys. J. Int.*, **149**, 659-678.
- Becker, A., Ferry, M., Monecke, K., Schnellmann, M & Giardini, D., Multiarchive Paleoseismic record of late Pleistocene and Holocene strong earthquakes in Switzerland, in prep..
- Bender, B., 1983. Maximum likelihood estimation of b-values for magnitude grouped data, *Bull. Seism. Soc. Am.*, **73**, 831-851.
- Benedetti, L., Finkel, R., Papanastassiou, D., King, G., Armijo, R., Ryerson, F., Faber, D. & Flerit, F., 2002. Post-glacial slip history of the Sparta Fault (Greece) determined by ³⁶Cl cosmogenic dating; evidence for non-periodic earthquakes, *Geophys. Res. Lett.*, **29/8**, ?.
- Berger, G.W., Pillans, B.J. & Palmer, A.S., 1992. Dating loess up to 800 ka by thermoluminescence, *Geology*, **20**, 403-406.
- Berryman, K., Ota, Y. & Hull, A.G., 1989, Holocene paleoseismicity in the fold and thrust belt of the Hikurangi subduction zone, eastern North Island, New Zealand, *Tectonophysics*, **163**, 185-195.
- Bitterli-Brunner, P. & Fischer, H., 1988. Erläuterungen zu Blatt 1067 Arlesheim des Geologischer Atlas der Schweiz 1:25'000, *Schweiz. Geol. Komm.*.
- Bonjer, K.-P., Gelbke, C., Gilg, B., Rouland, D., Mayer-Rosa, D., & Massinon, B., 1984. Seismicity and dynamics of the upper Rhine graben, *J. Geophys.*, **55**, 1-12.
- Bonjer, K.-P., 1997. Seismicity pattern and style of seismic faulting at the eastern border fault of the southern Rhine Graben, *Tectonophysics*, **275**, 41-69.
- Bronk Ramsey, C., 1995. Radiocarbon Calibration and Analysis of Stratigraphy: the OxCal Program, *Radiocarbon*, **37/2**, 425-430.
- Brun, J.-P., Wenzel, F., Blum, R., Bois, C., Burg, J.-P., Colletta, B., Damotte, B., Durbaum, H., Durst, H., Fuchs, K., Grohmann, N., Gutscher, M.-A., Huebner, M., Karcher, T., Kessler, G., Kloeckner, M., Lucazeau, F., Lueschen, E., Marthelot, J.-M., Meier, L., Ravat, M., Reichert, C., Vernessa, S., Villemin, T., Wittlinger, G., 1991. Crustal-scale structure of the southern Rhine graben from ECORS-DEKORP seismic reflection data, *Geology*, **19/7**, 758-762.
- Burbank, D.W. & Anderson, R.S., 2001, *Tectonic geomorphology*, Blackwell Science, Malden, pp. 274.
- Busby, J.P. & Merritt, J.W., 1999. Quaternary deformation mapping with ground penetrating radar, *J. Appl. Geophys.*, **41**, 75-91.
- Cadiot, B. *et al.*, in *Les Tremblements de Terre en France*,

- Camelbeeck, T. & Meghraoui, M., 1998. Geological and geophysical evidence for large paleoearthquakes with surface faulting in the Roer Graben (northwest Europe), *Geophys. J. Int.*, **132**, 347-362.
- Camelbeeck, T., Alexandre, P., Vanneste, K. & Meghraoui, M., 2000. Long-term seismicity in regions of present day low seismicity: the example of western Europe, *Soil Dyn. and Earth. Eng.*, **20**, 405-414.
- Crone, A.J., Machette, M.N., Bonilla, M.G., Lienkaemper, J.J., Pierce, K.L., Scott, W.E. & Bucknam, R.C., 1988. Surface faulting accompanying the Borah Peak earthquake and segmentation of the Lost River fault, central Idaho, *Bull. Seism. Soc. Am.*, **77/3**, 739-770.
- Crone, A.J., Machette, M.N. & Bowman, J.R., 1997. Episodic nature of earthquake activity in stable continental regions revealed by paleoseismicity studies of Australian and North American Quaternary faults, *Aust. J. of Earth Sc.*, **44**, 203-214.
- D'Addezio, G., Masana, E. & Pantosti, D., 2001. The Holocene paleoseismicity of the Aremogna-Cinque Miglia Fault (Central Italy), *J. of Seism.*, **5**, 181-205.
- Davis, J.L. & Annan, A.P., 1989. Ground-penetrating radar for high-resolution mapping of soil and rock stratigraphy, *Geophys. Prospecting*, **37**, 531-551.
- Dawson, T.E., McGill, S. F. & Rockwell, T. K., 2003. Irregular recurrence of paleoearthquakes along the central Garlock fault near El Paso Peaks, California, *J. Geophys. Res.*, **108/B7**, .
- Deichmann, N., 1987. Seismizität der Nordschweiz, 1983-1986, Nagra Technical Report 87-05, Wettingen.
- Deichmann, N. & Rybach, L., 1989. Earthquakes and temperatures in the lower crust below the northern Alpine foreland of Switzerland, in *Properties and processes of the lower crust*, pp 197-213, eds Mereu, R.F., Mueller, St. & Fountain, D., Am. Geophys. Union Geophysical Monograph 51, Vol. 6.
- Deichmann, N., Ballarin Dolfin, D. & Kastrup, U., 2000. Seismizität der Nord- und Zentralschweiz, Nagra Technical Report 00-05, Wettingen.
- Delouis, B., *et al.*, *Tectonophysics* **221**, 413 (1993)
- Fäh, D., Giardini, D., Bay, F., Bernardi, F., Braunmiller, J., Deichmann, N., Furrer, M., Gantner, L., Gisler, M., Isenegger, D., Jimenez, M.J., Kästli, P., Koglin, R., Masciadri, V., Rutz, M., Scheidegger, C., Schibler, R., Schorlemmer, D., Schwarz-Zanetti, G., Steimen, S., Sellami, S., Wiemer, S. & Wössner, J., 2003. Earthquake Catalogue Of Switzerland (ECOS) and the related macroseismic database, *Eclogae geol. Helv.*, **96**, 219-236.

- Finkel, C., & Barka, A., 1997. The Sakarya river–Lake Sapanca–Izmit Bay canal project: A reappraisal of the historical record in the light of new morphological evidence: *Istanbuler Mitteilungen*, v. 47, p. 429–442.
- Fujimoto, K., Tanaka, H., Tomida, N., Ohtani, T. & Ito, H., 2000. Characterization of fault gouge from GSJ Hirabayashi Core samples and implications for the activity of the Nojima Fault, *Proc. International workshop on the Nojima Fault core and borehole data analysis*, U.S.G.S. Open-file report 00-0129, 103-109.
- Gupta, R.P., 2003, *Remote Sensing Geology*, Springer Verlag, Berlin, pp. 655.
- Gutenberg, R. & Richter, C.F., 1944. Frequency of earthquakes in California, *Bull. Seism. Soc. Am.*, **34**, 185-188.
- Haas, J.N., Richoz, I., Tinner, W. & Wick, L., 1998. Synchronous Holocene climatic oscillations recorded on the Swiss plateau and at timberline in the alps, *Holocene*, **8/3**, 301-309.
- Hauser, E.C., Inoue, D., Abe, S., Ksnuki, Oda, Y., 2001. 3-D GPR Imaging of the Neodani Fault, Central Japan, *Symposium on Application of Geophysics to Environmental and Engineering Problems*, pp. 10.
- Hole, J.A., Catchings, R.D., St. Clair, K.C., Rymer, M.J., Okaya, D.A. & Carney, B.J., 2001. Steep-Dip Seismic Imaging of the Shallow San Andreas Fault Near Parkfield, *Science*, **294**, 1513-1515.
- Illies, J. H. and G. Greiner [*Geol. Soc. Am. Bull.* **89**, 770 (1978)]
- Imoto, M., 1991. Changes in the Magnitude Frequency B-Value Prior to Large (M-Greater-Than-or-Equal-to-6.0) Earthquakes in Japan, *Tectonophysics*, **193/4**, 311-325.
- Johnston, A.C., 1996. Seismic moment assessment of earthquakes in stable continental regions; I, Instrumental seismicity, *Geophys. J. Int.*, **124/2**, 381-414.
- Kanamori, H. & Anderson, D.L., 1975. Theoretical basis of some empirical relations in seismology, *Bull. Seism. Soc. Am.*, **65/5**, 1073-1095.
- Karnik, V., 1968. Seismicity of the European area. Part I, D. Reidel Publishing Company, Dordrecht Holland, pp. 364.
- Kastrup, U., Zoback, M.L., Deichmann, N., Evans, K. & Giardini, D., 2004. Stress field variations in the Swiss Alps and the northern Alpine foreland, *J. Geophys. Res.*, in press.
- Khair, K., Karakaisis, G.F. & Papadimitriou, E.E., 2000. Seismic zonation of the Dead Sea transform fault area, *Annali di Geofisica.*, **43/1**, 61-79.

- Klinger, Y., Avouac, J. P., Dorbath, L., Abou Karaki, N. & Tisnerat, N., 2000. Seismic behaviour of the Dead Sea fault along Araba valley, Jordan, *Geophys. J. Int.*, **142/3**, 769-782.
- Klinger, Y., Van der Woerd, J., Tapponnier, P., Xiwei, X., King, G., Chen, W.B., Ma, W.T., Peltzer, G. & Bowman, D., 2003. Detailed Strip Map of the Kokokili Earthquake Rupture (M_w 7.8, 14/11/01) from Space, *Abstracts for EGU 2003 Meeting*, Nice.
- Kostrov, B.V., 1974. Seismic moment and energy of earthquakes and seismic flow of rock, *Izv. Acad. Sci. USSR Phys. Solid Earth*, **1**, 23-44.
- Lal, D., 1991. Cosmic ray labelling of erosion surfaces: *in situ* nuclide production rates and erosion models, *Earth Planet. Sci. Lett.*, **104**, 424-439.
- Laubscher, H., 2001. Plate interactions at the southern end of the Rhine graben, *Tectonophysics*, **343**, 1-19.
- Lemeille, F., Cushing, M., Carbon, D., Grellet, B., Bitterli, T., Flehoc, C. & Innocent, C., 1999. Co-seismic ruptures and deformations recorded by speleothems in the epicentral zone of the Basel earthquake, *Geodin. Acta*, **12/3-4**, 179-191.
- Levret, A., Backe, J.C. & Cushing, M., 1994. Atlas of macroseismic maps of French earthquakes with their principal characteristics, *Nat. Hazards*, **10**, 19-46.
- Litton, C.D. & Buck, C.E., 1995. The Bayesian approach to the interpretation of archaeological data, *Archaeometry*, **37/1**, 1-24.
- Liu, L. & Li, Y., 2001. Identification of liquefaction and deformation features using ground penetrating radar in the New Madrid seismic zone, USA, *J. Appl. Geophys.*, **47**, 199-215.
- McCalpin, J., Ed., 1996, *Paleoseismology*, Academic Press, San Diego, pp. 588.
- McCalpin, J.P., Forman, S.L. & Lowe, M., 1994. Reevaluation of Holocene faulting at the Kaysville site, Weber segment of the Wasatch fault zone, Utah, *Tectonics*, **13/1**, 1-16.
- Magny, M., Guiot, J. & Schoellamer, P., 2001. Quantitative reconstruction of Younger Dryas to mid-Holocene paleoclimates at Le Locles, Swiss Jura, using pollen and lake-level data, *Quat. Res.*, **56**, 170-180.
- Maineult, A., Schott, J.-J. & Ardiot, A., 2003. 3-D geoelectrical modelling using finite-difference: a new boundary conditions improvement, *Abstracts for EGS-AGU-EUG Joint Assembly*, Nice.
- Mayer-Rosa, D. & Cadiot, B., 1979. A review of the 1356 Basel earthquake : basic data, *Tectonophysics*, **53**, 325-333.

- Meghraoui, M., Camelbeeck, T., Vanneste, K., Brondeel, M. & Jongmans, D., 2000. Active faulting and paleoseismology along the Bree fault, lower Rhine graben, Belgium, *J. Geophys. Res.*, **105**, 13809-13841.
- Meghraoui, M., Delouis, B., Ferry, M., Giardini, D., Huggenberger, P., Spottke, I. & Granet, M., 2001. Active normal faulting in the upper Rhine graben and paleoseismic identification of the 1356 Basel earthquake, *Science*, **293**, 2070-2073.
- Meghraoui, M., Gomez, F., Sbeinati, R., Van der Woerd, J., Mouty, M., Darkal, A.N., Radwan, Y., Layyous, I., Al Najjar, H., Darawcheh, R., Hijazi, F., Al-Ghazzi, R. & Barazangi, M., 2003. Evidence for 830 years of seismic quiescence from palaeoseismology, archaeoseismology and historical seismicity along the Dead Sea fault in Syria, *Earth Planet. Sci. Lett.*, **210**, 35-52.
- Meschede, M., Asprion, U. & Reicherter, K., 1997. Visualization of tectonic structures in shallow-depth high-resolution ground-penetrating radar (GPR) profiles, *Terra Nova*, **9**, 167-170.
- Meyer, B., Lacassin, R., Brulhet, J. & Mouroux, B., 1994. The Basel 1356 earthquake : which fault produced it?, *Terra Nova*, **6**, 54-63.
- Nash, D.B., 1980. Morphological dating of degraded normal fault scarps, *J. Geol.*, **88**, 353-360.
- Nivière, B. & Winter, T., 2000. Pleistocene northwards fold propagation of the Jura within the southern Upper Rhine Graben: seismotectonic implications, *Global and Planet. Change*, **27**, 263-288.
- Nobes, D.C., 1999. Geophysical survey of burial sites: A case study of the Oaro urupa: *Geophysics*, **64**, 357-367.
- Nocquet, J.-M., Calais, E., Altamimi, Z., Sillard, P., & Boucher, C., 2001. Intraplate deformation in western Europe deduced from an analysis of the International Terrestrial Reference Frame 1997 (ITRF97) velocity field, *J. Geophys. Res.*, **106/B6**, 11239-11257.
- Obermeier, S., Pond, E.C. & Olson, S.M., 2001. Paleoliquefaction studies in continental settings: Geologic and geotechnical factors in interpretations and back-analysis, *USGS Open File Report*, **01-29**, pp. 72.
- Ogata, Y., 1999. Seismicity analysis through point-process modeling: A review, *Pure App. Geophys.*, **155 /2-4**, 471-507.
- Orellana, N., 2002. Mécanismes de déformation et contrôle structural des failles de Bâle (Fossé Rhénan) et Pygarki (Fossé de Corinthe), *Mémoire de D.E.A.*, Université Louis Pasteur, Strasbourg.

- Parsons, T.Barka, A., Toda, S., Stein, R., and Dietrich, J.H., 2000. Influence of the 17 August 1999 earthquake on seismic hazards in Istanbul: in *The 1999 Izmit and Duzce Earthquakes: Preliminary Results* (A. Barka, O. Kozaci, S. Akyuz, and E. Altunel, editors), Istanbul Technical University, 295-310.
- Pavoni, N., 1984. Seismotektonik der Nordschweiz, Nagra Technical Report 84-45, Wettingen.
- Pavoni, N., 1987. Seismotektonik der Nordschweiz, *Eclogae Geol. Helv.*, **80/2**, 461-472.
- Plenefisch, T. & Bonjer, K.-P., 1997. The stress field in the Rhine Graben area inferred from earthquake focal mechanisms and estimation of frictional parameters, *Tectonophysics*, **275**, 71-97.
- Poirier, J.P. & Taher, M.A., 1980. Historical seismicity in the Near and Middle East, North Africa, and Spain from Arabic documents (VIIth - XVIIIth centuries), *Bull. Seism. Soc. Am.*, **70**, 2185-2201.
- Reasenber, P.A. , 1985. Second-order moment of Central California Seismicity, *J. Geophys. Res.*, **90**, 5479-5495.
- Reilinger, R.E., McCusky, S.C., Oral, M.B., King, R.W., Toksoz, M.N., Barka, A.A., Kinik, I., Lenk, O., & Sanli, I., 1997. Global positioning system measurements of present-day crustal movements in the Arabian-African-Eurasian plate collision zone, *J. Geophys. Res.*, **102**, 9983-9999.
- Reynolds, J.M. & Taylor, D.I., 1995. The use of geophysical surveys during the planning, construction and remediation of landfills. In: Bentley, S. (ed.), *Engineering Geology of Waste Storage and Disposal*, Geological Society Special Publication, **11**, 93-98.
- Reynolds, J.M., 1997, *An Introduction to Applied and Environmental Geophysics*, John Wiley & Sons, Chichester, pp. 796.
- Rivera, L. & Cisternas, A., 1991. Stress tensor and fault plane solutions for a population of earthquakes, *Bull. Seism. Soc. Am.*, **80**, 600-614.
- Rockwell, T., A. Barka,, T. Dawson, K. Thorup & S. Akyuz, 2001. Paleoseismology of the Gazikoy-Saros segment of the North Anatolia fault, northwestern Turkey: Comparison of the historical and paleoseismic records, implications of regional seismic hazard, and models of earthquake recurrence, *J. Seism.*, **5/3**, 433-448.
- Rockwell, T.K., Akbalik, B., Akoglu, A., Aksoy, E., Barka, A., Dier, D., Ferry, M., Klinger, Y., Langridge, R., Meghraoui, M., Meltzner, A., Ragona, D., Satir, D., Seitz, G. & Uçarkuş, G., 2001. Results of Paleoseismic Studies After the 1999

- Izmit Earthquake: Implications for Seismic Hazard to Istanbul, *Abstracts for EUG 2001 meeting, Strasbourg*, **1**, 292.
- Rockwell, T.K., S. Lindvall, T. Dawson, R. Langridge, W. Lettis & Y. Klinger, 2002. Lateral offsets on surveyed cultural features resulting from the 1999 Izmit and Duzce earthquakes, Turkey, *Bull. Seism. Soc. Am.*, **92**, v.1.
- Rockwell, T.K., Seitz, G., Langridge, R., Aksoy, E., Barka, A., Ferry, M., Klinger, Y., Meghraoui, M., Meltzner, A., Ragona, D. & Uçarkuş, G., 2002. Paleoseismology of the Western North Anatolian Fault near the Marmara Sea: The past 400 years of surface ruptures east and west of Istanbul, *Abstracts for 1st ITU Symposium on Earth Sciences and Engineering, Istanbul*, **1**, 58.
- Rowan, L.C. & Mars, J.C., 2003. Lithologic mapping in the Mountain Pass, California area using Advanced Spaceborne Thermal Emission and Reflection Radiometer (ASTER) data, *Remote Sens. Environ.*, **84**, 350-366.
- Schleicher, M., Grootes, P.M., Nadeau, M.-J. & Schoon, A., 1998. The carbonate ¹⁴C background and its component at the Leibniz AMS facility, *Radiocarbon*, **40/1**, 85-93.
- Schnellmann, M., Anselmetti, F., Giardini, D., McKenzie, J. & Ward, S., 2003. Prehistoric earthquake history revealed by lacustrine slump deposits, *Geology*, **30/12**, 1131-1134.
- Schwarz, D. P. & Coppersmith, K. J., 1984. Fault behavior and characteristic earthquakes: Examples from the Wasatch and San Andreas faults, *J. Geophys. Res.*, **89**, 5681-5698.
- Shimazaki, K., Nakata, T., 1980. Time-predictable recurrence model for large earthquakes, *Geophys. Res. Lett.*, **7**, 279-282.
- SIA 260, 2003, Swiss Standard SIA 260: Action on Structures, Swiss Society Engineers and Architects, Zurich.
- Sieh, K.E., 1978, Prehistoric Large Earthquakes Produced by Slip on the San Andreas Fault at Pallett Creek, California, *J. Geoph. Res.*, **83**, 3907-3939.
- Sieh, K. E., 1996. The repetition of large-earthquake ruptures, *Proc. Nat. Acad. Sci.*, **93**, 3764-3771.
- Smith, D.G. & Jol, H.M., 1995. Wasatch fault (Utah), detected and displacement characterized by ground-penetrating radar, *Env. Engin. Geosc.*, **1/4**, 489-496.
- Steier, P. & Rom, W., 2000. The use of Bayesian statistics for ¹⁴C dates of chronologically ordered samples: a critical analysis, *Radiocarbon*, **42/2**, 183-198.

- Stephenson, W.J., Smith, D.G. & Pelton, J.R., 1993. A high-resolution seismic reflection and gravity survey of Quaternary deformation across the Wasatch fault, Utah, *J. Geoph. Res.*, **98/B5**, 8211-8223.
- Stratton Noller, J., Sowers, J.M., Lettis, W.R., Eds., 2000, Quaternary Geochronology: Methods and Applications, AGU Reference Shelf, 4, pp. 582.
- Straub, C. & Kahle, H., 1995. Active crustal deformation in the Marmara Sea region, NW Anatolia, inferred from GPS measurements, *Geophys. Res. Lett.*, **22/18**, 2533-2536.
- Straub, C.S., 1996. Recent crustal deformation and strain accumulation in the Marmara Sea region, N.W. Anatolia, inferred from GPS measurements. unpub. Ph.D. dissertation, Swiss Federal Institute of Technology at Zurich, 122 p. plus appendices.
- Stuiver M., Reimer, P.J., Bard, E., Beck, J.W., Burr, G.S., Hughen, K.A., Kromer, B., McCormac, G., van der Plicht, J. & Spurk, M., 1998. INTCAL98 Radiocarbon Age Calibration, 24000-0 cal BP, *Radiocarbon*, **40/3**, 1041-1083.
- Suzuki, K., Toda, S., Kusunoki, K., Fujimitsu, Y., Mogi, T. & Jomori, A., 2000. Case studies of electrical and electromagnetic methods applied to mapping active faults beneath the thick quaternary, *Eng. Geol.*, **56**, 29-45.
- Swan, F.H., Schwartz, D.P. & Cluff, L.S., 1980. Recurrence of moderate to large magnitude earthquakes produced by surface faulting on the Wasatch fault zone, Utah, *Bull. Seism. Soc. Am.*, **70/5**, 1431-1462.
- Van der Woerd, J., Ryerson, F.J., Tapponnier, P., Gaudemer, Y., Finkel, R., Meriaux, A.S., Caffee, M., Zhao Guoguang & He Qunlu, 1998. Holocene left-slip rate determined by cosmogenic surface dating on the Xidatan segment of the Kunlun fault (Qinghai, China), *Geology*, **26/8**, 695-698.
- Vanneste K., Verbeeck K., Camelbeeck T., Paulissen E., Meghraoui M., Renardy F., Jongmans D. & Frechen M., 2001. Surface-rupturing history of the Bree fault scarp, Roer Valley graben: Evidence for six events since the late Pleistocene, *J. Seism.*, **5**, 329-359.
- Vogt, J., 1979. Les tremblements de terre en France, *Mem. Bur. Rech. Geol. Min.*, **96**, 153-165.
- Wells, D.L. & Coppersmith, K.J., 1994. New empirical relationships among magnitude, rupture length, rupture width, rupture area, and surface displacement, *Bull. Seism. Soc. Am.*, **84/4**, 974-1002.
- Wiemer, S. , 2001. A software package to analyze seismicity: ZMAP, *Seism. Res. Letters*, **72**, 373-382.

- Wintle, A.G. & Huntley, D.J., 1982. Thermoluminescence dating of sediments, *Quat. Sci. Rev.*, **1**, 31-53.
- Zollinger, G., 1991. Zur Landschaftsgenese und Quartärstratigraphie am südlichen Oberrheingraben –am Beispiel der Lössdeckschichten der Ziegelei in Allschwil (Kanton Basel-Landschaft), *Eclogae geol. Helv.*, **84/3**, 739-752.

Acknowledgements

Before all, I would like to thank the community of earthquake geologists, or paleoseismologists, which sometimes appears like a secret society of some sort. These people are presently rare, especially in Europe, and show a constant sense of solidarity and sharing. I met some of them, who make a newcomer feel at ease and part of a special group instantly. Namely, they were Daniela Pantosti, Tom Rockwell, Christian Walls, Daniel Ragona, Gordon Seitz, Ramon Arrowsmith, Eulàlia Masana and Joan Fonseca, among many others.

My most sincere thanks go to Domenico Giardini, Mustapha Meghraoui and Bertrand Delouis who provided me with strong and unique scientific support and a genuine point of view of what science should be and how scientists should regard it.

I should not forget to mention all my Turkish colleagues and now friends who welcomed me and showed me unthought-of facets of their beautiful and charming country. An increasing number of people call me Mehmet thanks to Gülsen Uçarkus, Ersen Aksoy, Özgür Kozacı, Burçak Akbalık, Dilek Satır, Aynur Dikbas, Serdar Akyuz and Erhan Altunel. I would add a special thought for the late and deeply regretted Aykut Barka who left far too early.

This would not be complete without a big “Merci viel mal!” to Peter Schürch for helping me in the field and for trying to teach me Lindy Hop. Thanks also go to my colleagues from the PALSEIS group: Arnfried Becker, future Doctor Katrin Monecke and now Doctor Michäel Schnellmann.

I would like to express my deep gratitude to my parents Edith and Alain and to my sister Johanne who all started calling me doctor when I was 10: it worked. And to Maggy who is checking, down under, if kangaroos are isotropic and koalas anisotropic. Or reverse, maybe.

*To Andrée and Jean,
they would have appreciated that moment*

Lebenslauf

Ferry Matthieu

Born March 23rd, 1973 in Nancy, France.

Expected degree: PhD in Sciences, ETH Zurich, 2004.

Master degree (1999)

Title: *Electromagnetic imaging of the Nîmes and Moyenne Durance faults with application to seismic risk assessment.*

Laboratoire d'Imagerie Tectonique, Institut de Physique du Globe, Université Louis Pasteur. Supervisors: Maksim Bano and Guy Marquis.

Graduation report (1998)

Title: *The October 1997 seismic crisis in Italy: seismotectonic implications.*

Laboratoire de Sismologie, Institut de Physique du Globe, Université Louis Pasteur. Supervisors: Michel Granet and Jean-Christophe Maurin.

Baccalaureate in Sciences, with honors (1991).

Bibliography

- Meghraoui, M., Delouis, B., **Ferry, M.**, Giardini, D., Huggenberger, P., Spottke, I. and Granet, M., 2001, *Active Normal Faulting in the Upper Rhine Graben and Paleoseismic Identification of the 1356 Basel Earthquake*, *Science*, 293, 2070-2073.
- Perea, H., Figueiredo, P. M., Carner, J., Gambini, J., Boydell, K. and participants in the Europealeos course, 2003, *Paleoseismological data from a new trench across the El Camp Fault (Catalan Coastal Ranges, NE Iberian Peninsula)*, *Ann. Geophys.*, 46/5, 763-774.
- Ferry, M.**, Meghraoui, M., Rockwell, T., Kozaci, O., Akyuz, S., Girard, J.-F. and Barka, A., 2004, *GPR investigations along the North Anatolian Fault near Izmit (Turkey): Constraints on the right-lateral movement and slip history*, *Geology*, 32/1, 85–88.
- Ferry, M.**, Meghraoui, M., Delouis, B., and Giardini, D., in press, *Evidence for Holocene Paleoseismicity along the Basel-Reinach Active Normal Fault (Switzerland): A Seismic Source for the 1356 Earthquake in the Upper Rhine Graben*, *Geophys. J. Int.*.
- Rockwell, T.K., Seitz, G., Langridge, R., Barka, A., Aksoy, E., Uçarkus, G., Akbalik, B., Satir, D., Meltzner, A., Ragona, D., Klinger, Y., Meghraoui, M. and **Ferry, M.**, 2004, *Paleoearthquake History of the western portion of the North Anatolian Fault in Western Turkey from paleoseismic data, and implications to the seismic hazard of Istanbul*, Submitted to *Bull. Seism. Soc. Am.*.
- Becker, A., **Ferry, M.**, Monecke, K., Schnellmann, M. and Giardini, D., 2004, *Multiarchive Paleoseismic record of late Pleistocene and Holocene strong earthquakes in Switzerland*, submitted to *Tectonophysics*.

As well as 18 oral and poster presentations in various national and international workshops and meetings including AGU, EUG, EGS and EGU.

